SA-2000517500000

SECRET

LA-4919

Nuclear Weapon Data
Sigma 1
Critical Nuclear Weapon
Design Information Per
DoD Directive 5210.2

Series D Issued: March 1985

This document consists of 115 pages
No. 6 of 10 copies, Series D

DP-32HAI89AD013
This document consists of 115 pages
No. 1 of 1 Copies, Series OC-A

UNCLASSIFIED

Nuclear Weapon and Material Detection (U)

DEPARTMENT OF ENERGY DECLASSIFICATION REVIEW

1ST REVIEW-DATE: 3-2-95
AUTHORITY: ☐ADC ☐ADC ☒ADD
NAME: P.A. Carpenter
2ND REVIEW-DATE: 3-29-95
AUTHORITY: ADD
NAME: [illegible]

DETERMINATION (CIRCLE NUMBER(S))
(1) CLASSIFICATION RETAINED
2. CLASSIFICATION CHANGED TO: ____
3. CONTAINS NO DOE CLASSIFIED INFO
4. COORDINATE WITH: ____
5. CLASSIFICATION CANCELLED
(6) CLASSIFIED INFO BRACKETED
(7) OTHER (SPECIFY): Concurred w/ Ltr
ACDA, CIA, NN-40, Navy, Air Force

18 7-3258 6/10D $

Los Alamos National Laboratory
Los Alamos, New Mexico 87545

Los Alamos National Laboratory is operated by the University of California for the United States Department of Energy under contract W-7405-ENG-36.

Derivative Classifier
John McDonald
Classification Officer

J.W. Dimmick 3/23/90
P.A. Carpenter 3-23-90

UNCLASSIFIED

RESTRICTED DATA

This document contains Restricted Data as defined in the Atomic Energy Act of 1954. Unauthorized disclosure subject to Administrative and Criminal Sanctions.

SECRET

R281 142 151

8706315A

This document consists of 113 pages
No. [illegible] of 75 copies, Series A

LA-4919
ATOMIC WEAPON DATA
CATEGORY SIGMA 1
CRITICAL NUCLEAR WEAPON
DESIGN INFORMATION PER
DOD DIRECTIVE 5210.2
ISSUED: July 1972

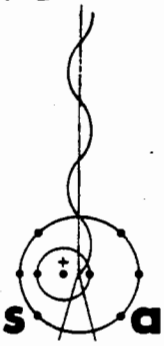

los alamos
scientific laboratory
of the University of California
LOS ALAMOS, NEW MEXICO 87544

Nuclear Weapon and Material Detection (U)

by

W. H. Chambers
H. F. Atwater
J. T. Caldwell
P. E. Fehlau
C. N. Henry
J. H. Jett
W. E. Kunz
W. E. Mauldin
N. Nicholson
A. A. Robba
T. E. Sampson

Supported by the Air Force Space and Missile Systems Organization

UNITED STATES
ATOMIC ENERGY COMMISSION
CONTRACT W-7405-ENG. 36

ATOMIC WEAPON DATA
Category Sigma 1
LA-4919

USAEC, Headquarters Library, Reports Section, Washington, D. C.	1-3
Division of Military Application, Washington, D. C.	4
Attn: Col. Henry W. Parlett	
Manager, ALO, Albuquerque, New Mexico	5
Attn: Myron Roepke	
Lawrence Livermore Laboratory, Livermore, California	6-7
Attn: Robert daRoza	
Sandia Corporation, Albuquerque, New Mexico	8
Attn: Charles Winter	
Military Liaison Committee, Washington, D. C.	9
Director, Defense Research and Engineering, Washington, D. C.	10
Headquarters, Defense Nuclear Agency, Washington, D. C.	11-12
Defense Nuclear Agency Field Command, Kirtland AFB, New Mexico	13-15
Commanding General, Army Combat Developments Command, Fort Belvoir, Virginia	16-17
Commanding General, Army Materiel Command, Washington, D. C.	18
DCS/Operations, Army, Washington, D. C.	19
Chief, R&D, Army, Washington, D. C.	20
Naval Ordnance Systems Command, Washington, D. C.	21
Chief of Naval Operations (OP-75), Washington, D. C.	22
Naval Research Laboratory, Washington, D. C.	23
Attn: Keith W. Marlow	
DCS/Research and Development, Headquarters, USAF, Washington, D. C.	24
Director, Air Force Weapons Laboratory, Kirtland Air Force Base, New Mexico	25-27
Space and Missile Systems Organization, Los Angeles, California	28-47
Attn: Lt. Col. Clement/Lt. Holliday	
Los Alamos Report Library	48-75

CONTENTS

b(1)

LIST OF TABLES

LIST OF FIGURES

NUCLEAR WEAPON AND MATERIAL DETECTION

by

W. H. Chambers, H. F. Atwater, J. T. Caldwell,
P. E. Fehlau, C. N. Henry, J. H. Jett,
W. E. Kunz, W. E. Mauldin, N. Nicholson,
A. A. Robba, and T. E. Sampson

ABSTRACT (SNSI)

[redacted]

b(1)

I. Summary

As a follow-on to the mission analysis study of the inspection of orbiting satellites suspected of carrying nuclear weapons (SAMSO TASK 11), Los Alamos Scientific Laboratory (LASL) conducted a detailed experimental and theoretical investigation of nuclear sensor techniques. The objectives were to (1) define for the 1970-1980 period the observables constituting weapon detection and the effects of potential countermeasures, (2) analyze the sensors recommended in Task 11 and explore new sensor concepts, (3) select preferred techniques, and (4) define the performance of the selected techniques as well as the imposed mission constraints.

Unique identification of weapon fission fuels and discrimination from other radioactive materials is accomplished primarily by high-resolution [Ge(Li)] gamma spectrometry. High-resolution spectra from eight US weapons representing the yield range from 50 kt to 10 Mt were measured and analyzed for characteristic energies and for absolute flux as a function of distance and view angle in order to specify the spectrometer requirements. Low-resolution gamma spectra and flux from a number of other weapons have also been evaluated. Similar data for neutron flux were obtained in a few cases because of the redundancy that can be provided by neutron detectors in the identification of material and estimation of quantities.

Unique identification of deuterium as the principal thermonuclear fuel requires photointerrogation at energies (typically 2.62-MeV gamma or 4-MeV bremsstrahlung) above the $D(\gamma,n)$ threshold, with subsequent

neutron detection. Discrimination from interfering Be(γ,n), which has a lower threshold energy, is made possible by changing source energy (to 1.69-MeV gamma or 2.2-MeV bremsstrahlung), by determining neutron endpoint energy with ^{4}He neutron spectrometry, or by measuring neutron average energy with moderated ^{3}He neutron detectors. With these incident gamma energies, which are below the photofission threshold, the same neutron spectral techniques allow determination of the coupling between fission and fusion fuels through the D(γ,n) plus U(n,f) reactions.

The gamma sources for the experimental photointerrogation studies were either selected radioisotopes or one of several pulsed bremsstrahlung sources, and an extensive series of small sample, mockup, and weapon irradiations were done to establish neutron yields and spectral characteristics. Neutron spectrometer development was also necessary to establish instrumentation limitations. The final calculational and experimental results from this sequence of investigations are presented for six typical US weapons and USSR weapon models in the 1- to 25-Mt range.

The identification of weapons by the characteristic arrangement of essential components is accomplished primarily by radiographic imaging. Essentially the same sources (energy and intensity) appropriate to photointerrogation are applicable to radiography, although the source and detector (radiographic screen) must now be on opposite sides of the target.

b(1)

An evaluation of radiographic detector components was conducted first in order to select equipment for further parametric studies on source and geometry requirements. Seven representative weapons were used as targets in the course of this work, which involved a wide variety of isotopic and pulsed sources.

b(1)

These essential techniques are further fortified by the use of pulsed sources (7.5-MeV bremsstrahlung or 14-MeV neutrons) for inducing fissions in the target weapon. The fission neutron yield and/or time history provides another unique identification of fissionable materials and in some cases gives significant design information. The availability of 7.5-MeV bremsstrahlung also extends the radiographic capability to heavier targets, provides some limited material identification through characteristic gamma decay of isomeric states, and, in conjunction with neutron spectrometry, may help confirm thermonuclear design information. Many experiments and calculations were conducted in these general areas to assist in defining sources, instrumentation, and operational requirements.

Because there is no optimum or preferred system but rather a continuum encompassing many variables in areas such as weapon design, space background, and operational constraints, the results are presented in four discrete steps. The simplest sensor package (SP-1) which provides some capability for each of the principal techniques mentioned above (gamma spectrometry, radiographic imaging, and photointerrogation above the deuterium photodisintegration threshold) is specified as the minimum useful system.

b(1)

SP-4, the most complex sensor package to be considered at all practical (including the techniques above plus photofission yield and time-history measurements),

b(1)

The most realistic package for actual hardware development probably lies somewhere between these extremes.

This brief summary of the recommended techniques, and possible options in sensor hardware to implement the techniques with varying cost and confidence, indicates satisfactory attainment of the study objectives. General conclusions and recommendations regarding subsequent efforts can be found in Sec. VII. It is important to emphasize that there is no optimum system, nor will any of the systems described here result in complete confidence in weapon detection under all postulated conditions. The possible sensor systems represent a continuum, and those presented in this report indicate a best estimate of the practical limits to that continuum.

II. Introduction

During the period from June 1970 through February 1971, Task 11 was conducted by Space and Missile Systems Organization (SAMSO) using two industrial contractors, with technical direction and ancillary support from Aerospace Corporation,

b(1)

The AEC nuclear weapon

laboratories provided advice and assistance to SAMSO before the contractors were selected and also during this mission analysis effort, in particular with regard to the nuclear sensor and interrogation subsystems and to basic nuclear weapon data. Predictably, one of the study findings emphasized the need for a follow-on nuclear sensor analysis and experimentation effort to clarify and quantize system parameters in the nuclear package. Thus, in March 1971 a nine-month theoretical and experimental program was undertaken by LASL. Progress during this study was reported periodically in a working group composed of representatives from LASL, SAMSO, Aerospace, Division of Military Application (DMA), AEC Albuquerque Operations Office (ALO), Lawrence Livermore Laboratory (LLL), and Sandia Laboratories. The present report constitutes the final summary and outlines the conclusions of the study.

The statement of work agreed upon at the outset listed four separate technical areas for detailed investigation and provided guidance on the relative effort to be expended on each. Briefly, these areas include:

(1) (10%) Definition of weapon design options during the 1970-1980 period, the possibility of tailoring weapon designs to defeat detection and identification by the proposed nuclear sensors, and the potential penalties associated with such countermeasures.

(2) (15%) Tabulation of gamma spectra and flux and neutron flux for representative weapon designs, including distance and weapon aspect angle considerations.

(3) (45%) Experimental investigation of radiographic techniques for this application using a large scintillating screen, a wide-angle lens, high-gain image intensifier, and photographic recording. The parameter study was to emphasize the minimum radiation intensity and energy required for positive detection.

(4) (30%) Application of a variety of neutron and photointerrogation techniques with both experimental and theoretical delineation of source and detector requirements and with typical weapon responses in neutron and gamma yields and time histories.

Because the experimental study was short-term and funded at a modest level ($250K), no new source facilities were contemplated for the active interrogation studies. Rather, a variety of existing installations at LASL were used without modification. Table I lists the sources along with certain information to identify further their major characteristics. These will be referred to without further amplification in later sections of this report. Most of the small sample and weapon component work was carried out at these LASL facilities. However, to get additional passive and active data on a variety of weapons conveniently, several field trips were made to the AEC fabrication and assembly plant at Amarillo, Texas (Pantex). The linac used routinely there for inspection and quality control was used as a bremsstrahlung source and is also listed in Table I.

The complex nature of the interface between the nuclear instrumentation used to detect and identify weapons and the spacecraft required to carry that instrumentation precluded any real sensor choices at this stage in the overall development program. Rather, the wide latitude in system synthesis has been indicated by illustrating several potential systems with increasing levels of complexity, size, and information return. The possible sensor systems really represent a continuum, and those presented in this report indicate a best estimate of the practical limits to that continuum as well as several intermediate examples. The correct inference is that hard engineering choices would have to be made by negotiation between the various requirements on a spacecraft-booster combination, and that a flyable sensor system would probably lie somewhere between the minimum-useful and maximum-complexity cases illustrated here.

III. Weapon Designs

The general design features and characteristics that may affect nuclear detection and identification systems for present weapon technology have been described elsewhere[4] and will not be reproduced here. However, the specific strategic warheads (RV's) which were in the current US inventory and which were used in the experiments conducted during the study are typical pegpoints in a wide range of generalized designs (50 kt to 10 Mt). The relevant parameters for these are summarized in Table II and will also be referred to in various later sections of the report. The weapons presented in Table II actually span a decade or more of modern developments and certainly represent the current state of the technology. Table II also lists characteristics as calculated for one plausible set of warheads matching the [redacted] capabilities. These designs are used for reference points in later sections where sensor performance is calculated.

In addition to the stockpile weapons and extrapolated designs, some test devices and/or subassemblies are referenced in specific experiments and calculations. The significant characteristics of these will be given in the appropriate sections.

TABLE I

ACTIVE INTERROGATION FACILITIES

Machine		Beam Energy and Type	Target and Thickness	Spot Size (in.)	Pulse Width	rep Rate
SCAPP	GMX-11 flash x-ray Single Cavity PHERMEX Prototype	3-7 MeV bremsstrahlung	0.010-0.043-in. W	1/8-1	0.2 μsec	Single pulse to 1 pps
Febetron	GMX-1 flash x-ray	2.3 MeV bremsstrahlung	0.025-in. Ta	1/4	0.020 μsec	Single pulse
Million Volt Machine	GMX-1	1 MeV bremsstrahlung	0.002-in. W	3/8	Sinusoidal ~ 100 μsec	1000 cps
Betatron	GMX-1	22 MeV bremsstrahlung	Internal ~0.100-in. Pt	0.008	~ 1 μsec	180 cps
Pantex Linac	Linear accelerator	7-10 MeV bremsstrahlung	0.040-in. Pt	1/16	~ 5 μsec	15-250 cps
EPA	MP-3 EPA	4-27 MeV bremsstrahlung	0.002-in. W	< 0.4	50-500 μsec	120 cps
Cockcroft-Walton	Deuterium accelerator	350 keV deuterium (14-MeV neutrons)	Deuterium, Tritium	NA	1 nsec-dc	10^6 cps
Zipper	Sandia high-output neutron generator	180 keV tritium (14-MeV neutrons)	Deuterium	NA	5-30 μsec	1-10 cps

As presently foreseen, advanced development over the next decade is directed along two principal lines insofar as strategic weapons are concerned. The first, and most predictable, effort concerns the refinement of primaries to smaller sizes, thus permitting small improvements in yield-to-weight ratios at the low end of the strategically significant yield range. Because of the large leverage which results from this factor, particularly in systems, this approach is expected to be continued for at least as long as nuclear testing continues. The nature of these developments, is such as to have relatively little effect on nuclear detection and identification techniques. Modest increases in amounts of fissile material present would make detection easier with some of the proposed techniques. On the other hand, increased emphasis on hardening against ABM tactics would somewhat degrade other sensor methods.

Application to strategic warheads appears unlikely. In any event, secondaries are not expected to change radically from those presently stockpiled in the strategic systems, Thus, this line of future development is not expected to produce any large surprises in the detection and identification game in the 1970's.

TABLE II

WEAPON DESIGN CHARACTERISTICS

The motivation for the strategic designer perhaps lies in an increase by a factor of three or four in yield-to-weight ratios, but the probability of successful deployment of such a weapon in the 1970-1980 period is low and unpredictable. Because of this uncertainty, the design of an inspection system should not be influenced strongly by characteristics

Assuming typical and current weapon technology, the important criteria for detection and identification can be listed. While the order of listing is not necessarily significant, two categories are used which to some extent separate the detection and identification criteria from those of acquiring significant additional intelligence data. Obviously there is considerable overlap in these two categories as well as in the individual criteria. Some items as listed are not entirely separable except under the limitations of specific techniques, nor are all items relevant to all potential warheads. However, all are discernible to some degree by the inspection methods proposed in this report.

(1) (a) Unique identification of the essential fission and fusion fuels: ^{235}U, ^{238}U, ^{239}Pu, and deuterium.

(b) Determination of approximate quantity and distribution of fissile and fusion fuels,

(c)

(2) (a) Identification and configuration of high-Z materials in nuclear components and radiation case.

(b) Determination of radiation channel, HE, and RV configurations.

(c) Measurement of approximate attenuation of system in unique locations.

(d) Identification of RV- and warhead-hardening techniques.

(e) Determination of significant fuzing and firing details that might be associated with boosting or safing components.

(f) Measurement of nuclear material isotopic ratios for production cycle information.

(g) Determination of reactivity of subcritical configurations by dynamic response.

These criteria, if completely determinable, would give high confidence to any statement as to the presence of nuclear warheads and would with reasonable confidence add to the completeness and accuracy of current US estimates of foreign weapon technology. The complexity of the list requires a combination of techniques to maximize the chance of obtaining reliable data on any given target. As will be seen later in the correlation of sensor packages to detection criteria, the overall success rate is related directly to the number and sophistication of the detection techniques employed and to the relative absence of countermeasures.

IV. Countermeasures

b(1)

V. Detection Techniques

A. Passive Gamma Technique.

1. Characteristic Gamma Signature of Weapons Materials. The major characteristic signatures of the various radioactive weapon materials will be discussed only briefly. The reader is assumed to have a basic knowledge of these signatures and the decay chains involved.

Characteristic ^{238}U lines at 766.4 and 1001.0 keV arise from the ^{234m}Pa daughter which attains equilibrium in about three months after chemical purification of the uranium.

TABLE III

DESIGN-INDUCED COUNTERMEASURES

Design Feature	Affected Inspection Technique	Countermeasure Effectiveness	Approximate Yield Penalty for Warhead of Size: 100-500 kt	0.5-5 Mt	>5 Mt
[redacted]					

b(3) b(1) b(3) b(3)

A useful reference exhibiting spectra of many of the above-mentioned isotopes is Idaho Nuclear Corp. report IN-1448 Rev. (January 1971).

2. Gamma Spectra of US Weapons. The following figures display the basic features of the gamma spectra from several types of US weapons. Some of these data have been published previously,[9] but separate spectra taken at the primary and secondary are shown here to illustrate the relative intensity of the various lines. These particular spectra are all taken close to the weapon

TABLE IV

ADD-ON COUNTERMEASURES

Countermeasure Type	Affected Inspection Technique	Countermeasure Effectiveness	Approximate Weight Penalty for Warhead of Size: 100-500 kt	0.5-5 Mt	> 5 Mt
[redacted]					

b6

(≈ 3 ft) and cannot be used to infer count rates at larger distances. However, an excellent idea of the spectral features observed at large distances can be obtained by combining visually the primary and secondary spectra. Table II gives the basic design features of these devices.

Figure 1 shows the spectrum from the W-62 with the detector looking in the channel between the primary and secondary. In this and subsequent spectra, unless otherwise stated, the 6% Ge(Li) detector (relative to 3- by 3-in. NaI at 1.33 MeV and 25 cm distance) is shielded and collimated to a 74° field of view (FOV). This spectrum of the W-62 is the same as that seen at a distance

Spectra from the Mk-28 are exhibited in Fig. 2.

The Mk-43 spectra in Fig. 3 are similar to those of the Mk-28.

In Fig. 4, the spectrum from the primary of the W-56

Similar spectra are observed from the W-47 and W-58.

Spectra from the primary and secondary of the Mk-53 are shown in Fig. 5.

In Fig. 6 spectra from the primary (top), and secondary (bottom) of the W-59 are shown. These spectra were taken with a 41° FOV, shielded, 4.5% relative efficiency Ge(Li) detector 20 in. from the axis of the weapon. Counting times were 4000 sec, and the weapon was in its shipping container.

These figures emphasize the design-dependent range of gamma outputs. As is well known, there is no one basic design parameter (size, weight, yield, etc.) that can be correlated directly with the gamma output. For example,

Fig. 1.
W-62 gamma spectrum, 32 in. from axis between primary and secondary, 1000 sec.

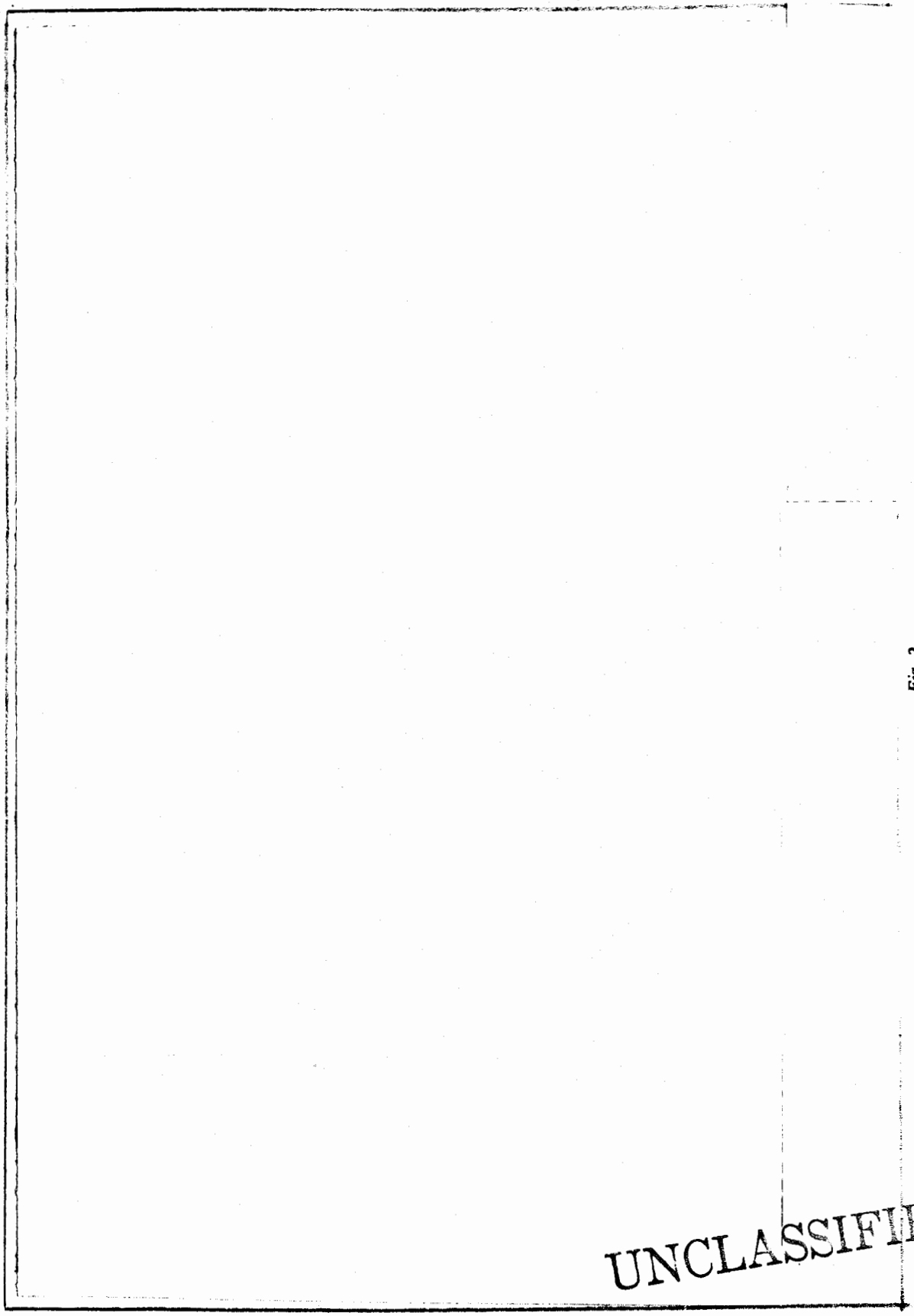

Fig. 2.
Mk-28 gamma spectra, 28 in. from axis, 1000 sec.
Top plot is at primary, bottom at secondary.

Fig. 3.
Mk-43 gamma spectra, 27 in. from axis, 1000 sec.
Top plot is at primary, bottom at secondary.

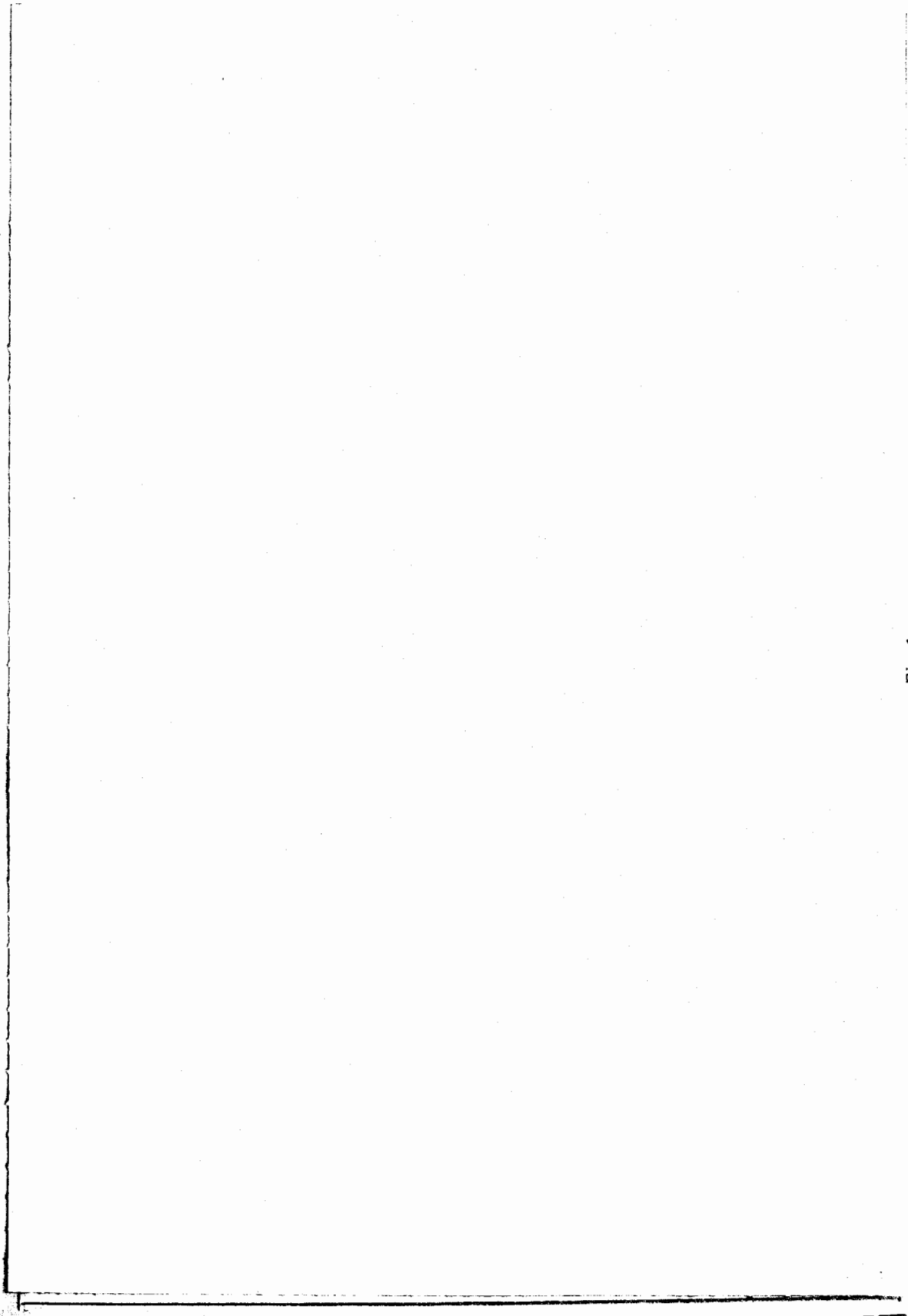

Fig. 4.
W-56 gamma spectra, 44 in. from axis, 1000 sec.
Top plot is at primary, bottom at secondary.

Fig. 5.
Mk-53 gamma spectra, 30 in. from axis, 1000 sec.
Top plot is at primary, bottom at secondary.

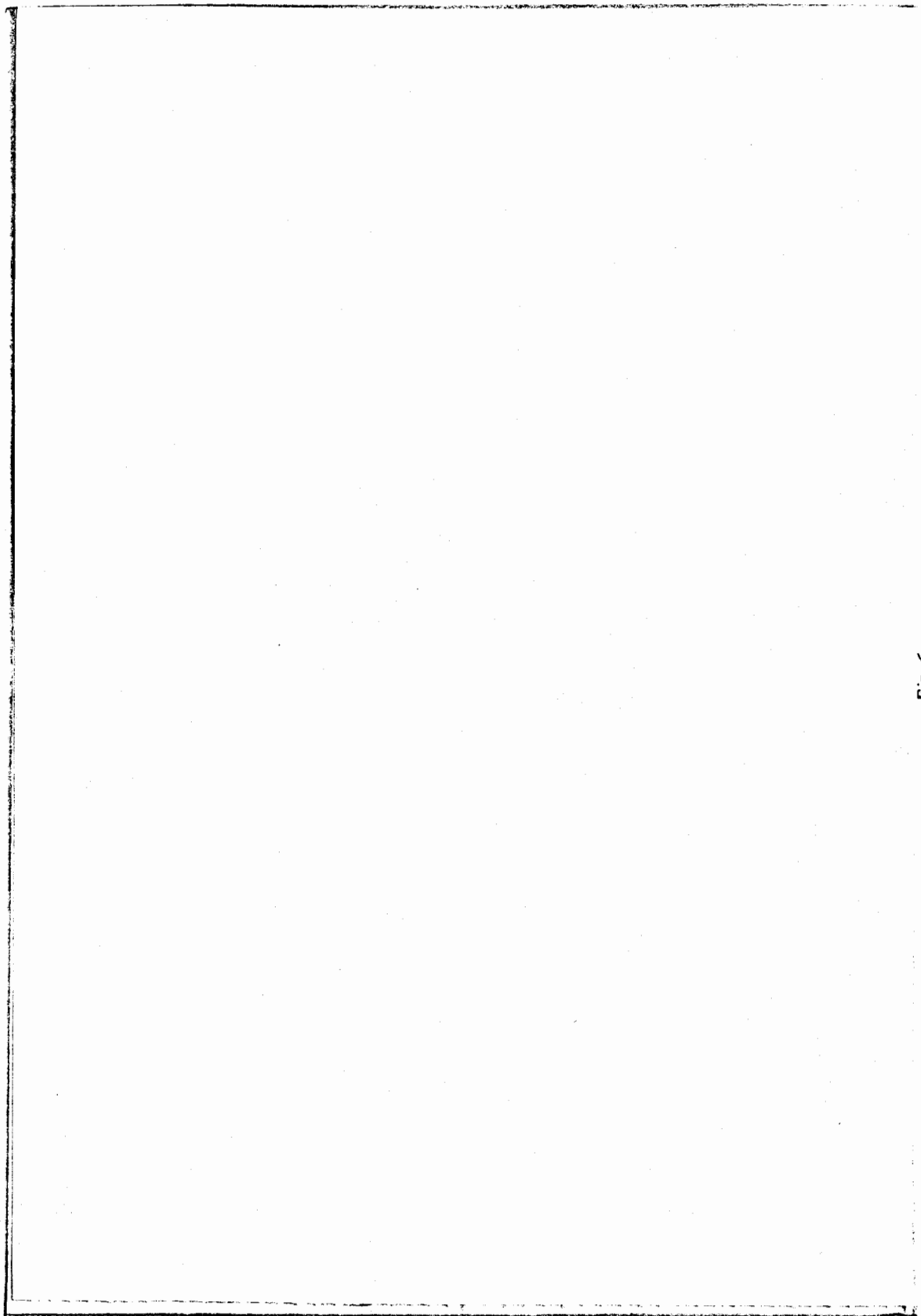

Fig. 6.
W-59 gamma spectra, 20 in. from axis, 4000 sec with 4.5% Ge(Li).
Top plot is at primary, bottom at secondary.

Data to be shown later will also illustrate the strong view-angle dependence of these spectra.

These spectra indicate that the lines that can be used for isotopic identification in practical cases are the characteristic plutonium and ^{238}U lines. The 2614-keV line is there, but its presence, in general, cannot be unambiguously assigned to a specific isotope, because it can be observed from 93.5% ^{235}U, ^{239}Pu, and ^{232}Th.

3. Experimental Results. The major experimental gamma-spectroscopy effort in this program was devoted to measuring photopeak fluxes from various US weapons systems as a function of distance and view angle. A discussion of some characteristics of Ge(Li) detectors is relevant to the effort and is given separately in Appendix A. The measurements were made with 6% Ge(Li) and 3- by 3-in. NaI detectors, and net counts in each photopeak were obtained by subtracting a linear extrapolation of the Compton continuum from underneath the photopeak. The efficiency curves of the appendix were then used to convert net photopeak counts to photopeak flux.

For the NaI data, the 400-keV ^{239}Pu complex appears as one peak. The flux was computed for the entire complex using the detector efficiency value at 400 keV. The high resolution data of Cline[7] shows that the 375- and 414-keV thin sample intensities are equal. The sum of the 375- and 414-keV intensities in turn is equal to approximately one-half the total intensity between 300 and 450 keV, the range covered in the NaI peak. With these arguments for a basis, the 375- and 414-keV photopeak fluxes or counting rates were approximated by taking each to be equal to one-fourth of the total flux in the 400-keV complex. This approximation neglects minor differences in attenuation in the weapon; however, these differences tend to be cancelled in the detector counting rate because of the slope of the detector efficiency curve.

Data were taken at LASL on the W-59 in its shipping container with both NaI and Ge(Li) detectors in a 33° FOV geometry. Measurements as a function of distance out to about 30 ft were made at four different view angles. For two of the view angles both Ge(Li) and NaI data were taken. In Fig. 7, a comparison of the Ge(Li) and NaI data is shown for the 375- and 414-keV lines as well as for the entire 400-keV complex. The view angle here is looking at the center of the channel at a 45° angle between the side and the primary end of the device. A similar comparison for the D-38 lines for side incidence is shown in Fig. 8.

Fig. 7.
W-59 photopeak flux vs distance, plutonium photopeaks, NaI and Ge(Li) detectors.

The scatter of the points is indicative of the magnitude of errors that arise in the measurement,

Fig. 8.
W-59 photopeak flux vs distance, ^{238}U photopeaks, NaI and Ge(Li) detectors.

TABLE V

PHOTOPEAK FLUX VS VIEW ANGLE, W-59 AT 20 FT

Flux ($\gamma/cm^2/sec$)

These studies were carried out on four different designs (W-62, W-68, Mk-53, Mk-43) at Pantex and Figs. 9 through 11 show the results of some of the measurements, all taken with a 3- by 3-in. NaI detector in 51° FOV geometry. Typical spectra from which these data points were extracted are shown in Figs. 12 through 16.

These illustrated spectra were all taken at 20 ft for count times of 10 to 20 min and represent realistic spectra that would be obtained in a low background inspection for reasonable counting times if a 3- by 3-in. NaI detector were used. The results of the flux measurements for a distance of 20 ft are tabulated in Table VI.

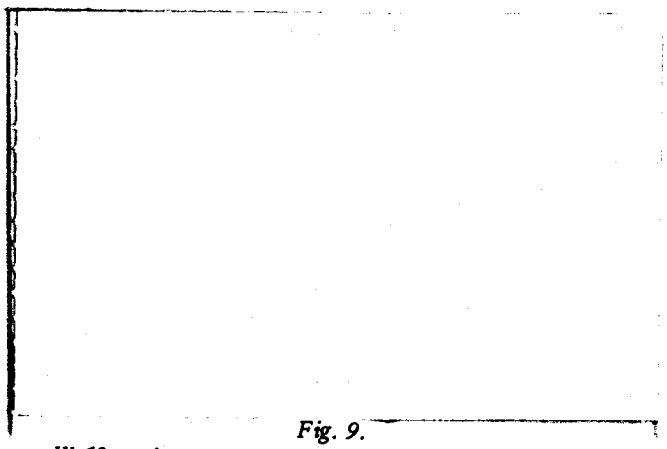

Fig. 9.
W-62 and W-68 photopeak flux vs distance, ^{239}Pu and ^{238}U photopeaks, NaI detector.

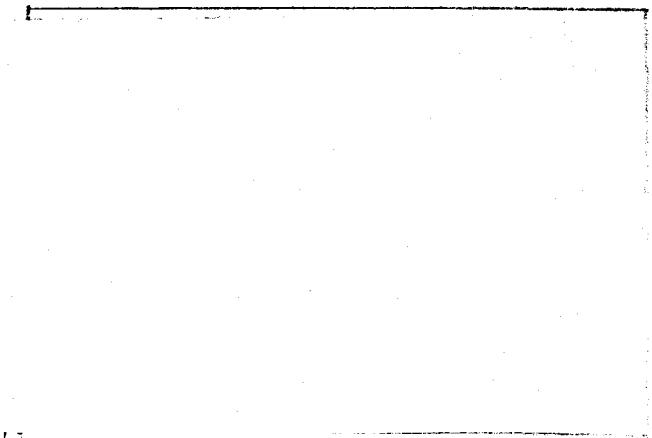

Fig. 10.
Mk-43 photopeak flux vs distance, ^{239}Pu and ^{238}U photopeaks, NaI detector.

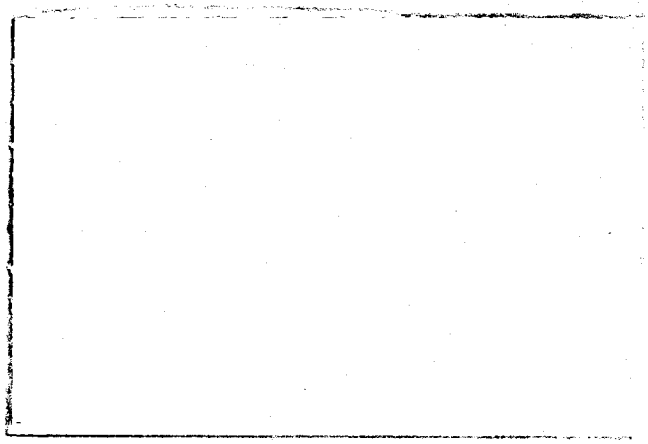

Fig. 11.
Mk-53 photopeak flux vs distance, ^{238}U photopeak, NaI detector, end-on view of secondary.

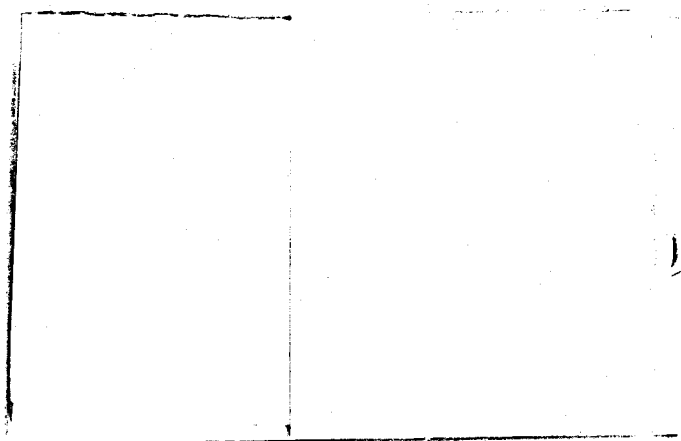

Fig. 12.
W-68 gamma spectrum, 3- by 3-in. NaI at 20 ft, 10-min count.

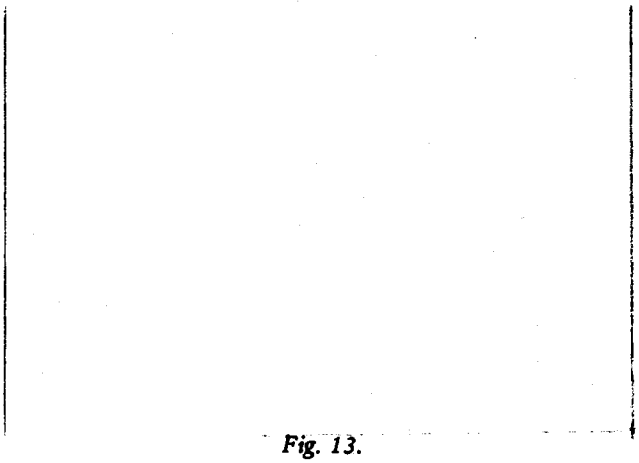

Fig. 13.
W-62 gamma spectrum, 3- by 3-in. NaI at 20 ft, 20-min count.

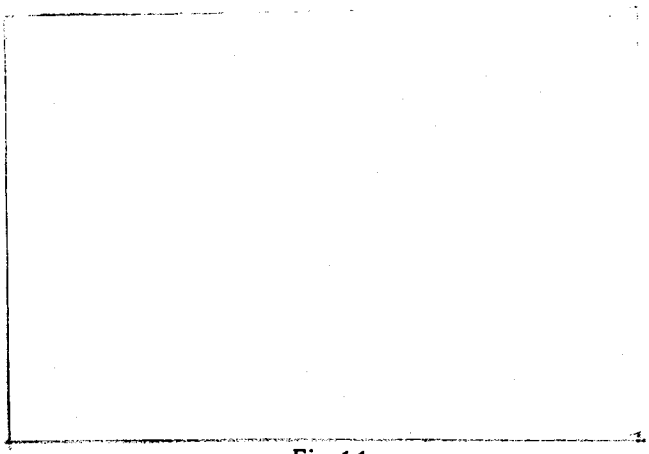

Fig. 14.
Mk-43 gamma spectrum, 3- by 3-in. NaI at 20 ft, 10-min count.

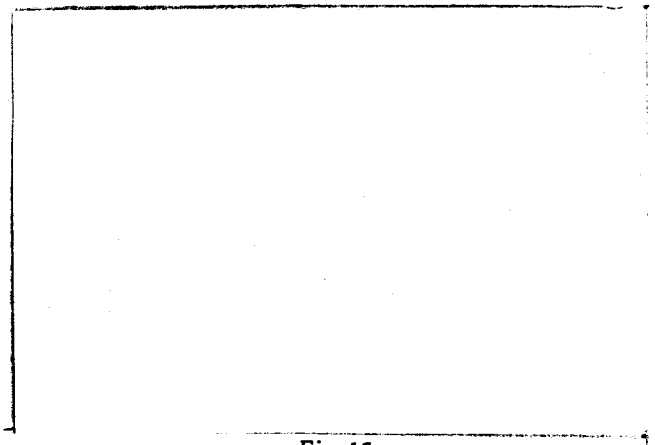

Fig. 15.
Mk-53 gamma spectrum, 3- by 3-in. NaI at 20 ft, 20-min count, end-on view of secondary.

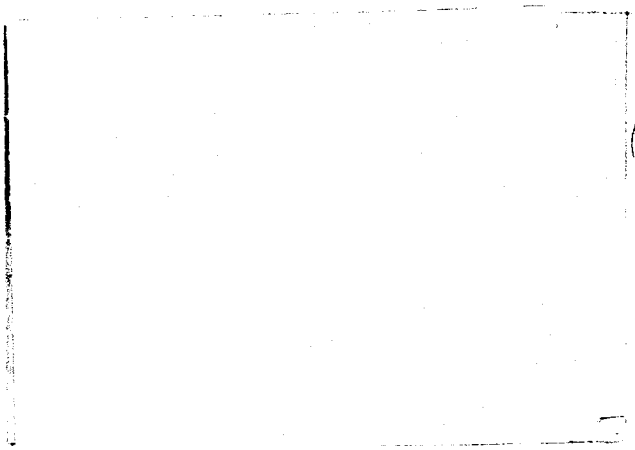

Fig. 16.
Background gamma spectrum, NaI detector, 20-min count.

All systems were viewed from the side except the Mk-53, which was viewed from the secondary end. All collimation was to 51° FOV except for a 33° FOV used for the W-59. All systems were bare except the W-59 and Mk-53, which were in their shipping containers.

Questions regarding collimator FOV can be answered rather simply. [redacted] This dependence will not begin to set in until the FOV becomes larger than the object under view, and the distance from the device is several times the largest linear dimension of the source. Ideally, the collimation should be tight enough for the inspection distance chosen so that the object viewed nearly fills the

TABLE VI

MEASURED PHOTON FLUX AT 20 FT
(γ/cm^2/sec)

	Gamma Energy (keV)		
Device	400 complex	766	1001
[redacted]			

(a) Parentheses indicate a very approximate value. See dashed line in Fig. 10 and spectrum in Fig. 14. All further calculations using this number are also approximate.

collimator aperture.

b(1) This optimum collimation depends, of course, on the size of the target and the inspection distance and implies a significant weight associated with the shield.

The Task 11 mission analysis included calculations of photopeak flux from three specific weapon models. None of the present measurements were made on the models calculated. However, from design similarity arguments the measured results can be roughly scaled to compare to the contractor calculations. Agreement by a factor of two to three is considered reasonable considering the calculational approximations.

4. Minimum Counting Time for Detection. From the measured fluxes at 20 ft (Table VI) and the 18% Ge(Li) efficiency curve in the appendix, the photopeak count rates expected for the various sources were tabulated and are shown in Table VII.

(1)(3)

Two factors influence the conversion of these count rates to detection time. The simplest is that there are no universally accepted criteria for minimum detection. The work of Currie[10] points out that differences of over a factor of 30 can appear for reasonable but differing criteria. The most serious problem, though, is the strong dependence of the minimum counting time on background. The details of the background expected in a b(1) detector are difficult to calculate because of the number of parameters involved and our incomplete knowledge of them. The space radiation background is discussed further in Sec. VI and in Appendix C, but for the present minimum detection time calculations are based on the backgrounds observed in shielded detectors in actual measurements on weapons. Here background is defined as the continuum on which the photopeaks ride. In the absence of large external sources, most of the background under the photopeaks arises from Compton scattering in the source and the detector. In this low background case both the magnitude and shape of the background are source-dependent. Reduction of some of this background by Compton suppression techniques is discussed in this section.

Backgrounds observed in measurements on the W-59 at 20 ft with a 6% Ge(Li) detector have been scaled up to the larger 18% Ge(Li) detector (shielded) and are listed in Table VIII for 2048 channels at 1.4 keV/channel.

Sophisticated computer techniques that search spectra for photopeaks and then analyze the peaks for energy and area are commonly available. One such code[11] (SAMPO) was used in this program to develop criteria for minimum area photopeak detection.[12] This work considered: (1) the probability that background fluctuations would be identified incorrectly as true photopeaks and (2) the probability that true photopeaks would be discarded in the process of discriminating against fraudulent peaks from background fluctuations. These probabilities were analyzed in terms of the background under the photopeak, and minimum counting time criteria were developed. However, this work considered only one width of photopeak, and the results are not universally applicable. The analysis is being extended, and eventually these computer search techniques will probably be more sensitive than the method outlined below. The latter, and more conservative, approach is adequate and perhaps desirable for system planning purposes.

The detection criterion assumed here is that the photopeak height is five times the standard deviation of the background points under the peak. The peak area of the assumed Gaussian peaks is simply related to the full

TABLE VII

PHOTOPEAK COUNT RATES
(counts/min)
18% Ge(Li)–at 20 ft

Device	Gamma Energy (keV) 375	414	766	1001
(6)(3)				

[a] Parentheses indicate very approximate value.

TABLE VIII

ESTIMATED MINIMUM BACKGROUND COUNT RATES

	E_γ (keV) 375	414	755	1001
Counts/min/channel	3	2.5	0.85	0.25

width at half maximum (FWHM) and height of the peak by the equation:

$$\text{Area} = 1.064 \times \text{Height} \times \text{FWHM}.$$

Using this relation and the fact that the standard deviation of a background point under the peak is $R_{bk}\ T_{min}$, the following expression can be derived for the minimum counting time:

$$T_{min} = \frac{28.30\ R_{bk}\ FWHM^2}{R_{pk}^2}\ , \qquad (1)$$

where R_{bk} = background count rate under peak (counts/channel-min),

FWHM = photopeak full width at half maximum (channels),

R_{pk} = integrated photopeak count rate (counts/min).

The criteria of Eq. (1) applied to the count rates of Table VII and the background of Table VIII produce the minimum detection times listed in Table IX. A FWHM of four channels has been assumed. The larger of the following times is listed in the table: (1) the time from Eq. (1), or (2) the time to collect 50 counts in the peak. The choice of 50 counts is somewhat arbitrary but is governed by the desire for reasonable statistics in determining approximate peak areas. In cases where the latter is larger, the Eq. (1) time is listed in parentheses for possible use in scaling with background. Note that the minimum detection time defined by Eq. (1) scales directly with background.

These detection times are not overly conservative when it is considered that enough counts must be accumulated so that meaningful relative intensity measurements can be made to avoid confusion from possible countermeasures. Computer search techniques can produce minimum count times that are lower than those in Table IX, but the resulting peak area accuracy does not allow relative intensity measurements. It has been shown[10] that count times for quantitative intensity determinations can be greater than the minimum times for detection by as much as a factor of 10.

TABLE IX

MINIMUM DETECTION TIME IN MINUTES

Device	Energy (keV) 375	414	766	1001

5. Compton Suppression Spectrometers. A non-exhaustive search of the literature on Compton suppression and anticoincidence shield techniques was unsuccessful in the sense that very little information was found on systems that would be suitable for satellite applications. The majority of the literature describes massive fixed-installation laboratory systems.

Ultrahigh resolution Si(Li) and Ge(Li) x-ray detectors with responses down to a few kiloelectron volts are common laboratory items. The small size of these low-energy detectors precludes their use at the present time, but such a detector has been used to illustrate the above points. As an example, the spectrum from a 0.003-in. ^{238}U foil was compared with that from a

A mantled detector is considered in greater detail in Sec. VI and in Appendix C.

6. Characteristic X-Rays. Detectable x-ray emissions from nuclear weapons have been studied to determine the quantity and quality of intelligence information that might be obtained from such spectra.

There are two principal methods of producing x rays in the radioactive decay of weapons materials:

(a) Internal conversion in the daughter nucleus after the parent decay produces x rays characteristic of the daughter, i.e., uranium K x rays dominate the K x-ray spectrum of thin plutonium sources.

(b) Fluorescent K x rays are produced in thicker sources from the photoelectric absorption of higher-energy gamma radiation emitted by the same material. This effect produces K x rays characteristic of the material itself. For example, in a thick uranium source, the fluorescent uranium x rays dominate over the thorium x rays expected from internal conversion in the daughter nucleus.

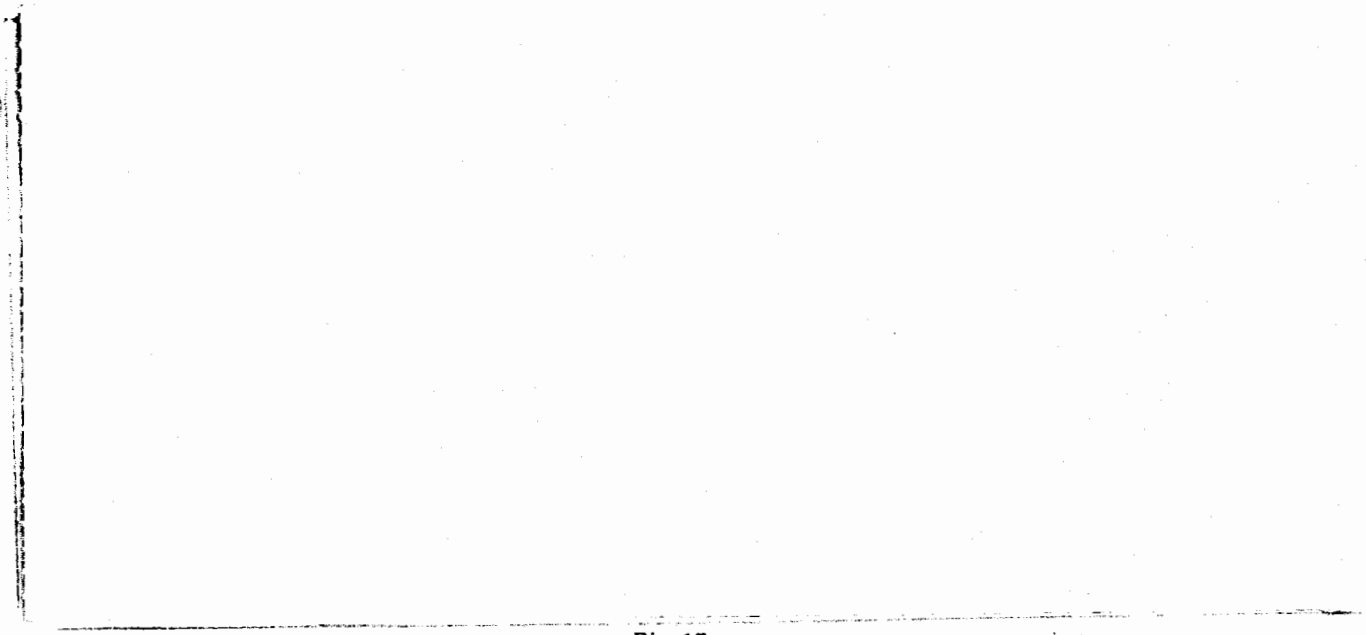

Fig. 17.
W-68 characteristic x-ray spectrum, primary end.

B. Passive Neutron Detection. The significant neutron emitters among common weapons materials are ^{238}U and ^{240}Pu, and these isotopes emit approximately 0.014 n/g-sec and 900 n/g-sec respectively from spontaneous fission.

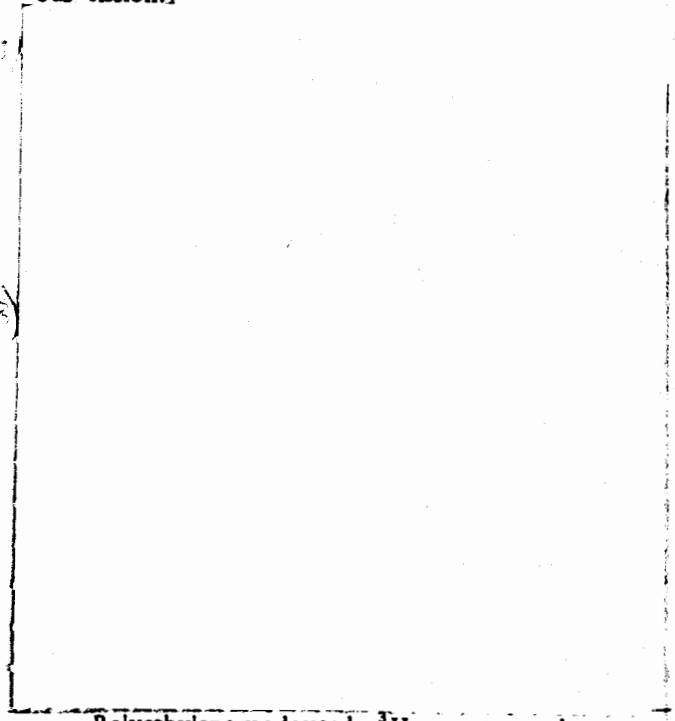

Polyethylene-moderated ^{3}He neutron detectors have been developed with intrinsic efficiencies for 1-MeV neutrons of nearly 20%.[8,13,14] For example, a detector of this type (19 ^{3}He tubes in a 20- by 24- by 3-in. polyethylene matrix) was used to detect neutrons from the W-59. The count rate as a function of distance for a side-on position is shown in Fig. 18. For this detector, the local background ranges from 5 to 10 cps.

While passive neutron detection is desirable, it is also redundant since passive gamma techniques give a more positive indication of the presence of ^{239}Pu. However, passive neutron detection is provided as an option for little cost by using the neutron detector proposed for

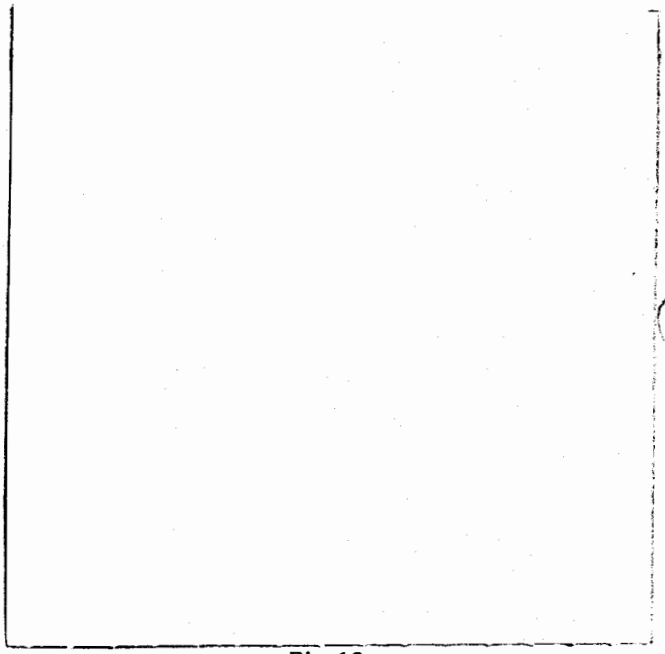

Fig. 18.
W-59 neutron count rate vs distance, 20- by 24- by 3-in. moderated ^{3}He detector.

Examples of the large collection of radiographs, including a variety of weapon types and a variety of exposure conditions, are given in the following sections along with a summary discussion.

C. Radiography.

1. Introduction. Radiography, as one of the techniques used in the satellite inspection program, can give a large amount of information concerning size, shape, and density distribution of internal components of an interrogated satellite.

The basic approach in the radiographic program was to design and fabricate an imaging system approximating a flyable system that could easily be used in a series of experimental parameter studies. The parameter studies would define a minimum energy and intensity that would produce interpretable radiographic images of nuclear weapons, as well as investigate target-associated scattering, the effects of spacecraft structure and of shielding countermeasures, and the optimization of components.

The system that was designed and assembled is described in some detail in Appendix B, along with the results of component evaluation studies. With this system a variety of nuclear weapons were radiographed under widely varying conditions. Radiographs of a W-59 were taken at LASL using the 2.3-MeV Febetron and SCAPP at 3 to 7 MeV. At the SCAPP, the W-59 was also radiographed in a variety of orientations, and sheets of absorber material were introduced in front of the weapon to simulate spacecraft structures and/or countermeasures. Experiments using radioisotopic sources were also conducted with reasonably good results. The system was also used to radiograph a Mk-45, Mk-53, W-62, and W-68 with the Pantex linac, variable in energy from 7 to 10 MeV, as the radiation source. In all cases, entire weapons were radiographed, although the pictures were in several segments when the size of the weapon dictated. Finally, conventional x-ray film radiographs were taken at all of the above radiation facilities and at the LASL betatron (22 MeV) and million-volt machine to provide a standard for comparison.

3. Experiments at the Febetron. The Febetron is a 2.3-MeV flash x-ray machine that has a nearly

*Dose measurements throughout this study were made with thermoluminescent detectors (TLD's).

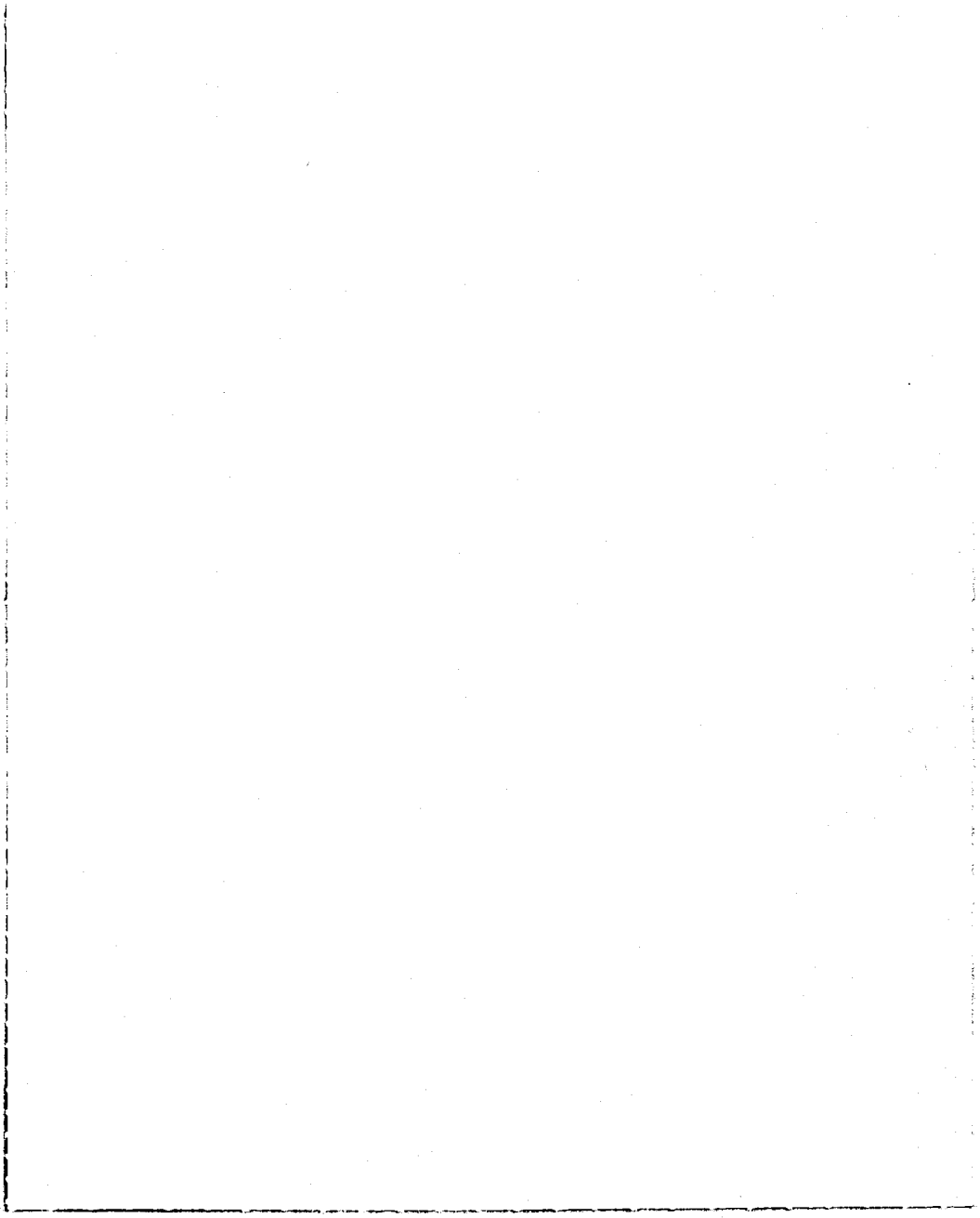

Fig. 19.
Scan of W-59 using ^{60}Co.

monoenergetic electron beam with a pulse width of ~ 20 nsec. After several radiographs were taken with both the image amplified system and with film, it was determined that the machine emitted a large amount of radiation not associated with the beam spot. A conical collimator, together with some lead shielding around the face of the machine, reduced this background to a tolerable level. Throughout the experiments a 0.025-in.-thick tantalum target was used directly behind the conical collimator and the beam spot size was defined at 1/4-in. diam.

Some beam filtering was tried in an attempt to harden the spectrum. Slightly better penetration was observed with a 1/8-in. lead filter at a cost of roughly 40% of the beam intensity. Several of the radiographs taken are shown in Fig. 20. For this sequence of shots, the

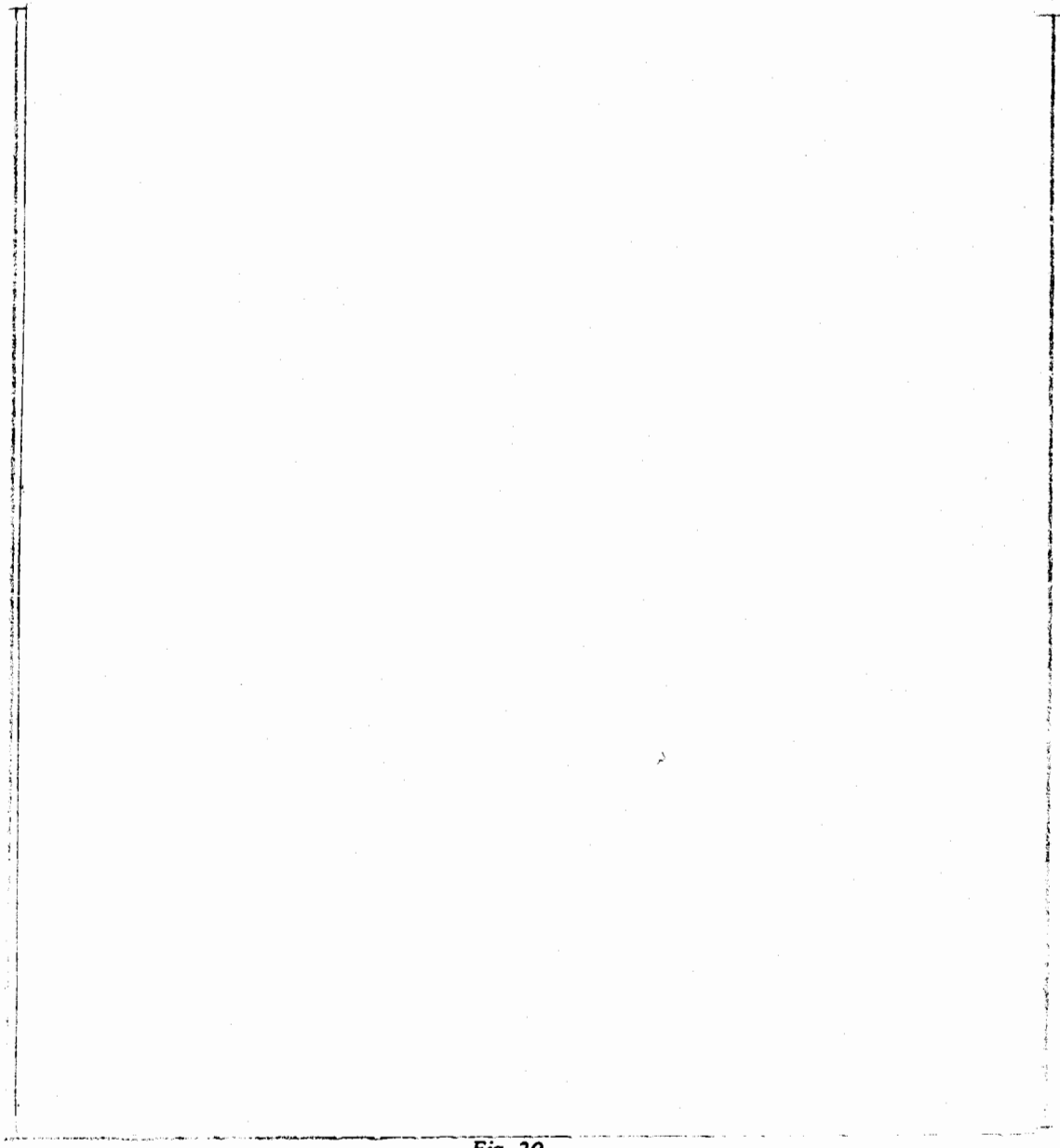

Fig. 20.
Scan of W-59 using the Febetron, 2.3 MeV.

source-to-target distance (D_1) was 22 ft and the target-to-screen distance (D_2) was 5 ft. The dose on the screen was 3 mR. The principal details of the device

are all visible in these shots.

A series of shots was made with various thicknesses of aluminum plate which simulated spacecraft structure. The shipping container was also present in all of the W-59 radiographs. Figure 21 shows a sequence covering

The first picture has no intervening attenuator, the second has a 1/4-in.-thick sheet of aluminum, the third has a 1/2-in.-thick sheet, and the fourth has a 1-in.-thick sheet. The 4- by 6-ft sheets were directly in front of the W-59. The effects were minimal even at this low energy.

4. Experiments at the Single Cavity PHERMEX Prototype (SCAPP). The SCAPP is a flash x-ray source variable in energy from 3 to 7 MeV with a 0.2-μsec pulse width and an almost monochromatic electron beam.* The spot size on target is controlled by focusing lenses near the target and by beryllium internal collimators, thereby allowing the spot size to be varied to suit the experiment. Of course, as the spot size is decreased, a penalty is paid in beam intensity on target. The radiographs taken with the SCAPP were with a 3-mm spot and with the conical collimator described earlier. Only two targets were used for all the experiments: a 0.010-in. tungsten target at 3 MeV and a 0.043-in. tungsten target at 4 to 7 MeV.

Throughout the experiments at the SCAPP, the image intensifier was operated either in a dc mode, where the tube was on for seconds; or in a pulsed mode, where the tube was on for the duration of a gate pulse synchronized with the beam burst. Several radiographs were taken using from 2 to 12 pulses.

Fig. 21.
Simulated spacecraft structure, Febetron, 2.3 Mev.

*The average current per pulse on target at 3, 4, and 7 MeV is 2.8, 6.6, and 21.6 A, which corresponds to 1.68, 5.28, and 30.2 J/pulse, respectively.

intensity on the screen varied from 1 mR ($D_1 + D_2 = 7$ ft) to 60 μR ($D_1 + D_2 = 28$ ft). This sequence of photos is shown in Fig. 23(a-e). Figure 23(a) shows a view of the primary end with a dose of 1 mR on the screen. Figures 23(b) and 23(c) are two different views with 250 μR, with 23(c) showing the [redacted] Figures 23(d) and 23(e) show the same region with 100 and 60 μR on the screen respectively. As can be seen,

b(1)

b(1)

b(1)

4 MeV. A scan at 4 MeV, taken with a 0.043-in. tungsten target, and with $D_1 = 10$ ft and $D_1 + D_2 = 12$ ft, is shown in Fig. 24(a-d). The dose on the screen for this sequence was 3 mR.

Details visible inside the radiation case

(b)(3)

3 MeV. A scan of the W-59 taken at 3 MeV, using a 0.010-in. tungsten target, with $D_1 = 5$ ft, $D_2 = 2$ ft and 3 mR on the screen, is shown in Fig. 22(a-d).

b(1)

b(

(b)(3)

A series of radiographs was taken at 3 MeV with the source-to-target distance (D_1) varying from 5 to 26 ft. Because the beam intensity remained unchanged, the

Fig. 22.
(a-d) W-59, 3 MeV. (e) W-59, 3 MeV, 1-in. aluminum, simulated spacecraft structure.

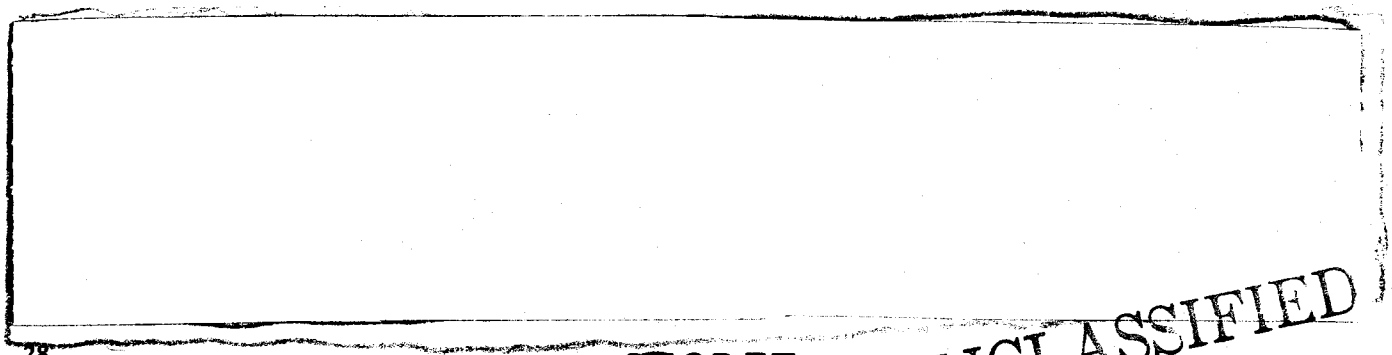

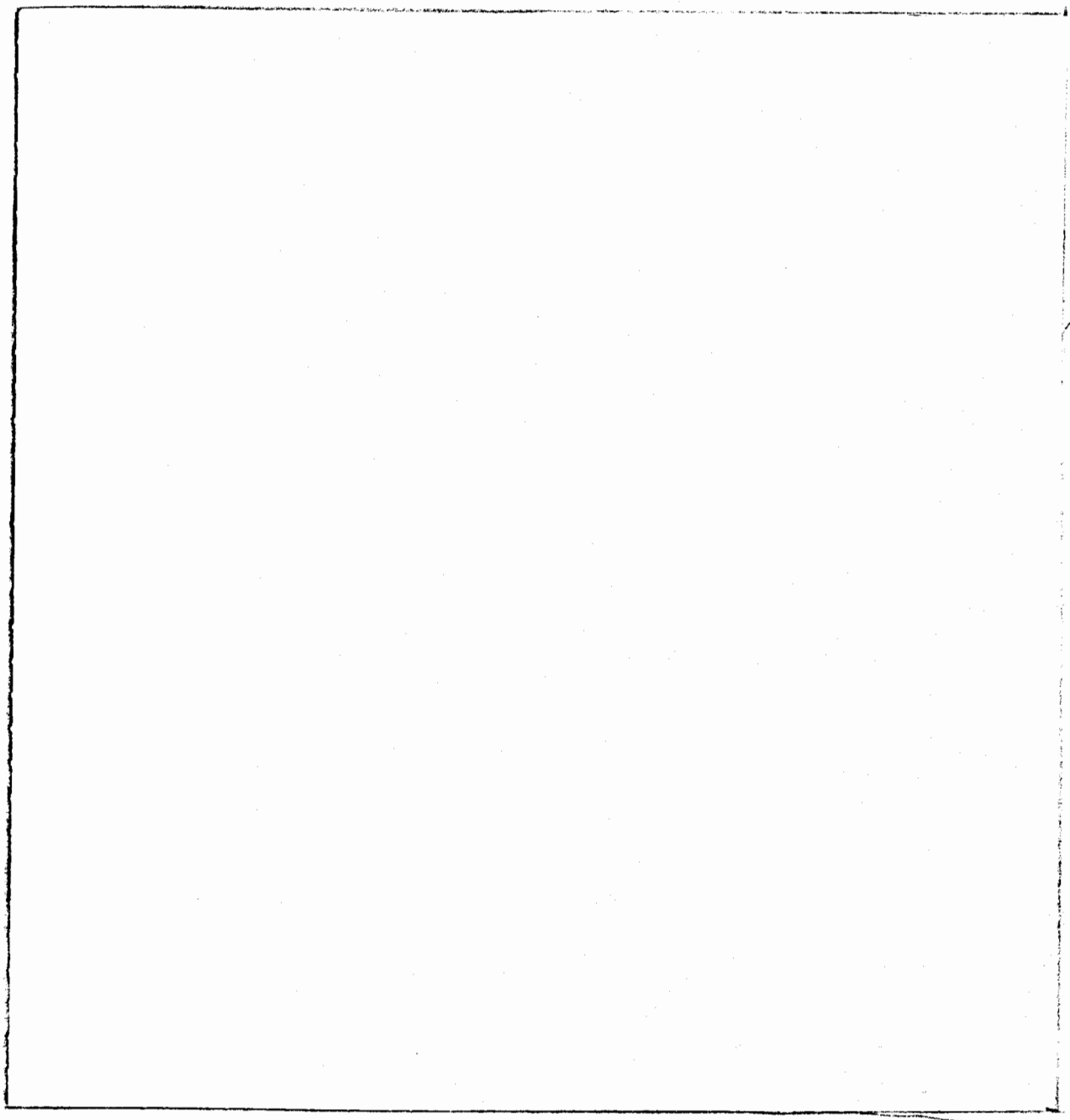

Fig. 23.
W-59, intensity variation, 3 MeV.

It is interesting to note that the Mk-53, radiographed at Pantex at 7 and 10 MeV, weighs almost 7000 lb.

A series of radiographs was made in which the intensity on the screen was varied from 1 mR to 15 μR,

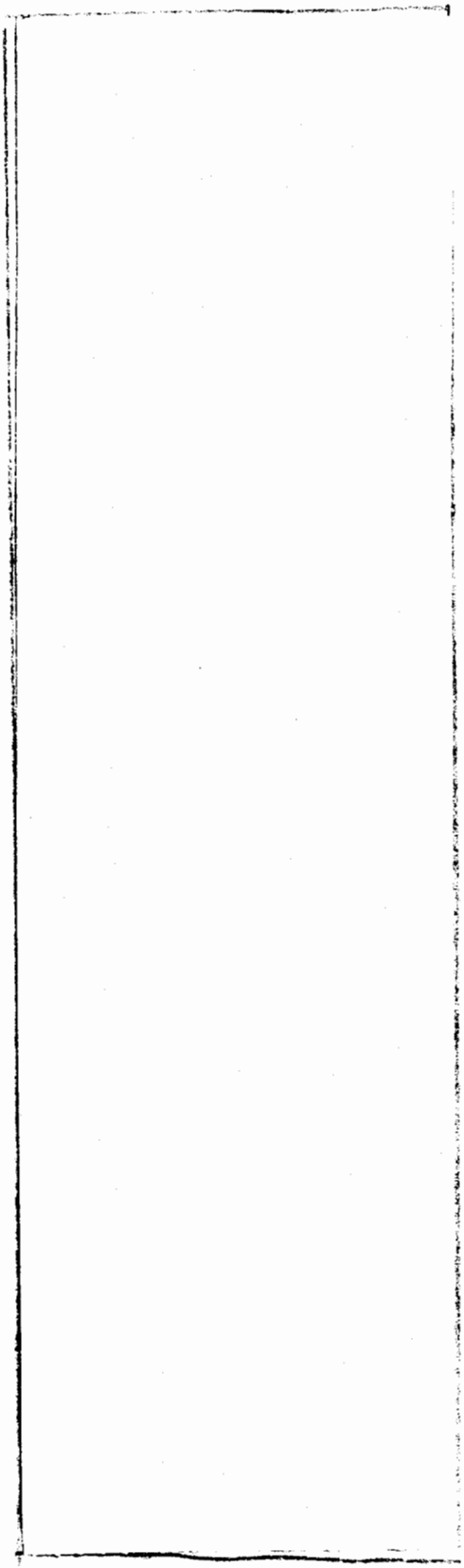

Fig. 24.
Scan of W-59, 4 MeV.

similar to the series made at 3 MeV.

The effect of source-associated background should decrease with decreasing source-to-screen distance. Figure 27(a-e) illustrates this point. This sequence of pictures was taken with D_1 = 3-1/2 ft, D_2 = 1-1/2 ft, and 10 mR on the screen.

5 MeV. Several scans of the W-59 were taken at 5 MeV using the 0.043-in. tungsten target, with D_1 = 26 ft and $D_1 + D_2$ = 29 ft. The dose on the screen for the scans was 3 mR.

7 MeV. The scan shown in Fig. 28(a-d) was taken with the 0.043-in. tungsten target at 7 MeV, with D_1 = 26 ft, D_2 = 3 ft, and with the dose on the screen equal to 5 mR.

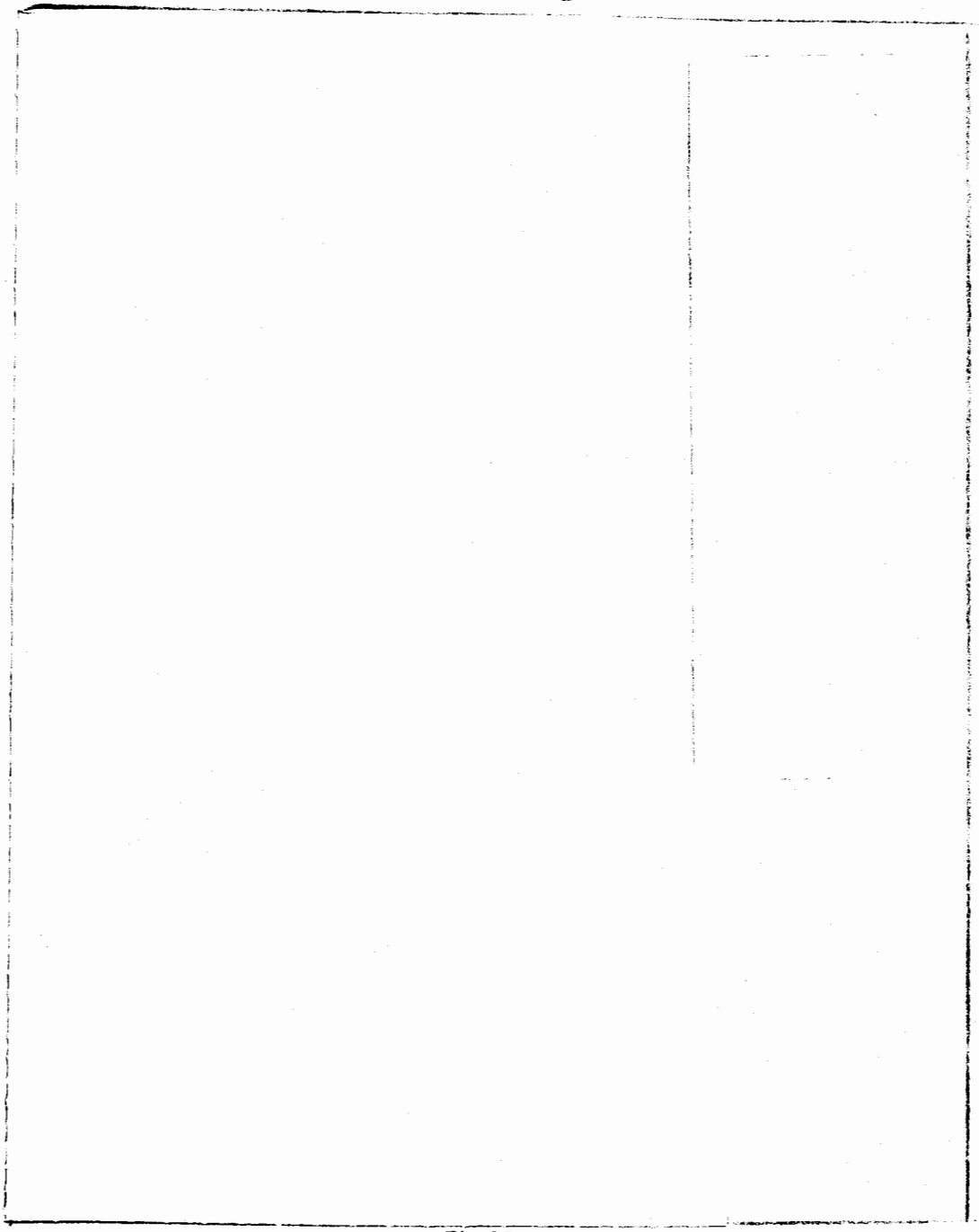

Fig. 25.
Scan of W-59, 4 MeV, 1.8 magnification.

b(1)

A few simulated spacecraft and light shielding experiments were done with $D_1 = 26$ ft and $D_2 = 3$ ft, similar to those described above using 1-in. aluminum and 1-in. steel sheets.

b(1)

b(1)
(2)

UNCLASSIFIED

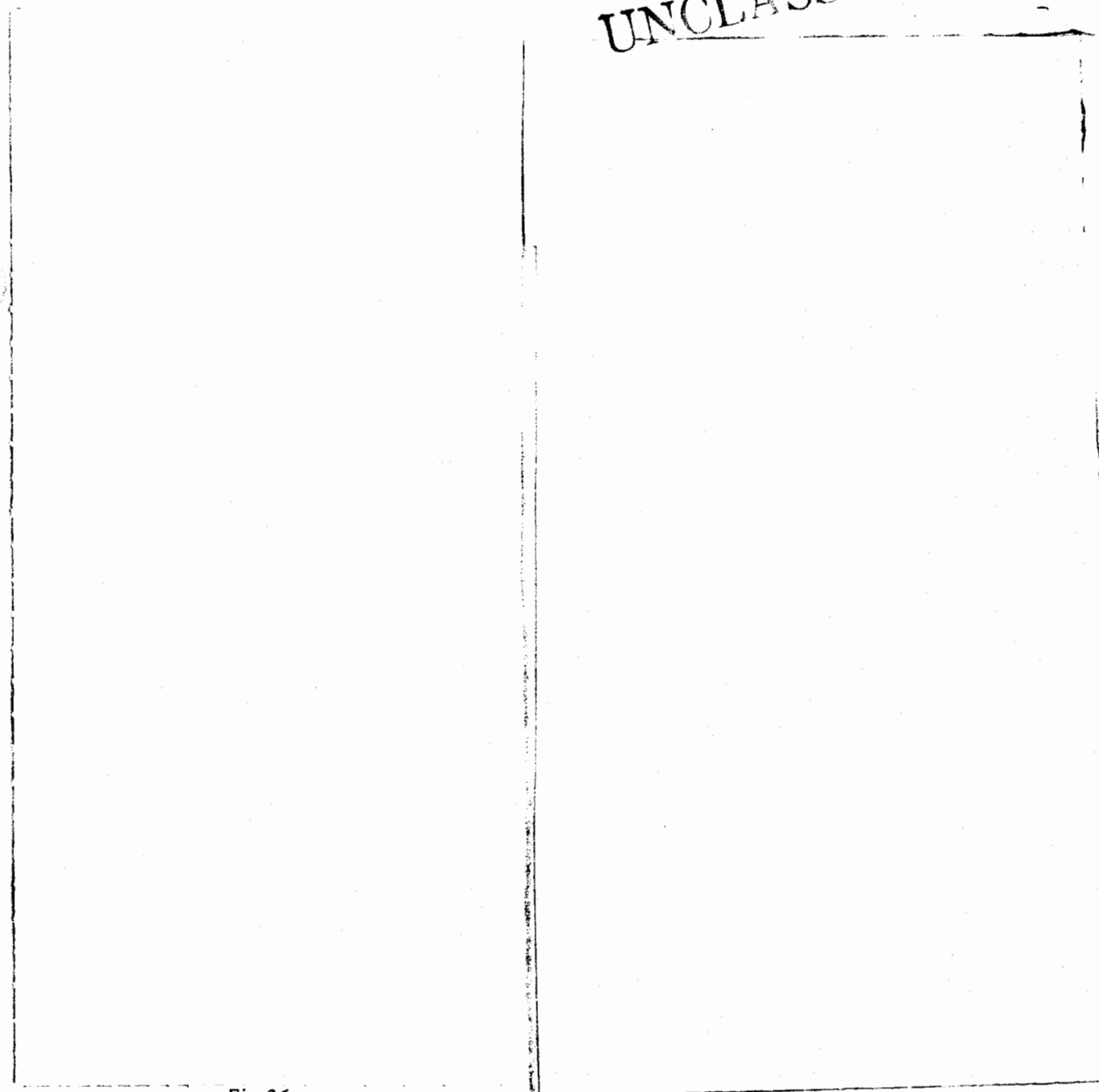

Fig. 26.
W-59, attenuation with aluminum and steel, 4 MeV. (a) No absorber. (b) 1-in. aluminum. (c) 1-in. aluminum plus 1-in. steel.

An unattenuated sequence was also taken with D_1 = 26 ft and D_2 = 39 ft. The W-59 was scanned in six frames as shown in Fig. 29(a-f). If this sequence is compared with the sequence shown in Fig. 28, it is

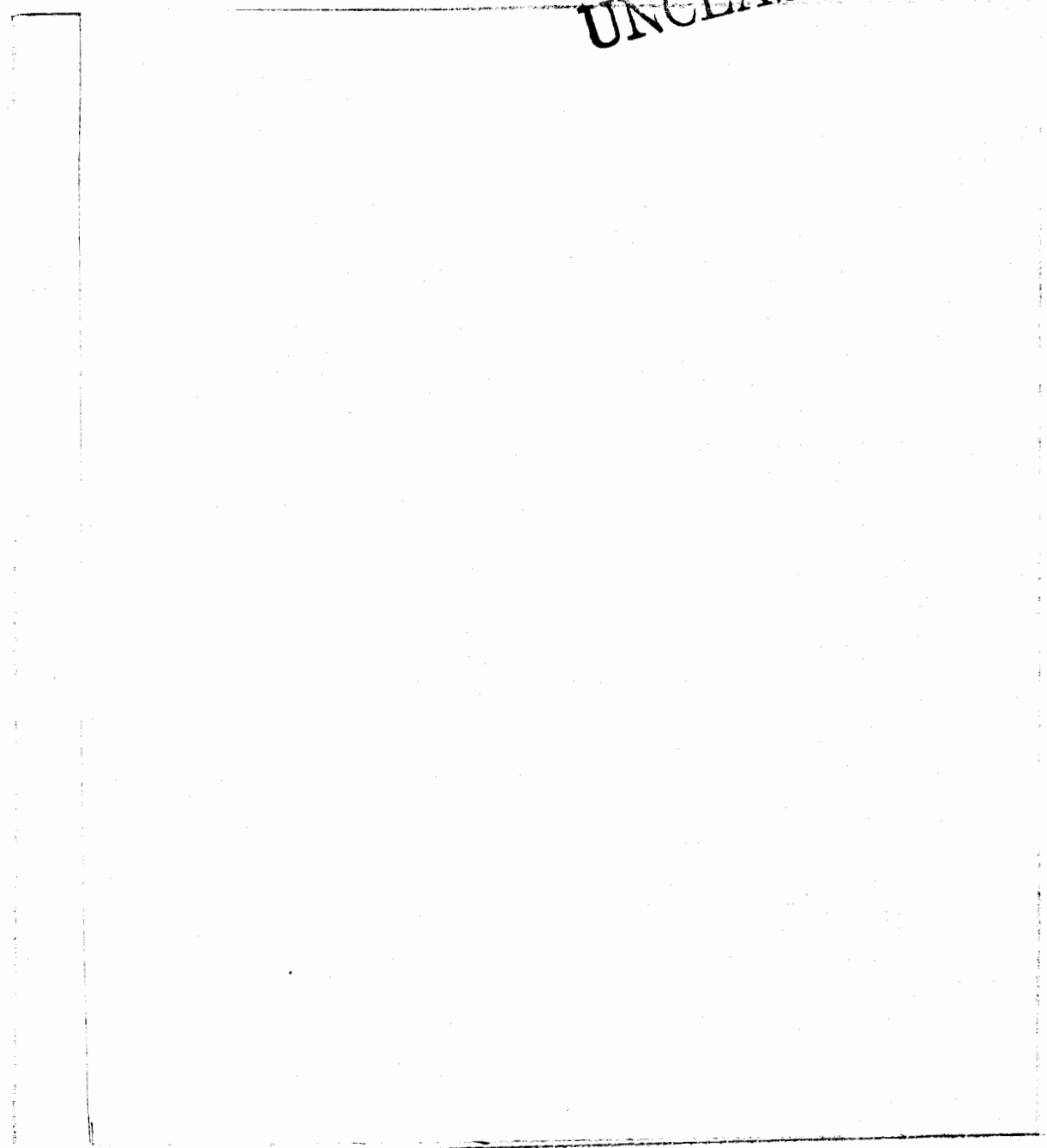

Fig. 27.

Scan of W-59 showing effects of reducing source-associated background, 4-MeV. D_1 = 3-1/2 ft, D_2 = 1-1/2 ft.

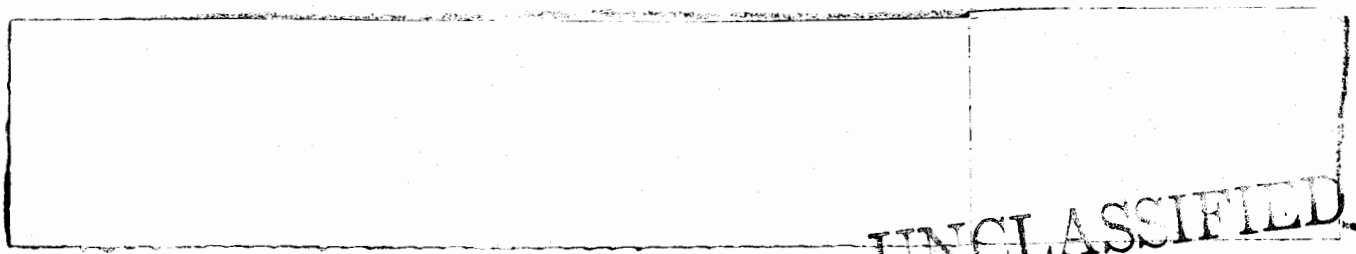

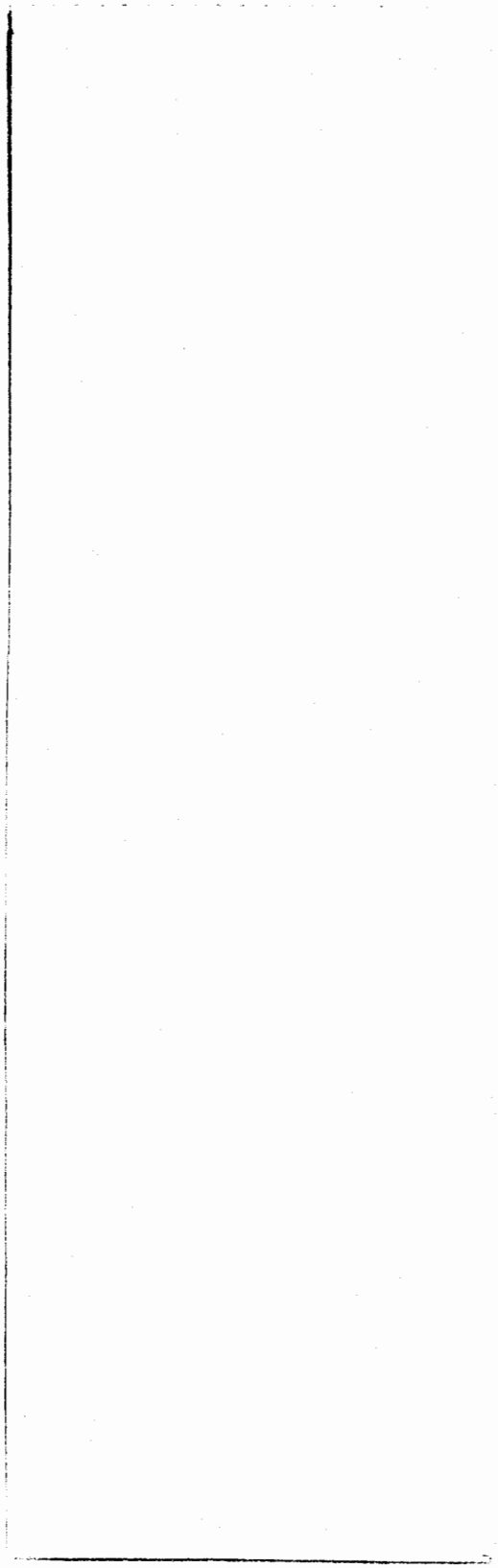

Fig. 28.
Scan of W-59, 7 MeV.

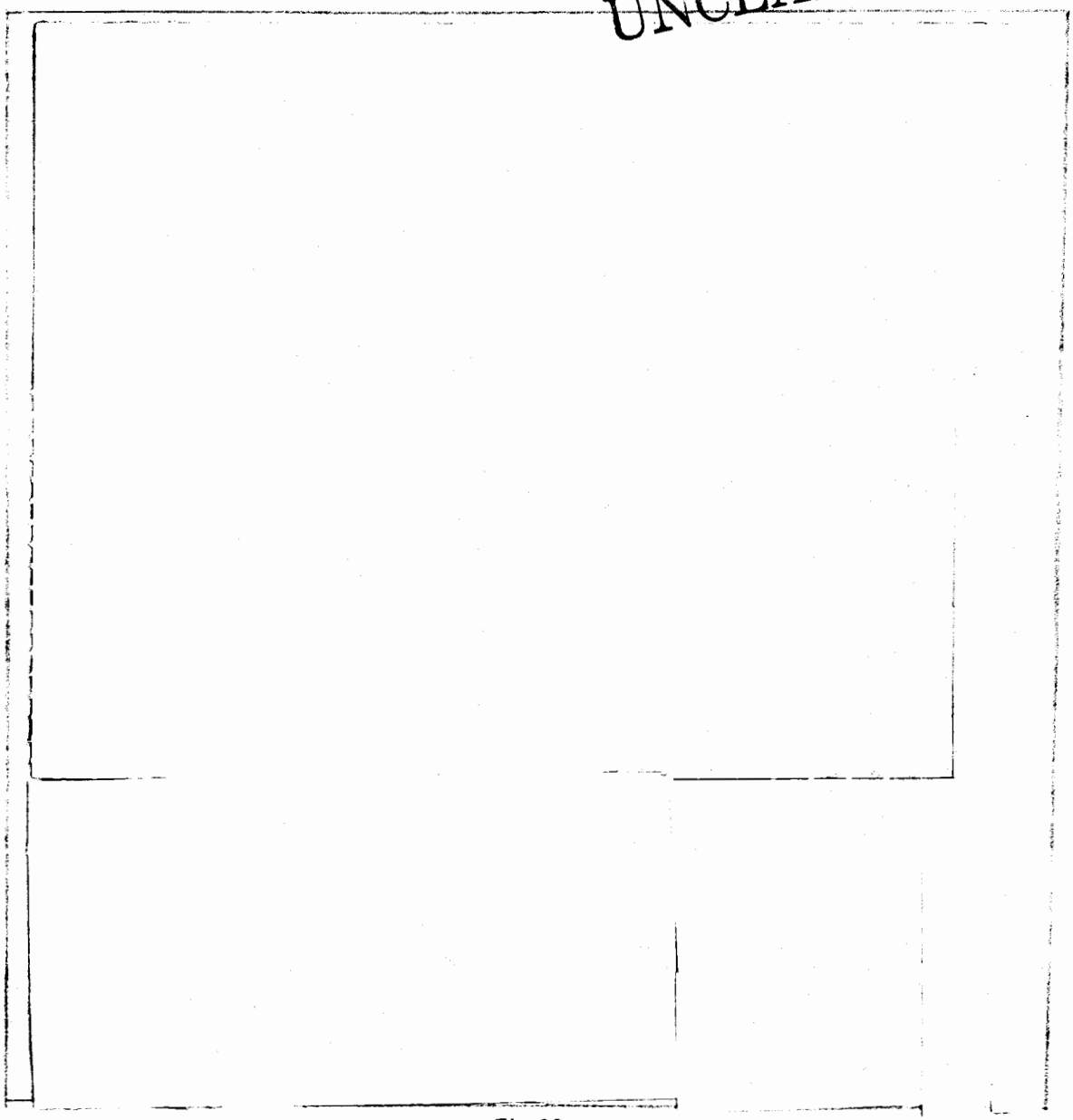

Fig. 29.
Scan of W-59, 7 MeV, 1.5 magnification.

Table X summarizes the various energies used to radiograph the W-59 using the image-amplified system and the qualitative results for penetration and definition of the principal weapon characteristics. The results of varying the intensity on the screen at a fixed energy are similarly summarized in Table XI.

5. Experiments at the Pantex Linac. The Pantex linac is a variable energy (7- to 10-MeV) linear accelerator with a monochromatic electron beam designed specifically as a radiographic source. Source-associated background from the linac was relatively low, but the room scatter contribution was more significant. The linac is housed in a concrete building with earth shielding on three walls. The maximum attainable source-to-screen distance was 25 ft, but most of the radiographs were taken with a source-to-screen distance of 19 ft.

The image intensifier was operated in both the dc and the pulsed mode. Because of the very high dose rate even at 15 pps, very short exposure times were used in the dc operation of the tube. When the image intensifier was used in the pulsed mode, a trigger pulse from the linac was used to turn on the image tube at the appropriate time.

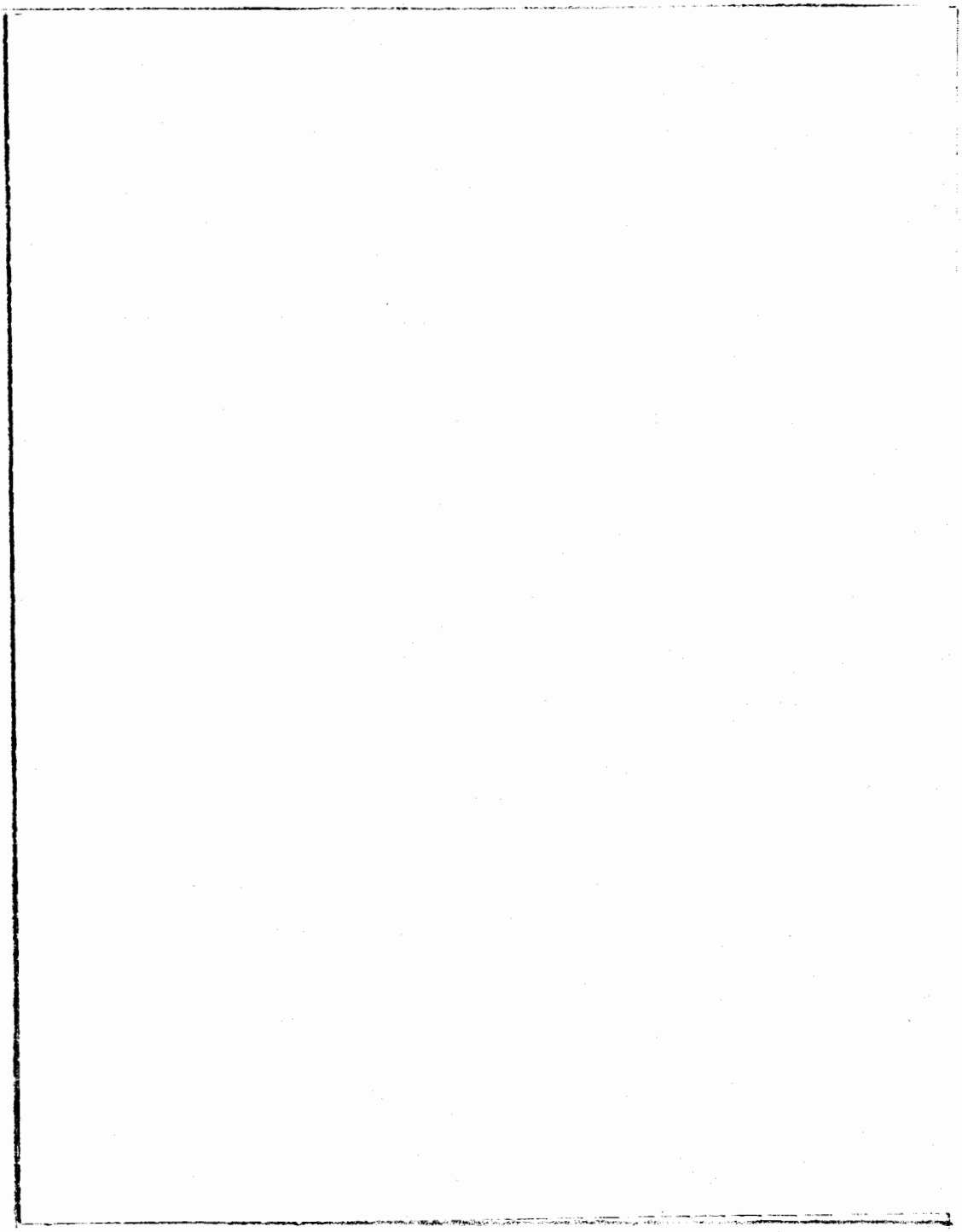

Fig. 30.
W-59, magnifications at 7 MeV.

Mk-53. The principal reason for our going to Pantex was to use the image-amplified system to radiograph the Mk-53. This weapon is the largest currently in stockpile, the basic weapon weighing 6750 lb. During these experiments, the weapon was mounted on the normal shipping truck which consists of a thin steel overcoat and a heavy structural cart (8000 lb total).

Two scans of the device were taken with D_1 = 14 ft and D_2 = 5 ft at 7 MeV.

UNCLASSIFIED

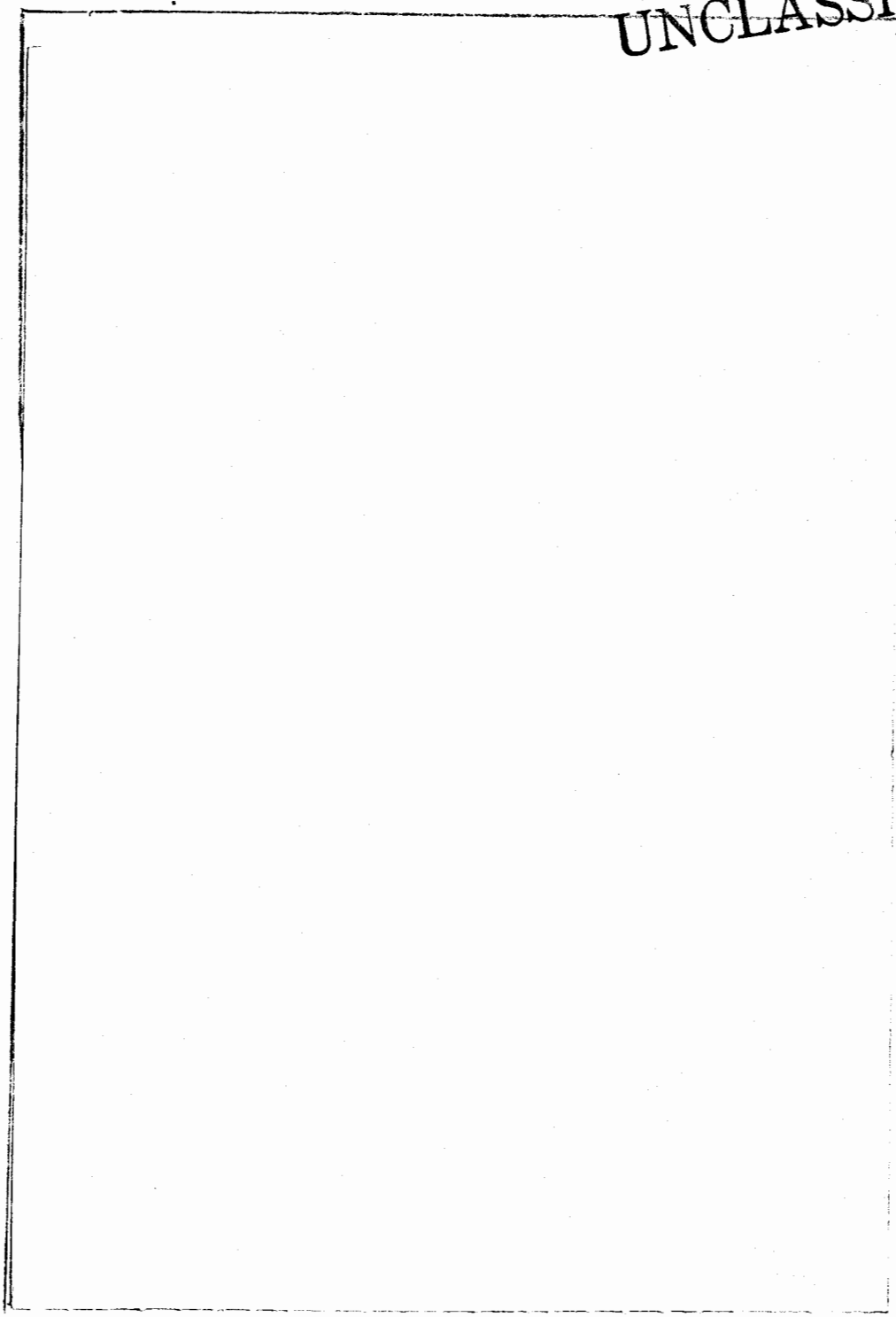

Fig. 31.
W-59, spot-size experiment, 7 MeV.

UNCLASSIFIED

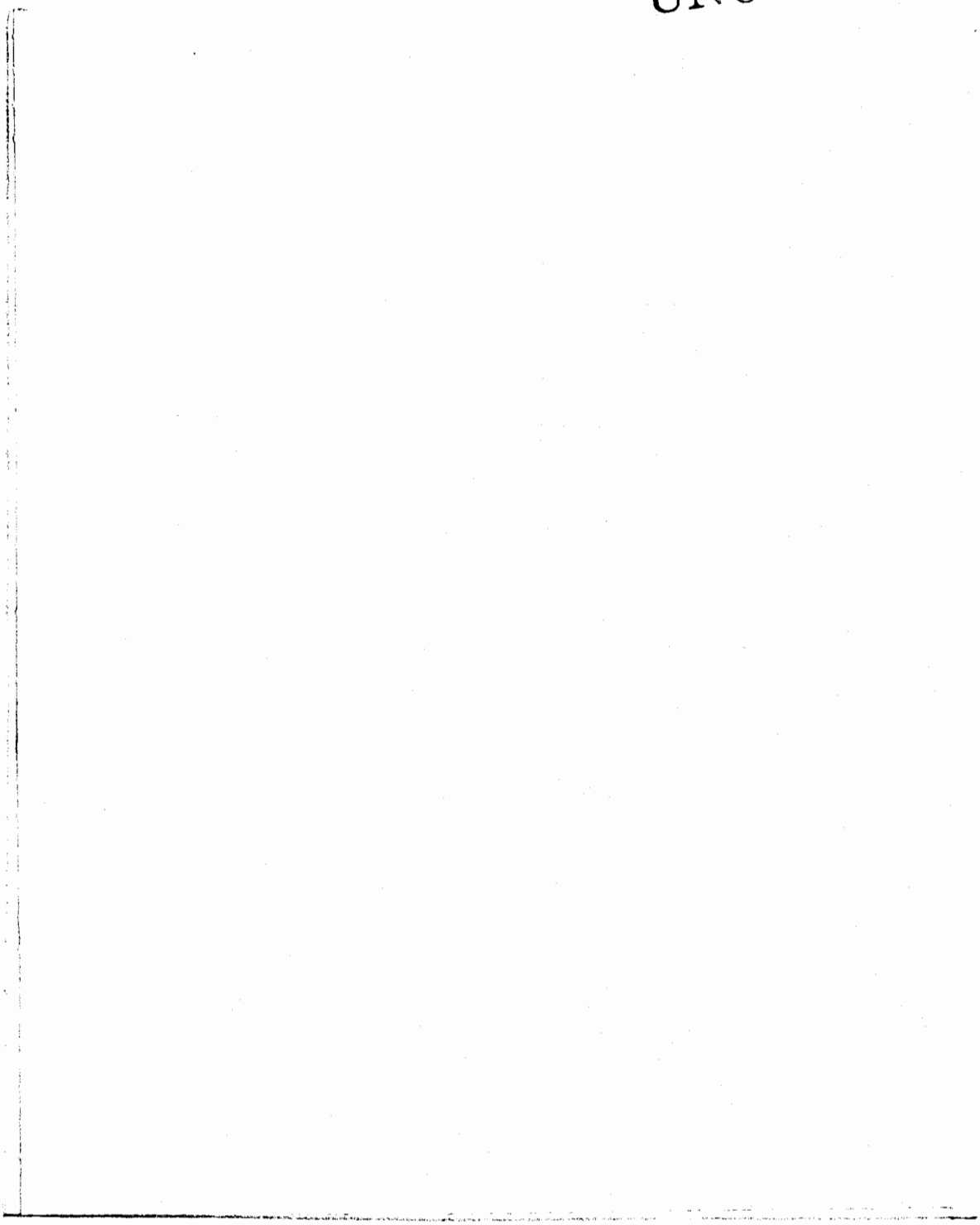

Fig. 32.
Scan of W-59, oblique angle experiment, 7 MeV.

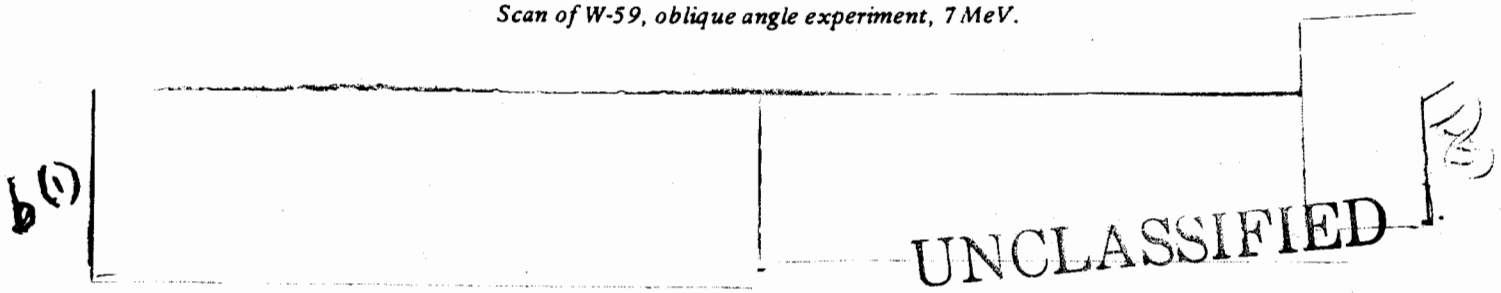

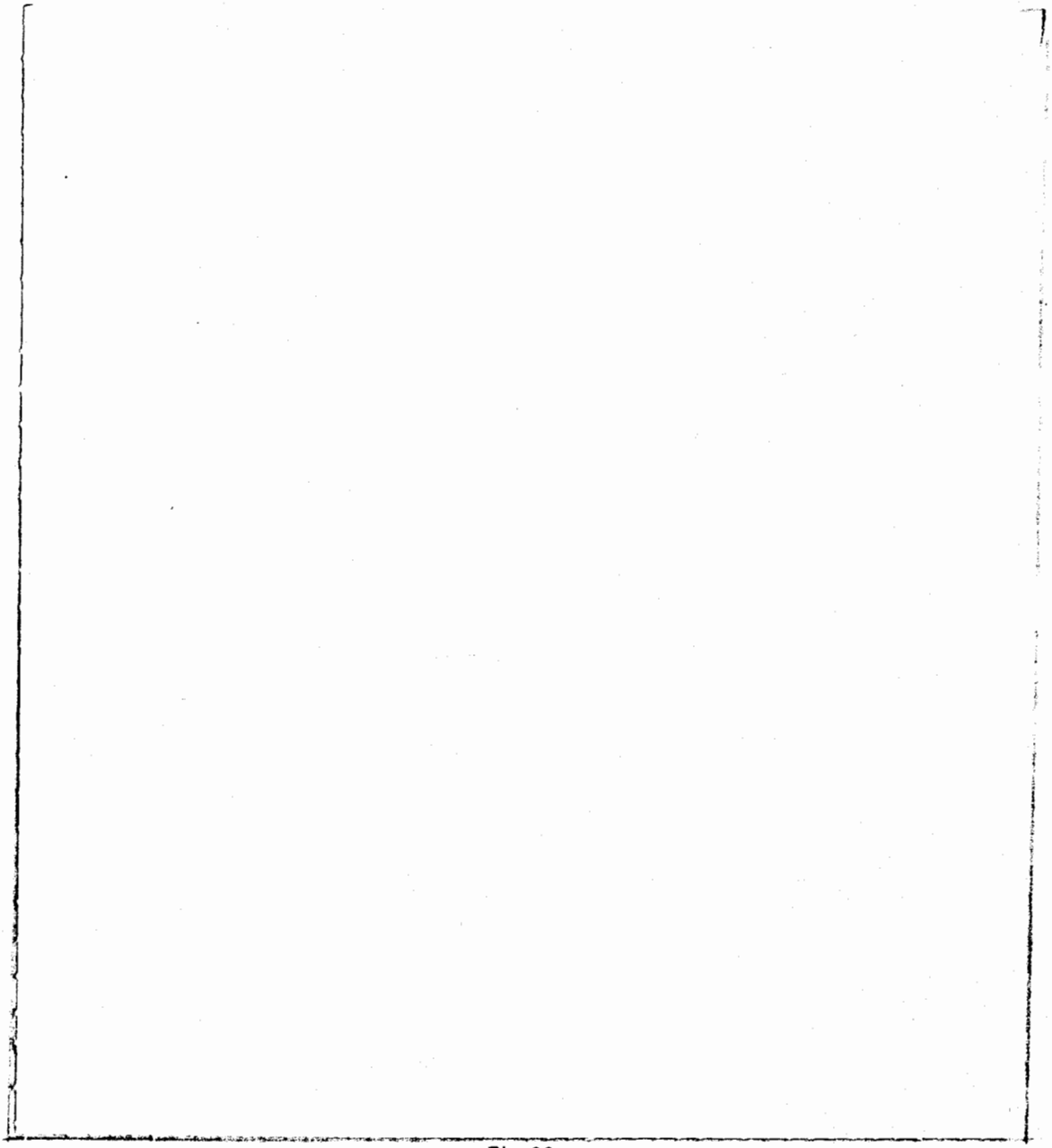

Fig. 33.
Scan of W-59 showing effects of reduction of the source-associated background, 7 MeV. D_1 = 12 ft, D_2 = 8 ft.

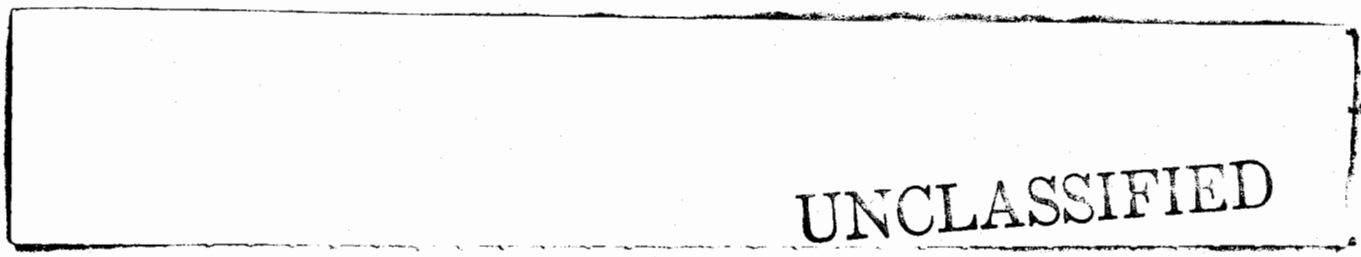

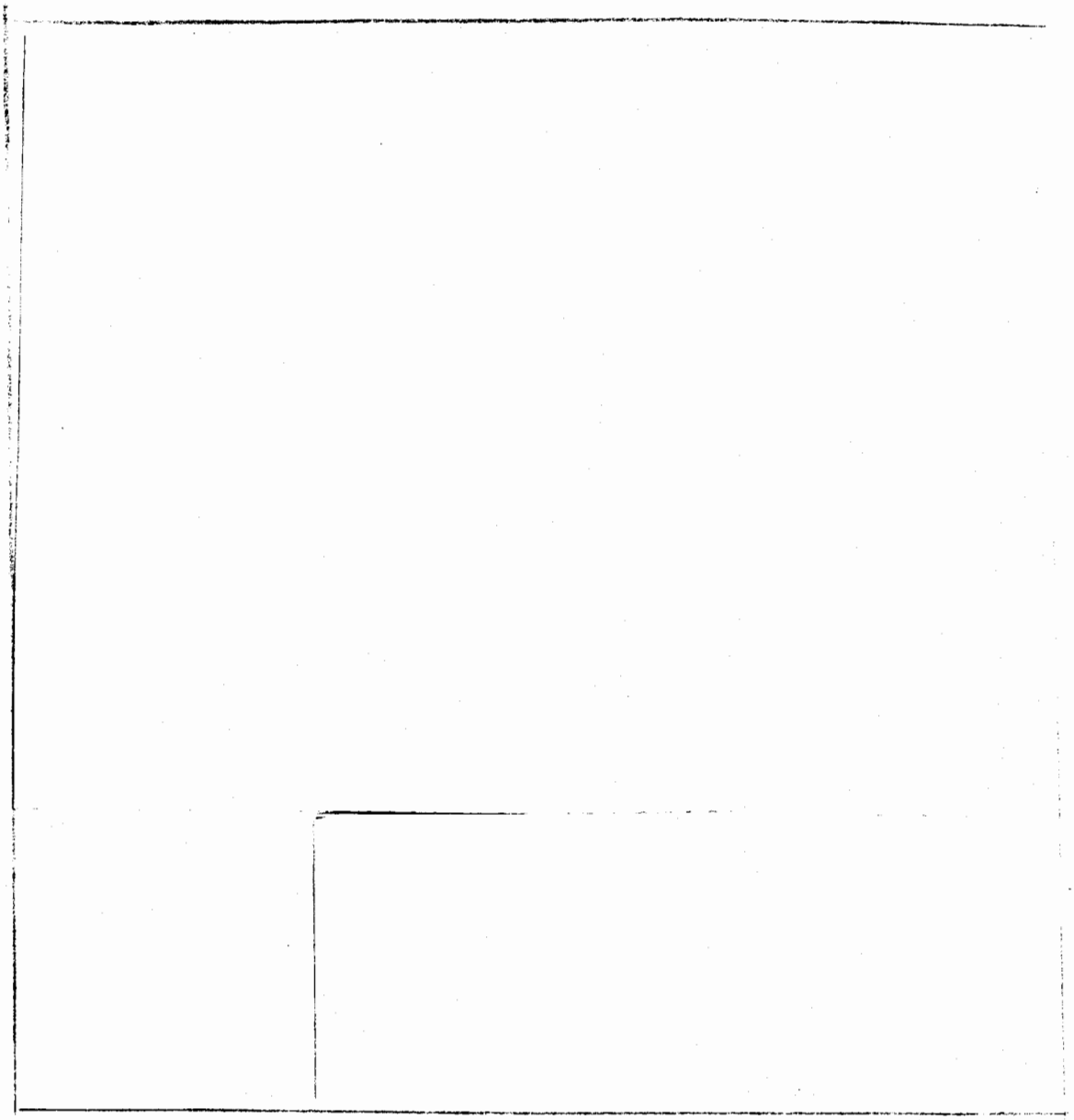

Fig. 34.
Scan of W-59 showing effects of further reduction of source-associated background, 7 MeV. (a-d) D_1 = 5-1/2 ft. D_2 = 1-1/2 ft. (e) D_1 = 3-1/2 ft, D_2 = 1-1/2 ft.

Mk-45. The Mk-45 is a small single-stage weapon, and is included here only as an example. The total weight of the device in its shipping container is approximately 150 lb. Figures 37(a) and 37(b) are two radiographs taken at 7 MeV and 30 mR on the screen but with different geometries. Figure 37(a) was taken with D_1 = 15-1/2 ft, D_2 = 3-1/2 ft, and Fig. 37(b) had D_1 = 15-1/2 ft and D_2 = 10 ft.

b(1)

b(1)

W-68. The W-68 is a small two-stage weapon used as the nuclear device in a MIRV system on the Poseidon missile. Figure 38(a-c) shows three views of the weapon taken at 7 MeV and 60 mR on the screen and with D_1 = 15 ft and D_2 = 4 ft. In Fig. 38(d), D_2 is 10 ft, slightly enlarging the device. The bar showing at the center of the secondary is a part of the shipping and handling container. The outstanding features of this

TABLE X

ENERGY VS PENETRATION

Source E	
^{192}Ir <0.600 MeV	
^{60}Co ~1.25 MeV	
Febetron 2.3 MeV	
SCAPP 3.0 MeV	
SCAPP 4.0 MeV	
SCAPP 5.0 MeV	
SCAPP 7.0 MeV	

TABLE XI

INTENSITY VS PENETRATION

Energy (MeV)	Intensity (mR)
3.0	1
	0.25
	0.100
	0.050
4.0	1
	0.063
	0.015
7.0	1
	0.100
	0.050

Definition of W-59

Fig. 35.
Mk-53, 7-MeV scan, 2mR.

In comparing Figs. 38(c) and 38(d) (D_2 = 4 and 10 ft respectively),

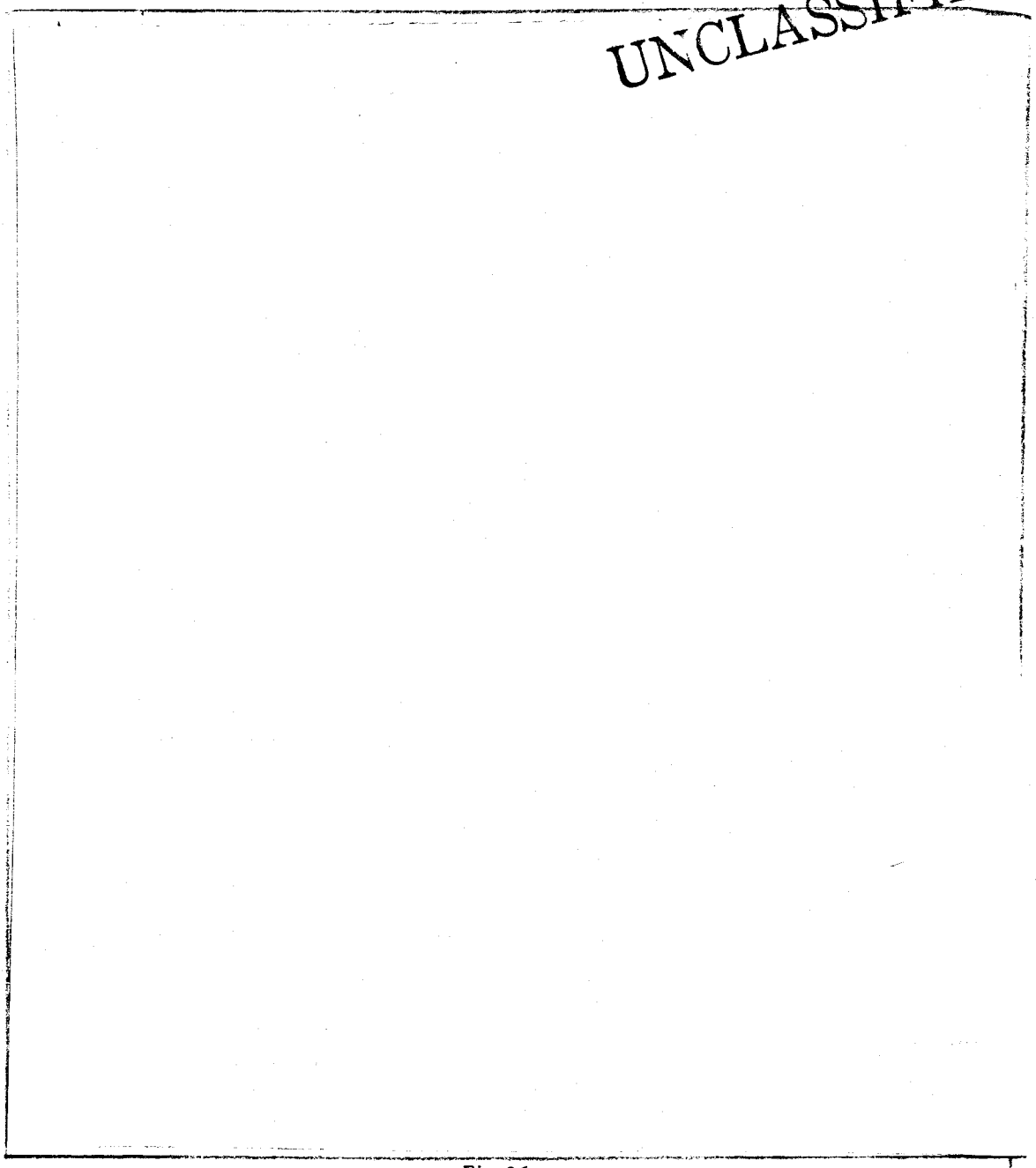

Fig. 36.
Mk-53, 10-MeV scan.

b(1)

D_2 = 4 ft

b(1)

W-62. This device is

only two views are shown in Fig. 39, with 39(a) taken at 7 MeV and 39(b) at 10 MeV, each with 60 mR on the screen. In both pictures, D_1 = 15-1/2 ft and

6. Radiographs with Standard X-Ray Film. Many radiographs were made with the standard industrial x-ray techniques commonly used at such facilities as Pantex and

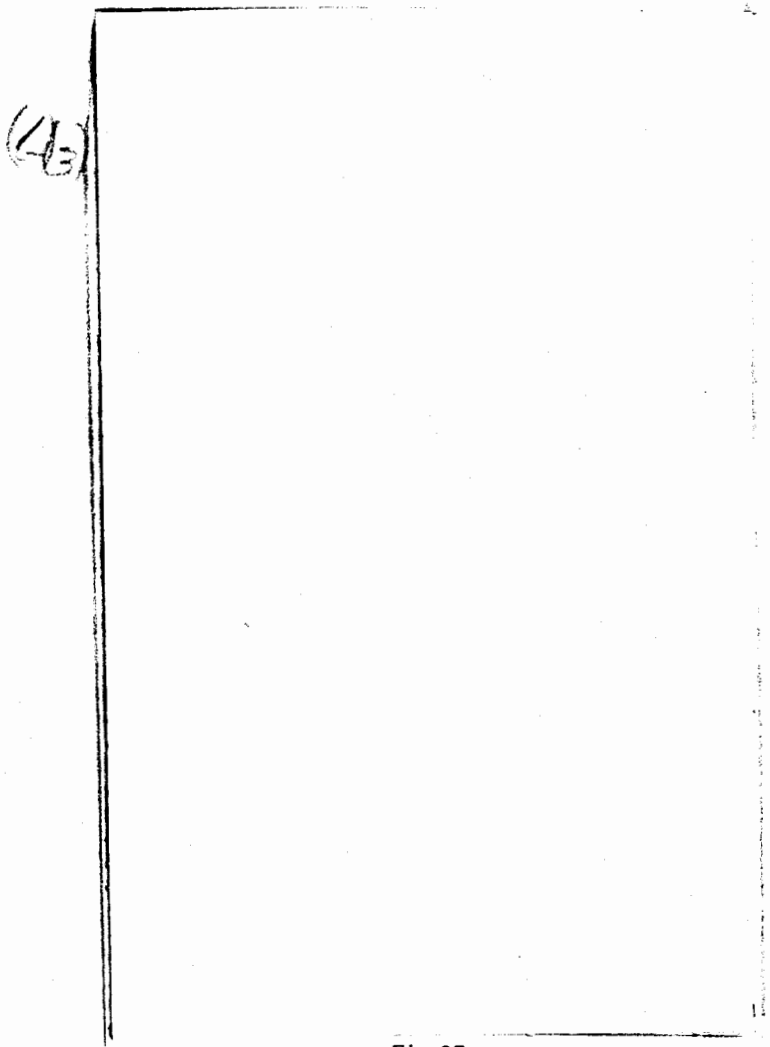

Fig. 37.
Mk-45, 7-MeV scan.

LASL Group GMX-1. Several sources were used in making these pictures, including the million-volt machine (1 MeV), a 600-mCi cobalt-60 source (1.25-MeV average energy), the Febetron (2.3-MeV flash x-ray machine), the SCAPP (3- to 7-MeV flash x-ray machine), the betatron (22 MeV), and the Pantex linac (7 to 10 MeV). The Mk-53, W-62, and W-68 were radiographed at Pantex, and a number of W-59 pictures were made at LASL.

These radiographs are not reproduced here but served several functions during the program. They indicated the quality that can be achieved by using the standard industrial techniques, served as a way of evaluating the performance of the image-amplified system, and were useful initially in establishing experimental conditions for the numerous sources.

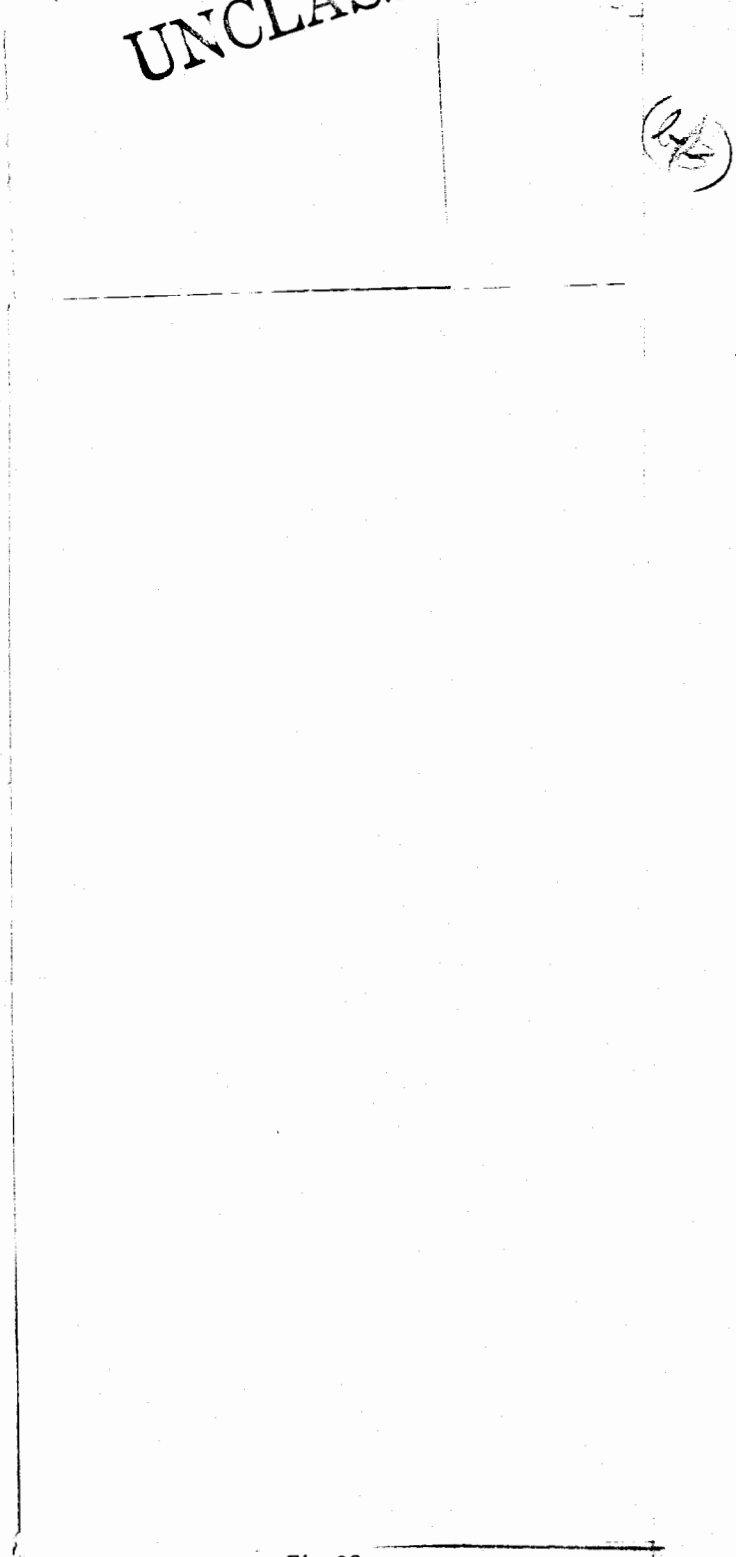

Fig. 38.
W-68, 7-MeV scan.

(b)

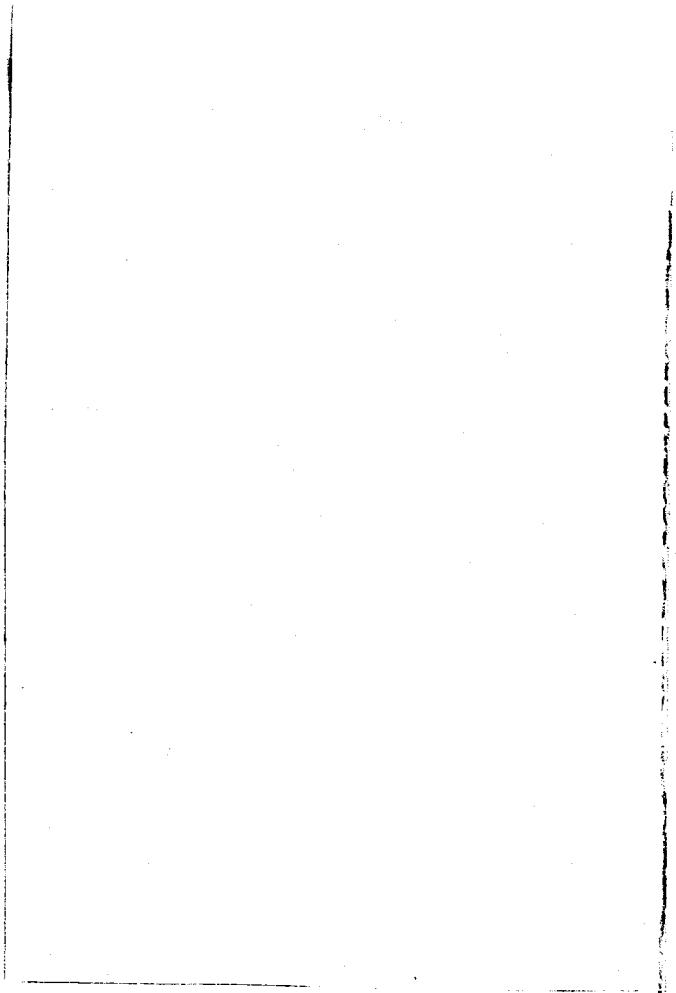

Fig. 39.
W-62. (a) 7-MeV scan. (b) 10-MeV scan.

7. Radiographic Image Enhancement. During the course of the program, the possibility of enhancing radiographic images by computer processing was considered. Some effort was expended in this area and is discussed in Appendix F.

D. Photonuclear Interrogation.

1. Radioisotope Sources.

(b)

b(1)

b(1)

b(1)(3)

2. Electron Accelerator Source Measurements.

a. Introduction. A variety of photonuclear processes can be exploited for weapons detection if bremsstrahlung radiation from an electron accelerator is available as the interrogating source. In addition to (γ,n) neutrons from ^{2}D and ^{9}Be, photofission of thorium, uranium, and plutonium isotopes can be achieved with electrons of $\geq$ 6-MeV energy. The latter reactions then make possible measurements of prompt and delayed neutrons and gamma rays. If electrons of energies $\geq$ 10 MeV are available, photoneutron production and/or isomeric state gamma-ray emission can be used to detect such common materials as lead, bismuth, tungsten, tantalum, gold, silver, copper, iron, and aluminum. In addition, the pulsed-beam capability of most common electron accelerators allows a measurement of characteristic decay times of weapon systems following photonuclear excitation, and this can be used to infer design information.

TABLE XII

(γ,n) COUNTING PARAMETERS FOR 500-Ci SOURCE

Warhead	Yield (Mt)	Net Counts and Statistical Error with 20 cps BKG	Net Counts and Statistical Error with 200 cps BKG	Average Neutron Energy (Mev)
		1880 ± 64	1880 ± 88	1.1
		1880 ± 63	1880 ± 87	~ 1.0
		4520 ± 97	4520 ± 114	0.05
		1120 ± 51	1120 ± 79	~ 0.10
		1960 ± 66	1960 ± 89	~ 0.05
		3640 ± 88	3640 ± 106	~ 0.05

b. Relative Photonuclear Yields. A general feature of bremsstrahlung-induced reactions is a steep rise in yield as a function of increasing electron energy above the reaction threshold: This phenomenon is illustrated in Fig. 40 which shows the bremsstrahlung-induced photoneutron yields for a variety of small samples over the electron energy range from 5 to 15 MeV. These measurements were made at the LASL electron prototype accelerator (EPA) with a slab-type neutron detector. Up to about 10 MeV the yields for D_2O and beryllium dominate. Above this energy photofission yields dominate. Below about 8 MeV the photoneutron yields of such high-Z materials as bismuth and lead are negligible if ^9Be, ^2D, or fissionable isotopes are present. The photoneutron yields of intermediate-Z materials such as copper and iron are negligible at all energies of interest.

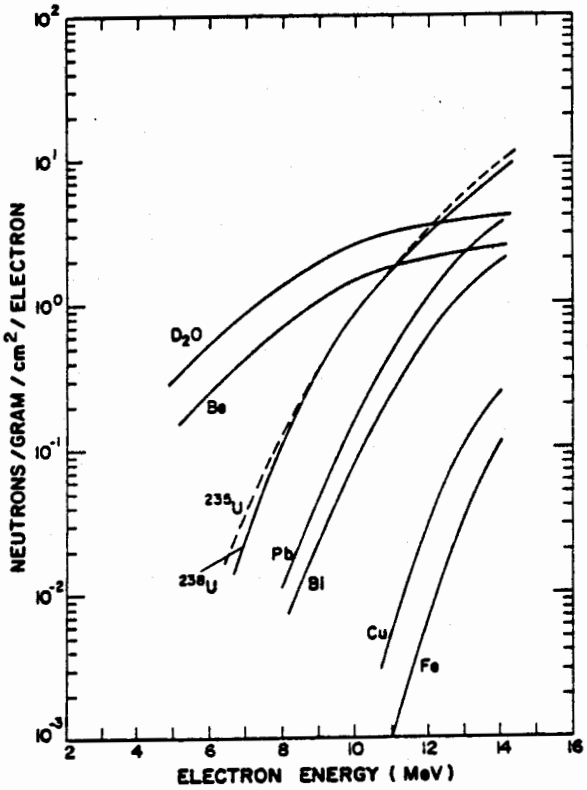

Fig. 40.
Relative bremsstrahlung-induced photoneutron yields for several materials.

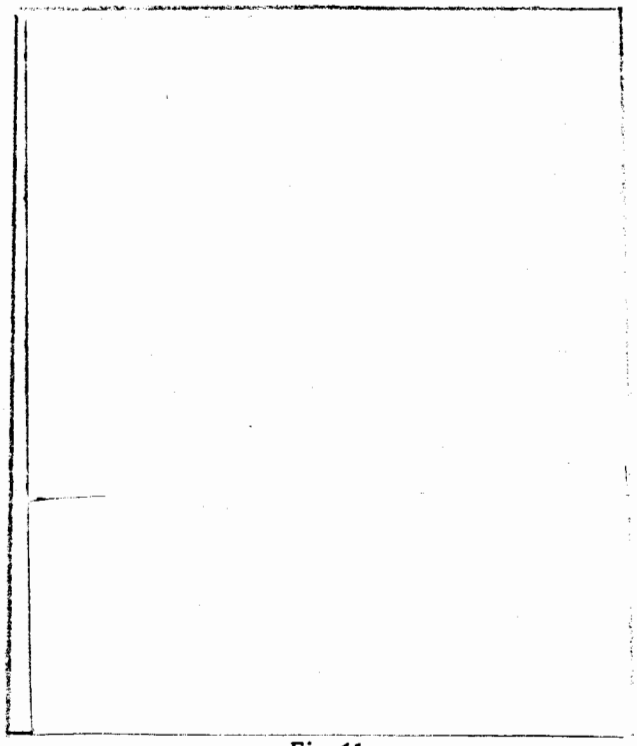

Fig. 41.
Photoneutron yield as a function of electron energy for three classes of weapon secondaries.

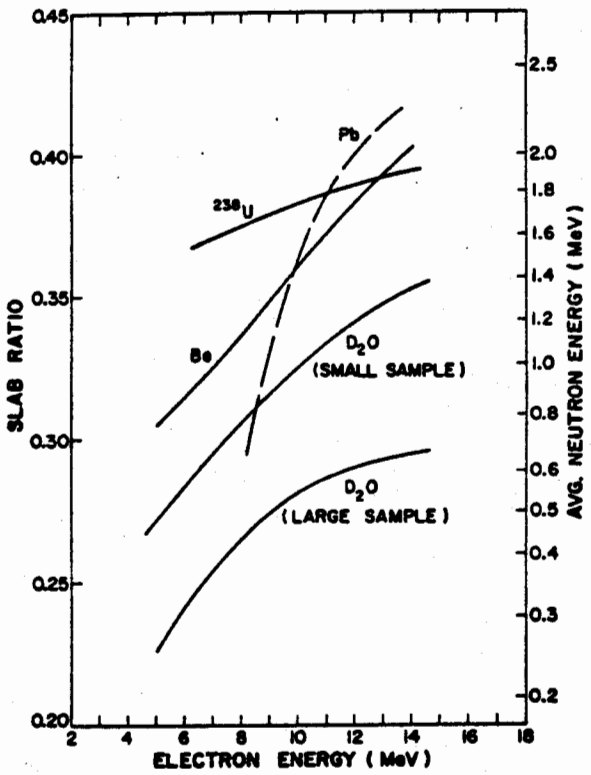

Fig. 42.
Slab-ratio data for bremsstrahlung-induced photoneutron reactions.

c. Photoneutron Spectra. The problem of beryllium determination and secondary design identification can also be approached through photoneutron spectral measurements. The description of photoneutron spectra in detail is complex; however, one general feature is a monotonic increase in average neutron energy with increasing electron energy. This is illustrated in Fig. 42 for beryllium, deuterium in heavy water samples, lead, and ^{238}U over the electron energy range 5 to 15 MeV. These measurements were made at the EPA using the slab-ratio method. As can be seen ^{9}Be has a considerably higher average neutron energy than ^{2}D for all electron energies. The average energy for a large D_2O sample is also shown in Fig. 42

The ^{238}U average energy is reasonably constant with electron energy, as expected for the fission process. This average neutron energy would also be obtained approximately for other photofissionable isotopes such as ^{235}U, ^{239}Pu, and ^{232}Th and for neutron-induced fission spectra.

b(1)

TABLE XIII

APPROXIMATE AVERAGE PHOTONEUTRON SPECTRAL ENERGIES IN MeV AT THREE ELECTRON ENERGIES

Secondary System	E_e = 5 MeV	E_e = 7.5 MeV	E_e = 10 MeV
	1.08	1.19	1.51
	1.00	1.16	1.50
	0.25	0.78	1.51
	0.50	0.89	1.50
	0.25	0.40	0.94
	0.50	0.72	1.12
	0.75	1.05	1.45

a ^{4}He proportional counter. Generally speaking, photoneutron spectral shapes and endpoints are unique for each isotope at each electron energy. Table XIV shows photoneutron endpoint energies for several isotopes of interest at three electron energies. Neutron-induced fission neutron spectra can be considered the same as photofission neutrons from ^{238}U, ^{235}U, or other photofissionable nuclei.

There is a large endpoint difference between ^{2}D and ^{9}Be at all electron energies. Considering the problem of competing reactions, however, an electron energy around 5 MeV is most interesting for beryllium-deuterium discrimination. Figure 43 illustrates the endpoint technique by showing measured beryllium and small sample D_2O photoneutron spectra for 5.35-MeV electron bremsstrahlung. These spectra were obtained by unfolding ^{4}He proportional counter spectral data measured at the EPA. Appendix D gives a description of the unfolding technique. The two spectra differ considerably in both endpoint energy (1.56 and 3.27 MeV) and shape. The spectral shape differences are due primarily to differences in the shapes of the D(γ,n) and Be(γ,n) cross sections below 5 MeV. Although the D(γ,n) cross section in this energy range is well known,[19] a literature search indicated that the Be(γ,n) cross section is not well known above 3-MeV photon energy. Competing beryllium photonuclear reactions such as (1) $^9\text{Be} + \gamma \rightarrow {}^8\text{Be}^* + n$ (2.9-MeV excited state of ^{8}Be*), (2) $^9\text{Be} + \gamma \rightarrow {}^4\text{He} + {}^5\text{He} - 2.46$ MeV (^{5}He subsequently breaks up spontaneously into ^{4}He + n with a 10^{-21} sec half-life), and (3) $^9\text{Be} + \gamma \rightarrow {}^4\text{He} + {}^4\text{He} + n - 1.57$ MeV could also occur and would make the prediction of neutron spectra uncertain even if the total Be(γ,n) cross section were known.

Figure 44 shows (1) the ^{252}Cf spontaneous fission neutron spectrum, (2) a ^{239}Pu multiplying assembly neutron-induced fission neutron spectrum, and (3) the 9.8-MeV electron bremsstrahlung-induced ^{238}U photofission neutron spectrum measured at EPA. All three spectra were measured with ^{4}He proportional counter spectrometers and unfolded using the technique described in Appendix D. All three spectra are quite similar, except for differences at low neutron energies (due to moderation effects in the multiplying assembly and a competing photoneutron reaction in the case of ^{238}U).

TABLE XIV

BREMSSTRAHLUNG-INDUCED PHOTONEUTRON ENDPOINT ENERGIES IN MeV

Isotope	E_e = 5 MeV	E_e = 7.5 MeV	E_e = 10 MeV
^{2}D	1.39	2.64	3.89
^{9}Be	2.96	5.18	7.40
Pb	(a)	0.76	3.26
Bi	(a)	0.04	2.54
^{238}U	(a)	> 10	> 10
^{235}U	(a)	> 10	> 10

(a) Below threshold for reaction.

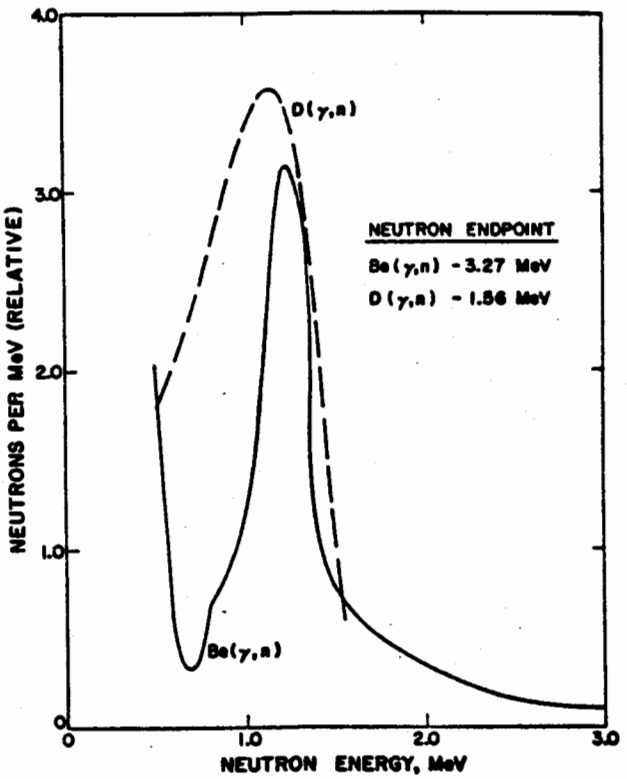

Fig. 43.
Deuterium and beryllium photoneutron spectra, 5.35-MeV bremsstrahlung.

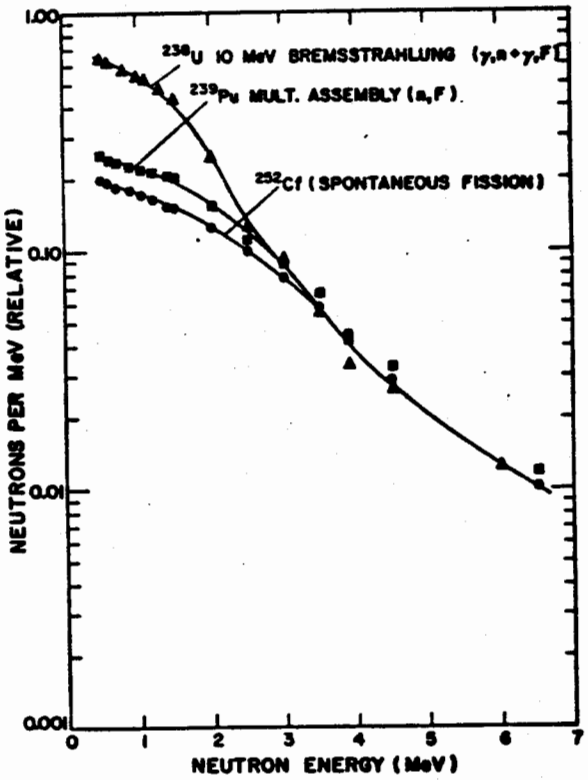

Fig. 44.
Fission neutron spectra for ^{238}U, ^{239}Pu, and ^{252}Cf.

(b)

The principal advantages of proportional-counter spectrometers are low gamma sensitivity (successful spectra have been taken in fields of > 10 R/h) and high intrinsic neutron detection efficiency ($\approx 13\%$ at 1 MeV for a ^{4}He type is realistic). Several experimental comparisons were made between ^{4}He and CH_4 tubes of identical scattering pressures (2 atm CH_4 and 8 atm ^{4}He) under a variety of conditions. This comparison between ^{4}He and CH_4 for monoenergetic 1-MeV neutrons is shown in Fig. 45. The ^{4}He tube is approximately twice as efficient as CH_4 in the maximum recoil energy region, and this translates into a correspondingly increased efficiency in applying the endpoint technique. The ^{4}He counter also has a considerable advantage in gamma sensitivity. In a $\geq$ 5-R/h ^{232}U gamma field, the ^{4}He spectrometer could be used to take good pulse-height spectra down to about 0.2 MeV, whereas the CH_4 counter suffered appreciable pulse-height degradation at 0.75 MeV. Identical electronics were used for these measurements, with high voltages for the two tubes set at their respective optimum resolution points. The ^{4}He elastic scattering proportional-counter spectrometer was thus selected for a further study of the endpoint technique. In addition, the properties of various types and configurations of ^{4}He spectrometers were studied analytically using LASL Monte Carlo computer codes. A description of the analytical work is included in Appendix E.

The basic deuterium-beryllium discrimination using the endpoint technique is illustrated in Figs. 46 and 47. Figure 46 shows the measured small sample photoneutron ^{4}He spectrometer pulse-height distribution for D_2O and beryllium for bremsstrahlung from 4.5-MeV electrons. Figure 47 shows the same for 5.35-MeV electrons. The corresponding endpoints are marked in all cases on the horizontal axes. Although these are direct spectrometer data (no unfolding), the shapes of the deuterium and beryllium distributions at a given electron energy are characteristically different, as are the endpoints. In an unknown spectrum with only D(γ,n) and Be(γ,n) components (e.g., conventional and clean weapons interrogated at less than 5 MeV), the beryllium portion could be identified and the deuterium component extracted for spectra containing a beryllium component less than a few times the deuterium component. The beryllium and deuterium

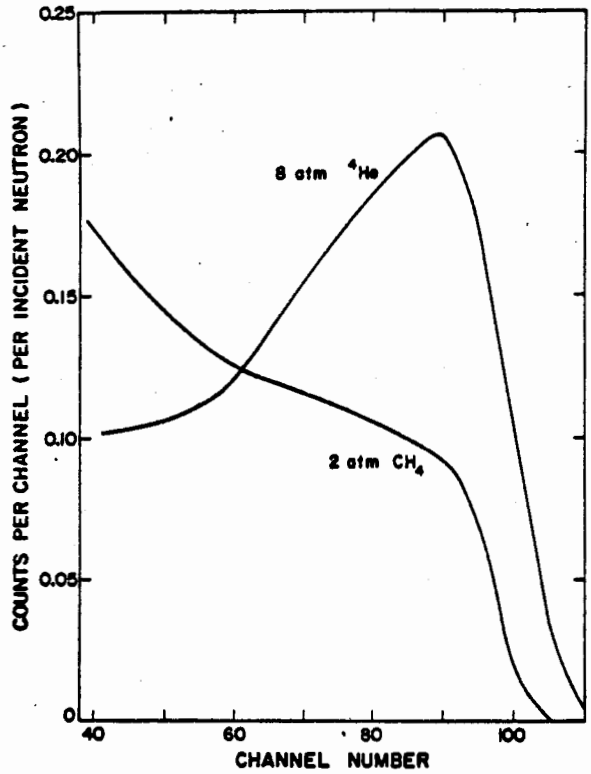

Fig. 45.
^{4}He and CH_4 1-MeV neutron response, neutron spectrometer comparison.

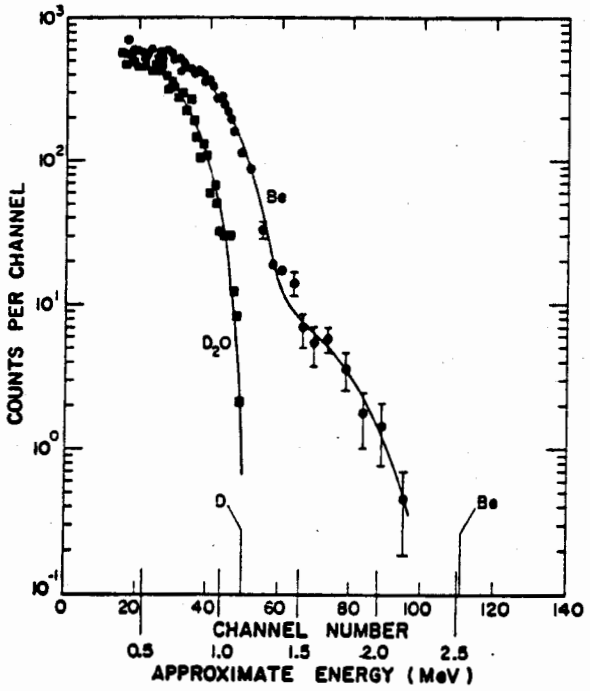

Fig. 46.
^{4}He neutron spectrometer data, 4.5-MeV bremsstrahlung-induced photoneutron pulse-height distribution for beryllium and D_2O.

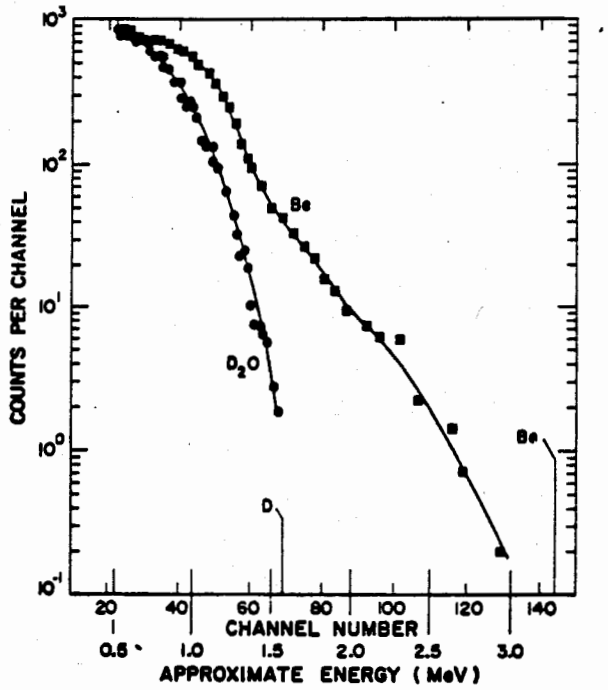

Fig. 47.
^{4}He neutron spectrometer data, 5.35-MeV bremsstrahlung-induced photoneutron pulse-height distribution for beryllium and D_2O.

pulse-height distributions are shown for both 4.5- and 5.35-MeV electron energies to illustrate the approximate range over which a successful discrimination can be made. As the electron energy is raised, all yields are correspondingly raised, with roughly a factor of two increase in yield per electron between 4.5 and 5.35 MeV for both deuterium and beryllium (Fig. 40). However, the ^{4}He detector efficiency falls off monotonically for neutrons $\geqslant 1.1$ MeV. This factor must also be considered in arriving at an optimum electron energy.

When higher energies are used, the photofission neutrons of ^{238}U, ^{235}U, and ^{239}Pu can be used for weapons detection. Figure 49 shows the ^4He spectrometer measurements of small sample ^{238}U photofission neutrons. Pulse-height distributions are shown for 6-, 7-, 10-, 12-, and 15-MeV electrons and are normalized to the same approximate bremsstrahlung dose incident on the sample at each electron energy. If the curves are multiplied by $(E_e)^3$ at each electron energy, they will be expressed approximately on a relative scale per electron.

The D(γ,n) distribution for 6- to 15-MeV electrons, also plotted for equal doses at each electron energy, is shown in Fig. 50. The systematic change of the spectral endpoint can be easily seen. Figure 51 shows a comparison of ^{238}U and Pb(γ,n) signatures at 10 MeV and

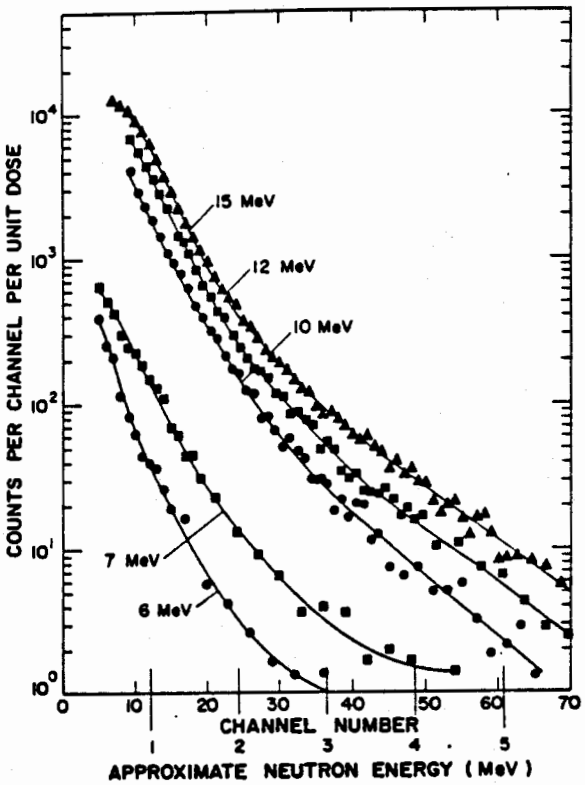

Fig. 49.

^4He neutron spectrometer data, ^{238}U photoneutron and photofission neutron pulse-height distribution for various bremsstrahlung energies.

illustrates a possible means of distinguishing between conventional and clean secondary designs.

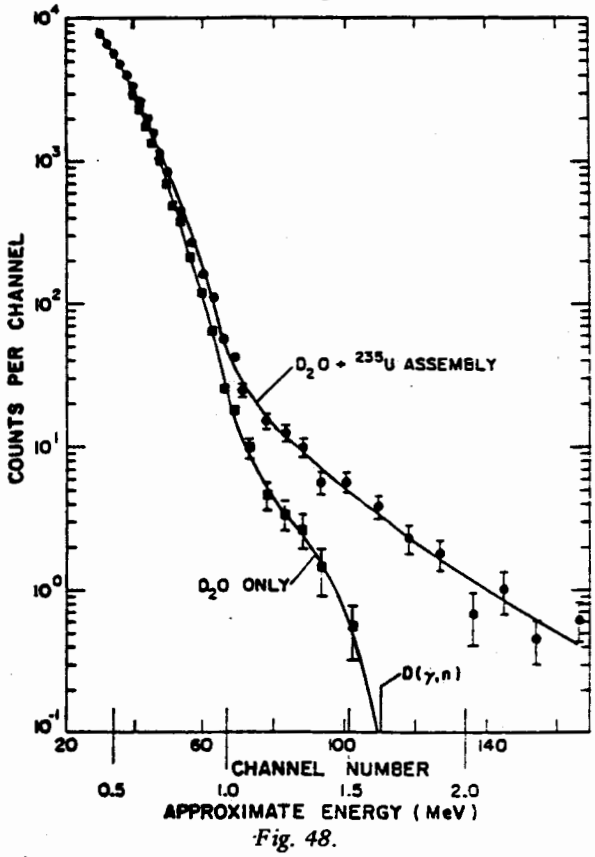

Fig. 48.

^4He neutron spectrometer data, 5.5-MeV bremsstrahlung-induced photoneutron pulse-height distribution for D_2O and for D_2O plus ^{235}U assembly.

UNCLASSIFIED

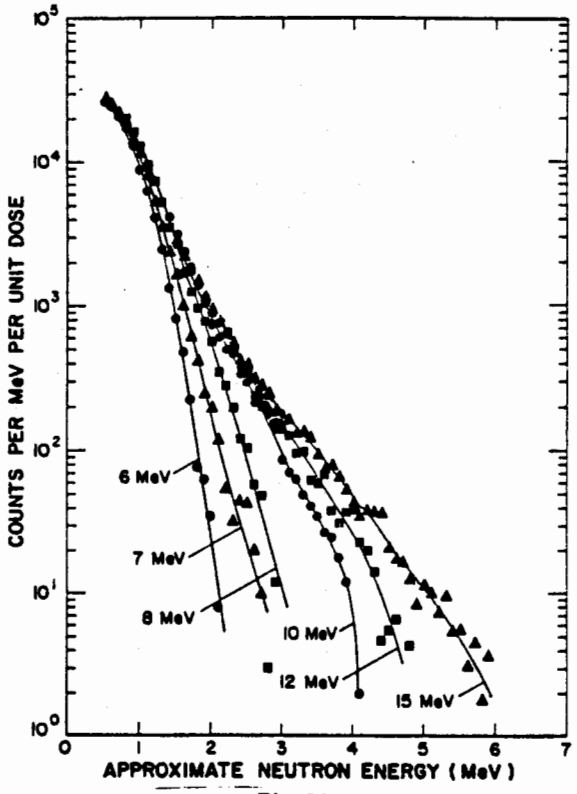

Fig. 50.
D(γ,n) ^{4}He proportional counter pulse-height distribution for 6- to 15-MeV bremsstrahlung.

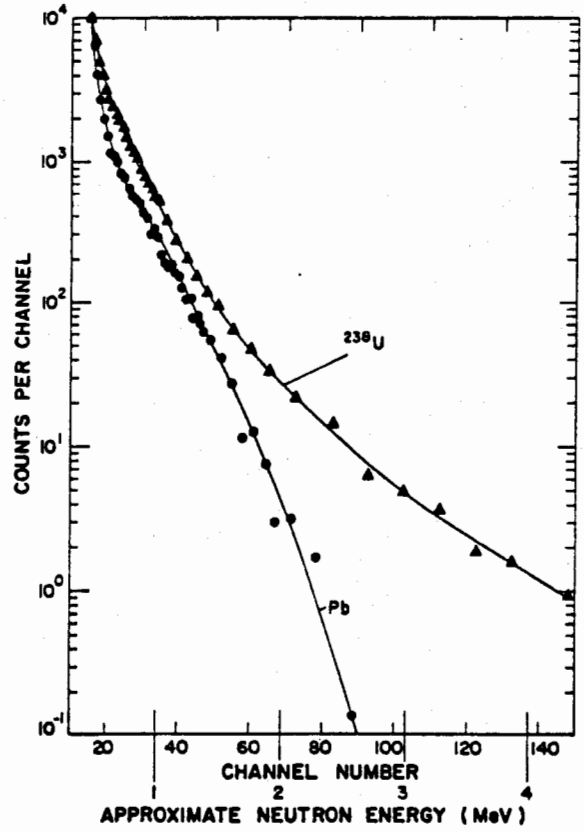

Fig. 51.
10-MeV bremsstrahlung-induced photoneutron pulse-height distribution for lead and ^{238}U.

b(2)
b(1)

[redacted]

one for larger quantities of beryllium.

d. Calculated and Scaled Results. To some extent the various results presented above can be summarized by scaling to the same systems described in Table XII for the radioisotope (γ,n) results. Anticipating the system definitions presented in detail in Sec. VI, two specific source and detector combinations are selected.

Table XV shows the number of counts obtained for various weapons using a Marx generator flash x-ray source at several energies and the slab detector described earlier. The Marx generator and the neutron detector are assumed to be 20 ft from the weapon. The net counts shown are for 40 pulses of 1.25×10^{14} electrons each (each pulse is thus equivalent to 100 A for 0.2 μsec). These calculated values are based on small sample measurements, radioactive source (γ,n) measurements, and the attenuation and multiplication calculations mentioned above. The expected count from beryllium in small RV quantities is also shown. For beryllium in this quantity or less, a few pulses at 2.2 MeV would suffice to determine beryllium effects to ± 20%. However, this technique is not a good

Because Marx generator measurements would be pulsed, the effects of space backgrounds would be small. Assuming the backgrounds previously discussed and a 50-μsec counting time per pulse, the total background count from all sources during the 40-pulse irradiation (Table XV) would be less than one count.

Table XVI shows bremsstrahlung-induced count rates expected for a photointerrogation system using a 500-W, 5-MeV electron linac. This beam is incident on a thick (≈ 0.10 cm) tungsten bremsstrahlung target assumed to be 10 ft from the interrogated weapon. The linac is farther away with the bremsstrahlung target suspended on a lightweight boom. The detector is assumed to be a bank of 10 16-atm ^{4}He proportional counters (2 in. diam, 24 in. long) located 20 ft from the interrogated weapon.

The entries in Table XVI were obtained by scaling measured D(γ,n) ^{4}He spectrometer count rates from the EPA small sample measurements to the ^{6}LiD mass distribution appropriate to each weapon. Complicating effects such as bremsstrahlung attenuation in intervening high-Z

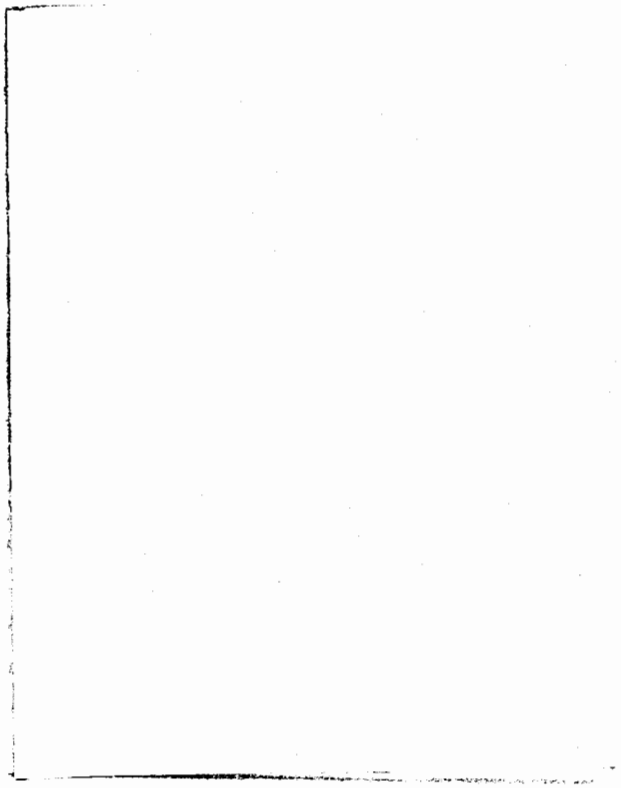

Fig. 52.
Linac interrogation of the Mk-53 for electron energies of 6 to 12 MeV.

materials and ^{235}U (n,f) reaction components were taken into account using the techniques described in Ref. 9. The resulting output spectrum (analyzed approximately into separate D(γ,n) and ^{235}U (n,f) components) was then folded into the ^{4}He detector response, and the final spectrometer response was summed over the indicated limits to illustrate approximate statistical accuracies for various pulse-height ranges. The beryllium-only entry was calculated in a similar fashion assuming that 2.5×10^{3} cm^2 of beryllium, 0.07 cm thick, is on the exterior portion of the target weapon.

The effect of space background on these measurements is negligible, primarily because the linac is pulsed, and the indicated 100-sec interrogation corresponds to a detector on-time of about 0.5 sec. Using the space neutron background estimates already discussed, about 4 to 40 total counts can be expected, distributed over the entire pulse-height range 0 to $>$ 10 MeV. This background could probably be neglected entirely; however, an *in situ* background measurement between beam bursts could easily be made.

Electronics for the ^{4}He spectrometer are identical to those discussed earlier for the ^{3}He slab detector with the exception that a pulse-height analyzer is also required. Only a modest number of channels of pulse-height data are required ($\sim$ 100), and the pulse-height analyzer discussed in connection with the passive gamma detector is more than adequate for this purpose.

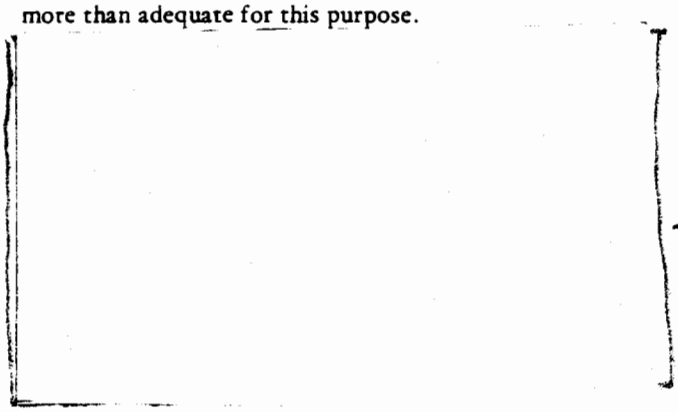

The spectra of Fig. 52 can be converted to the conditions of Table XVI by simple scaling

TABLE XV

APPROXIMATE SLAB DETECTOR COUNT RATES FOR 40 PULSES OF A MARX GENERATOR WITH 100-A, 0.2-μsec PULSES

Weapon	4-MeV Electrons (Net Counts)	5-MeV Electrons (Net Counts)	2.2-MeV Electrons (Net Counts)
	474	1452	—
	454	1390	—
	1140	3490	—
	282	866	—
	494	1514	—
	918	2812	—
	474	1058	50

TABLE XVI

APPROXIMATE COUNTS OBTAINED WITH A 100-SEC, 5-MeV LINAC INTERROGATION OF SELECTED WEAPONS SYSTEMS

Weapon System	Counts ⩾ 0.5-MeV Pulse Height	Counts ⩾ 1.0-MeV Pulse Height	Counts ⩾ 1.39-MeV Pulse Height [D(γ,n) Endpoint]	Counts ⩾ 2.96-MeV Pulse Height [Be(γ,n) Endpoint]
	5000	1970	960	120
	7300	1000	35	4
	4800	1890	920	110
	1800	250	9	1
	5880	800	28	3
	1000	260	70	—

Experiments to compare relative 14-MeV neutron and 10-MeV electron bremsstrahlung-induced fission efficiencies were performed on a Mk-53 at Pantex in a standard geometry using the same neutron detector.

4. Delayed Fission Neutron Time History. Delayed neutrons are a unique signature for fissionable isotopes at 10 MeV because there are no other photoreactions on any isotope that can generate directly a delayed neutron. In addition, under favorable conditions the delayed neutron time history from photofission can be used to determine a rough $^{235}U/^{238}U$ isotope ratio.

Figure 53 shows a delayed neutron time history for the Mk-53 system following 10-MeV bremsstrahlung-induced photofission.

Figure 54 shows the delayed neutron time history for a 7-MeV bremsstrahlung irradiation of the XW-67 secondary. This measurement was done at the SCAPP at LASL, and the data shown are the sums produced by 10 0.2-μsec pulses spaced 30 sec apart. Again, a slab detector was used. The solid line through the data points is the calculated time history using published ^{235}U (n,f) delayed neutron time history parameters.[22] The dashed line is the calculated time history using published small sample ^{235}U

Fig. 53.
Mk-53, 10-MeV bremsstrahlung-induced delayed neutron time history.

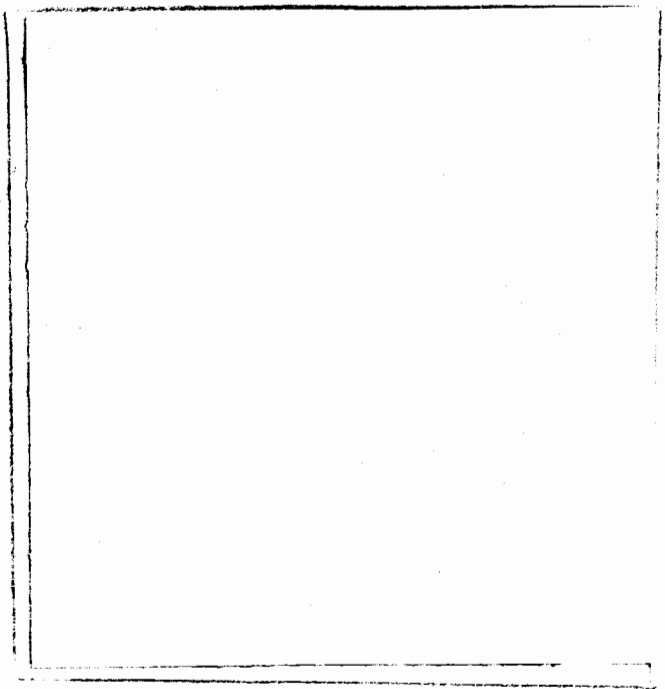

Fig. 54.
XW-67 secondary, 7-MeV bremsstrahlung-induced delayed neutron time history.

(γ,f) delayed neutron time-history parameters.[21] An independent measurement done at SCAPP using a small ^{235}U sample verified the values in Ref. 21. Figure 54 demonstrates that even with 7-MeV bremsstrahlung, the time history

Similar time histories were taken for the XW-67 at 4, 5, and 6 MeV, and all displayed the shape shown in Fig. 54.

The delayed neutron measurements of the Mk-53, XW-67, and small samples of ^{238}U and ^{235}U lead one to expect at least two distinct delayed neutron time histories from weapons following interrogation in the 4- to 10-MeV bremsstrahlung energy range.

There is a factor of 1.8 difference in an early-to-late ratio (count rate at ~0.5 sec compared to count rate at ~ 20 sec) between these two delayed neutron time histories for identical short burst irradiations. However, it is not likely that conditions of a typical space inspection mission will be sufficiently stable to exploit this difference.

The 10-MeV Mk-53 delayed neutron experiment, when scaled to a 1-sec irradiation of 5×10^{-4} A of 10-MeV electrons incident on a bremsstrahlung target 10 ft away with the slab detector 20 ft from the Mk-53, results in a delayed neutron count rate

Because the space background can be measured in some cases, a time history of sorts can apparently be measured for large weapons at 10 MeV.

5. Time-of-Flight Spectrometry. If an inspection could be carried out at distances of $\gtrsim$100 ft under stable ranging conditions ($\Delta R/R \leq 0.05$) with short beam bursts (≤ 0.1 μsec), then a time-of-flight technique could be attempted.

E. Neutron Interrogation. Experiments and calculations were done to investigate the feasibility and usefulness of active 14-MeV neutron interrogation in the satellite inspection problem. Selected neutron sources and assemblies were used to measure prompt decay constants, integrated prompt responses, and delayed neutron yeields.

1. Experimental Results. Measurements were made at Pantex on the Mk-53 and the W-68 using a Sandia prototype, high-output neutron generator. The weapons were pulsed once every 300 sec for a total of three pulses of approximately 10^{10} neutrons (14 MeV) per pulse to provide both delayed neutron kinetic response and delayed neutron yield data.

The detector consisted of a slab of polyethylene 3 by 20 by 24 in. with 19 1-in. diam ^{3}He proportional counters. This particular detector was designed for laboratory use but does permit extrapolation to a suitable detector for use in space. Pulses from the detector were fed through an appropriate preamplifier, amplifier, and discriminator. The resultant logic pulses were then fed

into a multichannel analyzer operating in the multiscale mode. A crystal-controlled external timer was used to provide varying channel widths of 0.5, 1.0, and 25 sec.

TABLE XVIII

EXTRAPOLATED PANTEX DATA FOR A SOURCE OF 10 PULSES PER SECOND OF 5 by 10^9 NEUTRONS PER PULSE

System	Count Rate (counts/sec)

TABLE XVII

PANTEX DELAYED NEUTRON YIELD DATA USING SANDIA PROTOTYPE HIGH-OUTPUT NEUTRON GENERATOR

Weapon System	Distance to Center of Weapon (in.)		Interrogation Location	Net Count Rate (from t = 0 to 0.5 sec)
	Source	Detector		

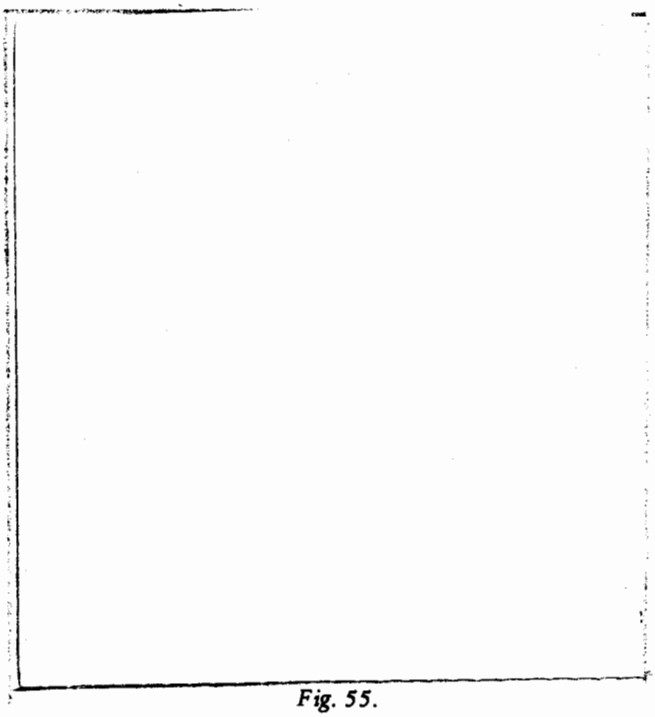

Fig. 55.
Mk-53 delayed neutron decay following 14-MeV neutron interrogation. Sandia high-output neutron generator.

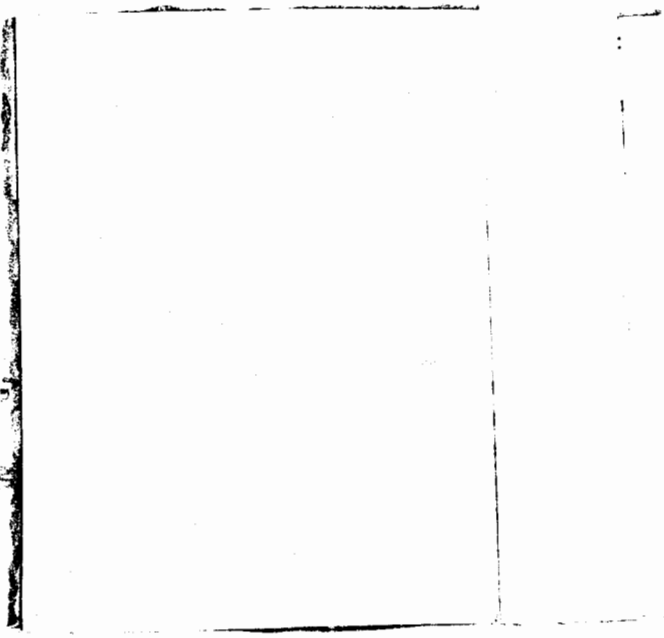

2. Calculated Decay Constants and Multiplication Factors. The decay constant, α, and the effective neutron multiplication factor, k_{eff}, were calculated for all weapon primaries listed in Table XIX. These calculations were made with the LASL DTF-IV neutron transport program[23,24] in spherical geometry. The S_8 discrete ordinates approximation was used with 16 energy groups and isotropic scattering. Cross-section values from the current LASL 16-group Hansen[25] set were used.

Calculation of k_{eff} for each of the subcritical primaries is straightforward and involves no unusual computational problems. Calculation of the decay constant, α, involves the basic physical assumption that the time behavior of the spatial and energy dependent neutron density, $n(\bar{r},\bar{\Omega},v,t)$, can be described by a fundamental decay constant, α, such that

$$n(\bar{r},v,\bar{\Omega},t) = n(\bar{r},v,\bar{\Omega})\exp(\alpha t) \quad , \tag{1}$$

where $\alpha < 0$ for the subcritical systems considered here. The assumption of a dominant fundamental decay constant implies that higher order spatial modes and kinetic distortion of the neutron density will decay much faster than the fundamental mode and therefore will not contribute to the measured decay rates.

The method of computing decay constants will be discussed briefly. Using standard notation, the neutron transport equation is written as

$$\frac{\partial}{\partial t}n(\bar{r},v,\bar{\Omega},t) + \Sigma_t(v)\phi(\bar{r},v,\bar{\Omega},t) + \bar{\Omega}\cdot\nabla\phi(\bar{r},v,\bar{\Omega},t)$$
$$= S(\bar{r},v,\bar{\Omega},t) + \int_{v'}\phi(\bar{r},v',\bar{\Omega}',t)$$
$$\Sigma_s(v')f(v,\bar{\Omega};v',\bar{\Omega}')dv'\,d\bar{\Omega}' \quad . \tag{2}$$

The transport equation is reduced by the method of discrete ordinates[24] to a set of coupled multigroup difference equations. These equations are ordinarily solved numerically for the eigenvalue, k_{eff}, which is contained in the source term $S(\bar{r},v,\bar{\Omega},t)$. To calculate the decay constant, α, Eq. (1) is substituted in the first term of Eq. (2), resulting in

$$\frac{\partial}{\partial t}n(\bar{r},v,\bar{\Omega},t) = \frac{\alpha}{v}\phi(\bar{r},v,\bar{\Omega},t)\exp(\alpha t) \quad . \tag{3}$$

Because the time dependence $\exp(\alpha t)$ is a multiplier in each term of Eq. (2), the transport equation reduces to the steady state expression

$$\left(\frac{\alpha}{v} + \Sigma_t(v)\right)\phi(\bar{r},v,\bar{\Omega}) + \bar{\Omega}\cdot\nabla\phi(\bar{r},v,\bar{\Omega}) = S(\bar{r},v,\bar{\Omega})$$
$$+\int_{v'}\phi(\bar{r},v',\bar{\Omega}')\,\Sigma_s(v')f(v,\bar{\Omega};v',\bar{\Omega}')\,dv'\,d\bar{\Omega}' \quad . \tag{4}$$

Equation (4) can now be reduced by discrete ordinates techniques and solved numerically with α treated as the

TABLE XIX

MEASURED AND CALCULATED DECAY CONSTANTS AND EFFECTIVE MULTIPLICATION FACTORS

System	1/8-in. Lead-Covered 2- by 2-in. NE-213 with Pulse Shape Discrimination to Eliminate Gamma Rays (see [illegible])	1/2-in. Polyethylene-Shielded 2- by 2-in. NE-213 Detecting Gamma Rays and Neutrons (see [illegible])	^{3}He Detectors (see [illegible])	Calculated Value Using 1-Dimensional DTF-IV (see [illegible])	Effective Multiplication Factor, k_{eff}, Calculated Using DTF-IV
[illegible]					

eigenvalue.

These instabilities are reasonably well understood and can be overcome by repeatedly adjusting convergence rate control parameters. Calculated decay constants in Table XIX are definitely converged values and should contain numerical uncertainties no larger than a few percent. Agreement between calculated and measured α values is generally good and indicates that the techniques used to measure decay constants are accurate and consistent.

Calculations indicate that it will be very difficult or impossible to measure both the prompt fundamental mode and the prompt-to-delayed ratio

3. Neutron Source. Sandia Laboratories (Albuquerque) are developing a high-output, 14-MeV neutron generator to produce the order of 10^9 n/μsec in pulses with widths of 5 to 30 μsec. Presently they have attained 3×10^8 n/μsec with generator lifetimes of greater than 400 pulses. The high voltage and ion source are on only during the pulse, because a pulse transformer is used to generate the source and acceleration voltage. Thus, the background between pulses is only the result of activation of ^{17}O in the tube insulators, and these background levels are very low. For the application in this study, i.e., the measurement of prompt responses of weapons, the 5-μsec pulse would be used.

TABLE XX

ESTIMATED INTEGRATED COUNT AND THE ASSOCIATED EARLY AVERAGE COUNT RATE

System	$\int_{20\ \mu sec}^{-} Cdt$	$\frac{\int_{20\ \mu sec}^{T_{1/2}+20\ \mu sec} Cdt}{T_{1/2}}$

The neutron generator and pulse transformer can be packaged in a cylinder about 15 in. long and 7 in. in diam and weighing about 15 lb. The power required is approximately 200 mA at 4 kV for the duration of each 20-sec active interrogation. In addition, a few watts (less than 50) would be required during the active interrogation and the background determinations.

The detectors chosen were a cluster of five proton recoil detectors with minimal shielding and the small slab detector as described in the (γ,n) technique. The inspection distances are not great enough to cause distortion of the time spectra for neutrons above 0.5 MeV from differences in time-of-flight. No gamma-ray discrimination is used because it is difficult to operate at the high count rates, and a higher efficiency is obtained by counting both neutrons and gamma rays. The suitability of this mode of operation can be seen by observing the agreement for the decay constants given as shown in Table XVIII. The proton recoil detectors were chosen over ^4He or CH_2 proportional counters because of the increased efficiency attainable. The small slab detector used in the (γ,n) technique will be used here for the detection of delayed neutrons.

The devices in Table XX give a representative sampling of the various types of weapons that might be encountered and thus represent reasonable limits on count rates. If a system

the detected count rate will be reduced considerably. The same is true for

In this case the systems may not be detectable with this method.

F. Delayed Gamma Rays. An inspection system which has a pulsed neutron or photon source on board, as well as a Ge(Li) detector, can obtain additional information by analyzing the gamma-ray spectrum between interrogating pulses. There are several potential sources for the gamma rays emitted following an incident pulse of photons or neutrons.

Delayed fission gamma rays are emitted by fission products which are left in high angular momentum states after fission. Lifetimes are long ($\sim 10^{-3}$ sec) because transitions from these high angular momentum states are highly inhibited. For a weapon system, experiments indicate that these delayed fission gamma rays are extremely weak relative to gamma rays from the other sources to be discussed.

Isomeric states in nonfissionable materials can be excited via (γ,n), (n,2n), and possibly (n,n′) reactions. Over the periodic table, the lifetimes of these states vary

for a 3-in.-thick mock HE shell with an incident pulse of $\sim 10^5$ fast neutrons, the thermal neutron flux in the shell was $\sim 10^4$ neutrons/cm^2/sec and had a half-life of ~ 1 msec. This flux estimate is based on measurements of the 2.224-MeV gamma ray from the H(n,γ)D reaction in the shell. During this thermalization and die-away, (n,γ) and (n,f) reactions can take place. The neutron capture will produce characteristic gamma rays observable with a Ge(Li) detector. These gamma rays will have energy, relative intensity, and half-life (which will follow the neutron half-life) signatures which should enable identification of the elements in the hydrogenous material. For example, in fast neutron interrogation of the mockup systems gamma rays from H(n,γ), Cl(n,γ), and N(n,γ) were clearly identified. Direct evidence for fissionable materials was not found except that in some cases prompt fission neutrons caused Ge(n,n'γ) reactions in the Ge(Li) detector. At 690 keV there is a peak which has a very characteristic shape.

The (n,n') and (n,2n) reactions, which will occur during the neutron burst, can produce nuclei in isomeric states. The characteristic gamma rays from isomeric states in ^{206}Pb and ^{207}Pb have been observed.

from $< 10^{-9}$ sec to tens of minutes. Many of these isomers emit gamma rays with characteristic energies, relative intensities, and half-lives. For example, the (γ,n) or (n,2n) reaction on ^{209}Bi can lead to an isomeric state in ^{208}Bi which has a 2.5-msec half-life. This state emits 0.925-, 0.654-, and 0.510-MeV gamma rays with a strong relative intensity and some other gamma rays weakly. The same reactions on natural lead yield isomeric states in ^{206}Pb($T_{1/2}$ = 0.13 msec) and ^{207}Pb($T_{1/2}$ = 0.8 sec), each of which emits several gamma rays.

A quick survey of the chart of the nuclides indicates that there are 45 nuclei with isomeric levels which have half-lives between 10^{-5} and 10 sec, and which can be reached by (γ,n) and (n,2n) reactions on naturally-occurring isotopes. Similarly, there are 45 nuclei which have isomeric levels in the same half-life region, and which may possibly be excited by inelastic neutron scattering.

If an interrogation is made with neutrons and there is a substantial amount of hydrogenous material present, then another process will occur. There will be considerable neutron thermalization in the hydrogenous material over a period of time like 10^{-6} to 10^{-3} sec. For example,

VI. System Definition

A. Approach to System Definition. Based on the techniques described in the previous sections of this

TABLE XXI

ISOMER COUNT RATE AT 15 MeV

Isomers	E_γ (MeV)	Photopeak Counts
^{207}Pb	1.066	10^3
	0.572	2×10^3
^{208}Pb	0.925	2×10^2
	0.510	3×10^2

report, several sensor package concepts have been chosen as reasonable candidates for a spaceborne satellite inspector. These represent somewhat arbitrary but representative steps in the continuum of options that develop around the possible variations in weapon design, background conditions, countermeasures, and detection confidence.

The following assumptions about the overall inspection system influenced the conceptual design of the basic nuclear sensor packages:

b(1)

TABLE XXII

SUMMARY OF SENSOR PACKAGES

UNCLASSIFIED

TABLE XXIII

UNCLASSIFIED

UNCLASSIFIED

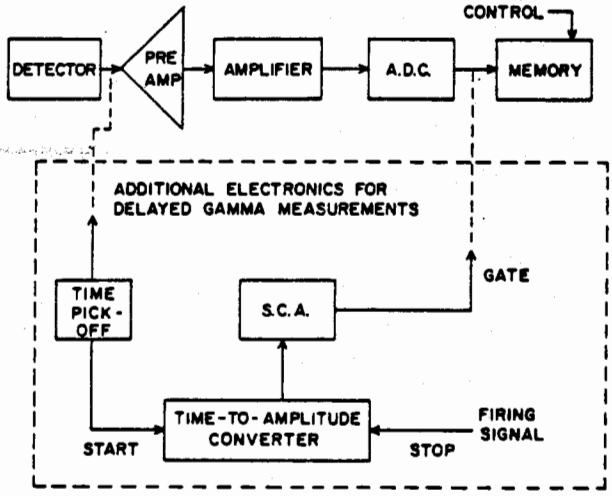

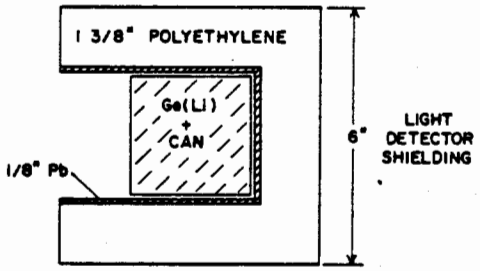

Fig. 58.
Schematic of gamma spectrometer.

b 3)

b(1)

TABLE XXV

DESCRIPTION OF IMAGING SUBSYSTEM

b(1)

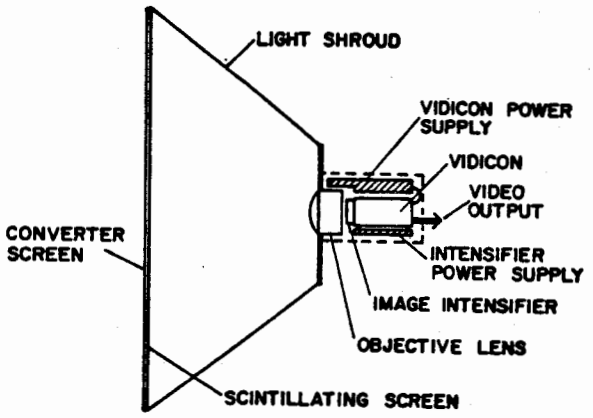

Fig. 59.
Schematic of radiographic imaging unit.

b(3)

UNCLASSIFIED

b

UNCLASSIFIED

TABLE XXVI

DETECTION CAPABILITY OF RADIOGRAPHIC SENSORS

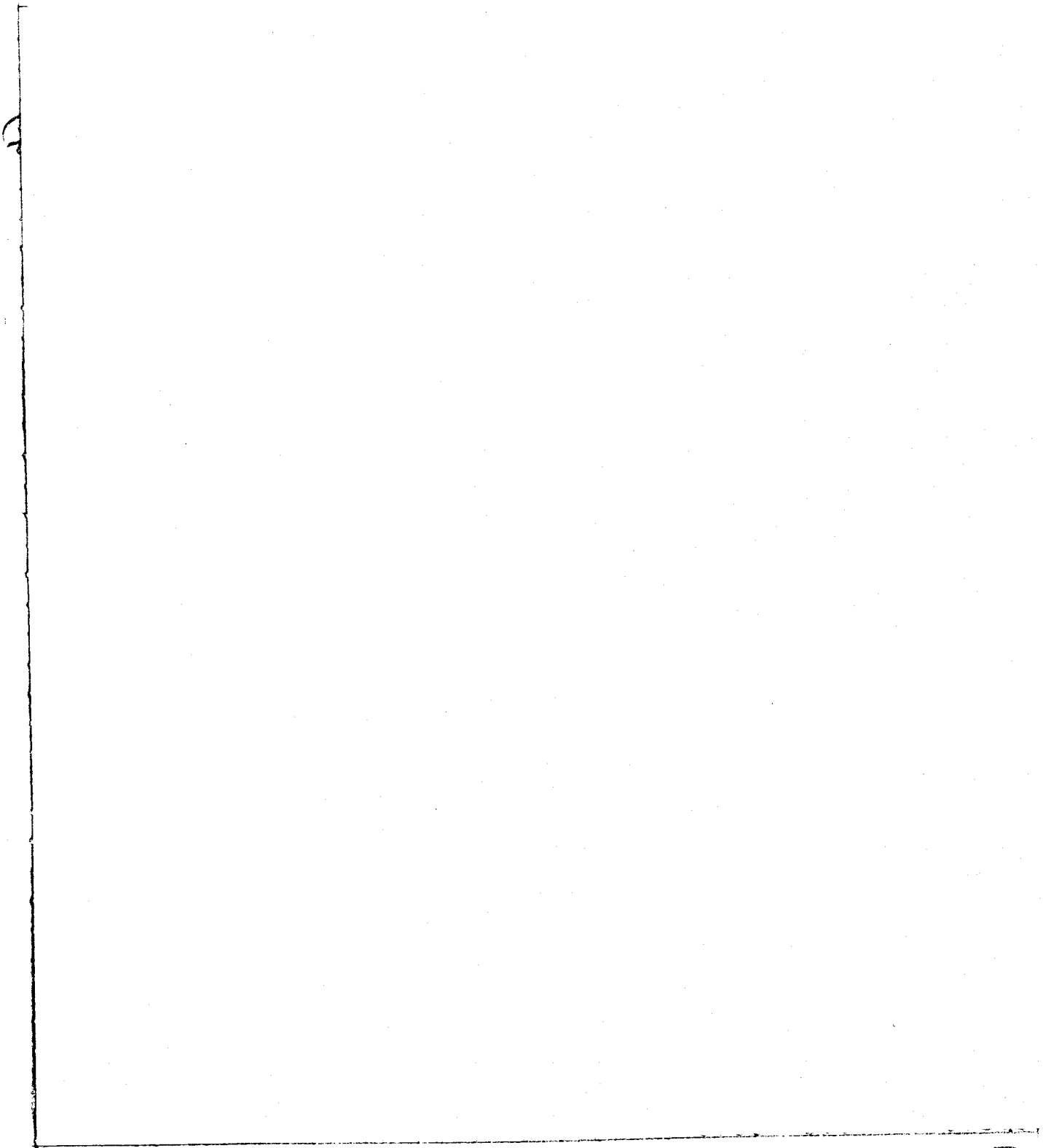

b(1)

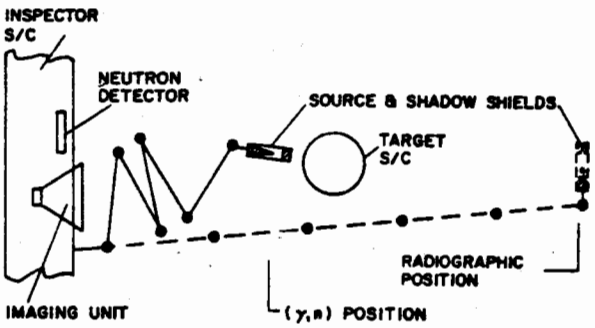

Fig. 60.
Source-target-detector geometry for radiographic and (γ,n) techniques.

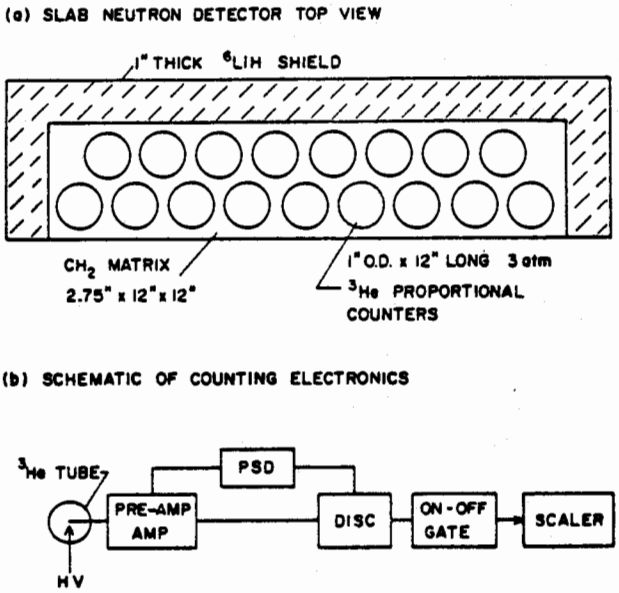

Fig. 61.
Slab neutron detector and a schematic of counting electronics.

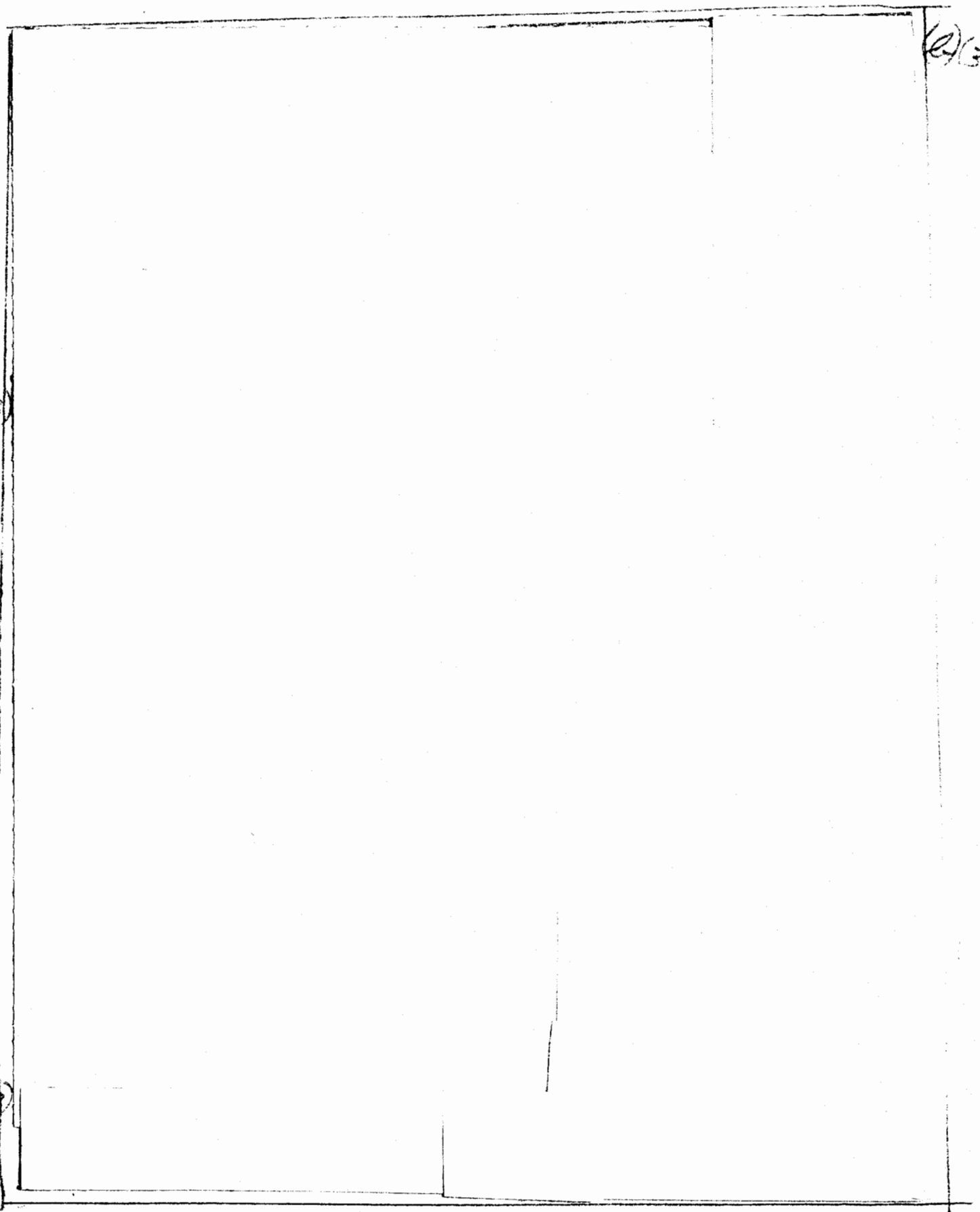

TABLE XXVII

WEIGHT (ESTIMATED) SUMMARY OF PROPOSED SENSOR PACKAGES

b(1)

TABLE XXVIII

DATA HANDLING SUMMARY

	Information Content Per Record (bits)	Maximum Transmission Rate to DHS (bps)
Radiographic sensor (vidicon)[a]	8.25×10^5	24.75×10^6
Gamma-ray spectrometer	1.60×10^5	8×10^4
^{3}He neutron detector	1.7×10^2	1.7×10^2
^{4}He neutron detector	1.9×10^3	9.5×10^2
Proton recoil detector	5.2×10^3	3.6×10^3

[a] All use common storage.

b(3)

b(1)

(b)(3)

(b)(3)

(b)(1)

(b)(1)

(b)(3)

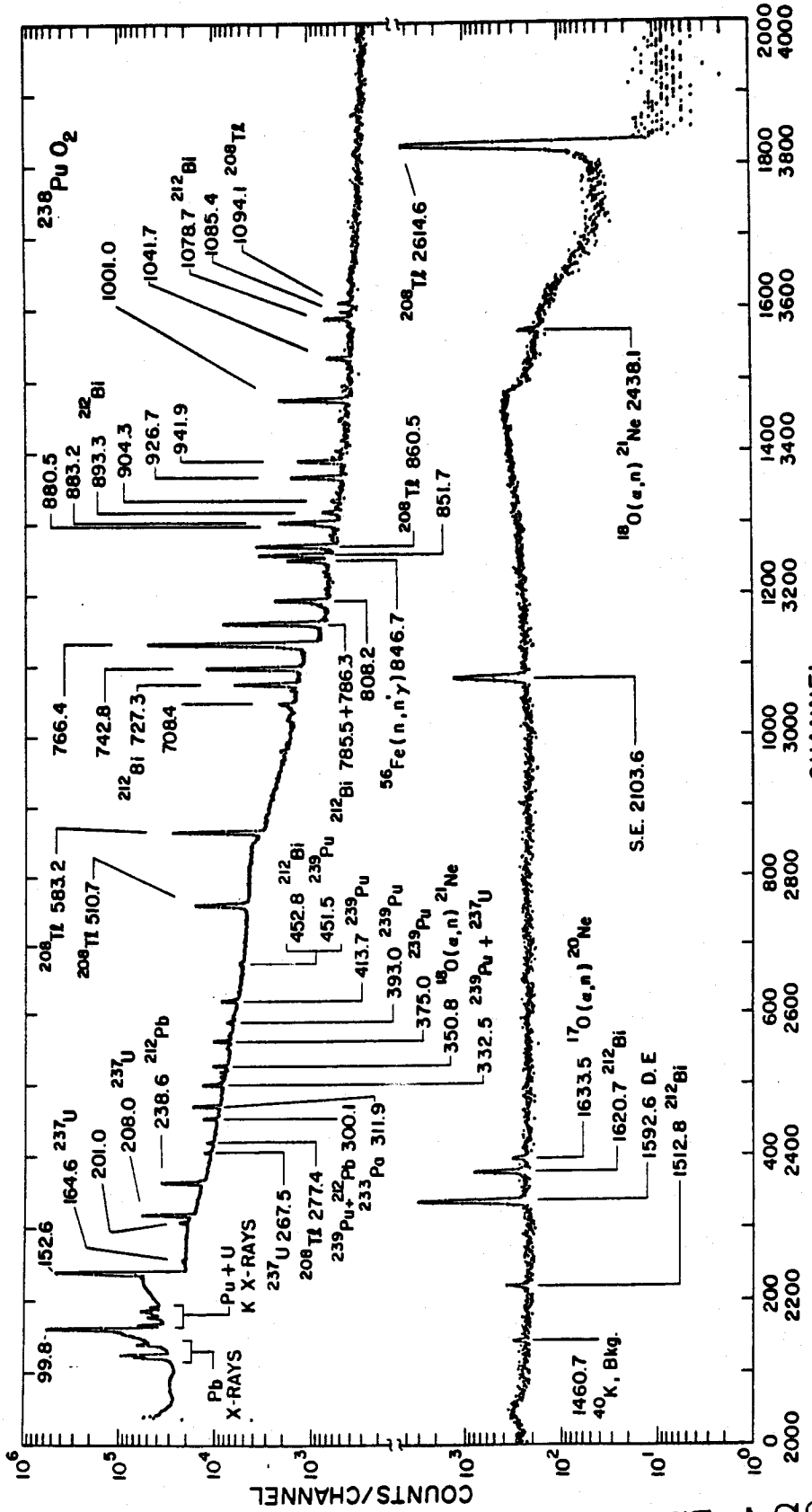

Fig. 62.
Gamma spectrum of $^{238}PuO_2$.

b(1)

b(1)

REFERENCES

1. Aerospace Corp. and SAMSO/AFSC, "Task 11 Final Report (U)," TOR-0172(2510-02)-1 (SRD) (July 27, 1971).

2. Grumman Aerospace Corp., "Task 11 Mission Analysis Final Summary Report (U)," (SRD) (February 1971).

3. North American Rockwell Corp., "Task 11 Mission Analysis Final Summary Report (U)," (SRD) (February 1971).

4. W. H. Chambers, "Weapon Characteristics for Neutron Detection and Identification," Los Alamos Scientific Laboratory report LA-4355-MS (January 1970).

5. G. R. Keepin, ed., "Nuclear Safeguards Research and Development, Program Status Report, January-April, 1970," Los Alamos Scientific Laboratory report LA-4457-MS (June 1970).

6. G. R. Keepin, ed., "Nuclear Safeguards Research and Development, Program Status Report, July-September 1969," Los Alamos Scientific Laboratory report LA-4315-MS (November 1969).

7. J. E. Cline, "Level Structure of ^{235}U Observed by a Study of the Alpha Decay of ^{239}Pu," Nucl. Phys. A106, 481-496 (1968).

8. G. R. Keepin, ed., "Nuclear Safeguards Research and Development, Program Status Report, May-August 1970," Los Alamos Scientific Laboratory report LA-4523-MS (September 1970).

9. W. H. Chambers et al., "MRV Verification by On-Site Inspection (U)," Los Alamos Scientific Laboratory report LA-4577 (SRD) (November 1970).

10. L. A. Currie, "Limits for Qualitative Detection and Quantitative Determination. Application to Radiochemistry," Anal. Chem. 40, 586-593 (1968).

11. J. T. Routti and S. G. Prussin, "Photopeak Method for the Computer Analysis of Gamma-Ray Spectra from Semiconductor Detectors," Nuc. Instr. Meth. 72, 125-142 (1969).

12. J. H. Head, "Minimum Detectable Photopeak Areas in Ge(Li) Spectra," Nuc. Instr. Meth. 98, 419-428 (1972).

13. L. V. East and R. B. Walton, "Polyethylene Moderated ^{3}He Neutron Detectors," Nuc. Instr. Meth. 72, 161-166 (1969).

14. G. R. Keepin, ed., "Nuclear Safeguards Research and Development, Program Status Report, October-December 1969," Los Alamos Scientific Laboratory report LA-4368-MS (February 1970).

15. Arms Control and Disarmament Agency, "Detection of the Presence of Nuclear Warheads (U)," FT-25 Final Report (SRD) (November 1971).

16. J. T. Caldwell, R. B. Walton, C. N. Henry, and J. J. Malanify, Los Alamos Scientific Laboratory internal document, April 16, 1970.

17. J. T. Caldwell, "Experimental Investigation of Particular Final-State Decay Modes Following Photo-Particle Reactions in O^{16}," Lawrence Livermore Laboratory report UCRL-50287 (May 23, 1967), p. 19.

18. G. R. Keepin, ed., "Pulsed Neutron Research for Nuclear Safeguards, Program Status Report, January-March 1968," Los Alamos Scientific Laboratory report LA-3921-MS (April 26, 1968).

19. J. S. Levinger, *Nuclear Photo-Disintegration* (Oxford University Press, London, 1960), 144p.

20. W. H. Buford, Jr., et al., "Nuclear Materials Detection Techniques, Vol. I (U)," Air Force Weapons Laboratory report AFWL-TR-67-66, Vol. I (SRD) (December 1967).

21. L. A. Kull, R. L. Bramblett, T. Gozani, and D. E. Rundquist, "Delayed Neutrons from Low Energy Photofission," Nuc. Sci. Eng. 39, 163-169 (1970).

22. G. R. Keepin, *Physics of Nuclear Kinetics* (Addison-Wesley, Reading, Mass., 1965), 435p.

23. K. D. Lathrop, "DTF-IV-A Fortran-IV Program for Solving the Multigroup Transport Equation with Anisotropic Scattering," Los Alamos Scientific Laboratory report LA-3373 (July 1965).

24. B. G. Carlson and K. D. Lathrop, "Transport Theory–The Method of Discrete Ordinates," Los Alamos Scientific Laboratory report LA-3251-MS (Revised) (October 1965).

25. L. D. Connolly, "Los Alamos Group-Average Cross Sections," Los Alamos Scientific Laboratory report LA-2941-MS (September 1963).

26. G. M. Simmons and C. P. Jupiter, "Nuclear Materials Detection Techniques, Vol. II: Nuclear Materials Discrimination Techniques (U)," Air Force Weapons Laboratory report AFWL-TR-67-66, Vol. II (SRD) (June 1968).

27. G. I. Bell, Los Alamos Scientific Laboratory internal document, November 11, 1969.

28. D. B. Eheoglu, "Radiographic Sensor. Final Report (U)," Air Force Weapons Laboratory report AFWL-TR-68-110 (SRD) (December 1968).

29. J. I. Vette, D. Gruber, J. L. Matteson, and L. E. Peterson, "A New Component of Cosmic Gamma Rays Near 1 MeV Observed by the ERS-18," Astrophys. J. 160, L161-L170 (1970).

30. R. W. Jenkins, J. A. Lockwood, S. O. Ifedili, and E. L. Chupp, "Latitude and Altitude Dependence of the Cosmic Ray Albedo Neutron Flux," J. Geophys. Res. 75, 4197-4204 (1970).

31. J. I. Vette et al, "Models of the Trapped Radiation Environment, Vols. 1-7," National Aeronautics and Space Administration report NASA-SP-3024, Vols. 1-7.

32. W. E. Dance, D. H. Rester, B. J. Farmer, and J. H. Johnson, "Bremsstrahlung Produced in Thick Aluminum and Iron Targets by 0.5 to 2.8 MeV Electrons," J. App. Phys. 39, 2881-2889 (1968).

33. L. C. Northcliffe and R. F. Schilling, Nuclear Data Tables A 7, 233 (1970).

34. G. L. Morgan and R. L. Walter, "Linearity and Energy Resolution of a High Pressure Helium Gas Scintillation Counter," Nuc. Instr. Meth. 58, 277-281 (1968).

35. G. L. Morgan and R. L. Walter, "Neutron-Helium Interaction. II. Angular Distributions and Phase Shifts from 0.2 to 7.0 MeV," Phys. Rev. 168, 1114-1130 (1968).

36. B. R. Hunt, D. H. Janney, and R. K. Ziegler, "Introduction to Restoration and Enhancement of Radiographic Images," Los Alamos Scientific Laboratory report LA-4305 (April 9, 1970).

37. R. Nathan, "Digital Video-Data Handling," Jet Propulsion Laboratory report JPL-TR-32-877 (January 5, 1966).

38. R. H. Selzer, "Digital Computer Processing of X-Ray Photographs," Jet Propulsion Laboratory report JPL-TR-32-1028 (November 15, 1966).

39. Harry C. Andrews, *Computer Techniques in Image Processing* (Academic Press, New York, 1970), 187p.

APPENDIX A

Ge(Li) DETECTOR CHARACTERISTICS

Very often a computed or measured count rate is quoted for a Ge(Li) detector whose only given specification is active volume, i.e., 50 cc, 80 cc, etc. With only this specification one cannot, in general, extrapolate the count rate accurately to other detectors or geometries. Additional data are needed concerning the exact dimensions, drift depth, and geometry because no two detectors have the same geometrical parameters.

The detector industry now standardizes the specification of Ge(Li) detectors by quoting efficiency relative to that of a 3- by 3-in. NaI detector at a source-detector distance of 25 cm and an energy of 1.33 MeV. The 1.33-MeV efficiency for a 3- by 3-in. NaI detector under these conditions is 1.2×10^{-3} photopeak counts per source disintegration, a calculated number. A somewhat different number would be measured from a ^{60}Co source due to summing effects. This convention is followed in subsequent discussion; thus the efficiency of a Ge(Li) detector expressed as a percent, i.e., 6%, 10%, etc., is relative to a 3- by 3-in. NaI detector at 25 cm and 1.33 MeV. This relative efficiency would be different if measured at other source energies or other distances because of geometrical and photon cross section differences between germanium and NaI. The largest Ge(Li) detectors now available off the shelf have relative efficiencies of about 20%.

The detector geometry is also important. For the purposes of this study a closed end coaxial geometry is preferred, because the entire frontal area is active. The ratio of active-to-dead volume should be as large as possible and is well over 95% for state-of-the-art detectors. The drift depth and length-to-diameter ratios are important for our application. Larger drift depths increase the peak-to-Compton ratio as well as the efficiency per unit volume. Drift depths approaching 20 mm are available at the present time.

The interplay of these factors is illustrated in Table A-I. Detector 1 is the 6% Ge(Li) detector used to record the spectra displayed previously. Detector 2 is a large volume state-of-the-art detector of the type proposed for this mission. The volume of detector 3 is even larger than that of detector 2 but detector 3 has a much poorer efficiency. The table vividly illustrates the pitfalls of specifying a detector only by volume. The superiority of detector 2 over detector 3 is due to greater drift depth and a larger diameter-to-length ratio. Because of its length, detector 3 might exhibit better performance for this application if used in side incidence.

Measured efficiency curves for detectors 1 and 2 are shown in Figs. A-1 and A-2. These efficiencies were measured for a source-detector distance of 1 m, the largest distance practical with the calibrated source intensities available. The large distance was used to approximate the nearly normal incidence of photons on the detector face that would be encountered in an inspection. The efficiencies for a 3- by 3-in. NaI detector shown in these figures

TABLE A-I

CHARACTERISTICS OF SEVERAL Ge(Li) DETECTORS

Detector No.	Active Volume (cm^3)	Diameter (mm)	Length (mm)	Drift Depth (mm)	25-cm, 1.33-MeV Relative Efficiency (%)	Inferred 25-cm, 1.33-MeV Intrinsic Photopeak Efficiency (%)
1	35	40.5	28.5	16.5	6	4.4
2	85	47.8	48.9	18.5	18.2	9.5
3	88	41	71	15	10.2	7.3

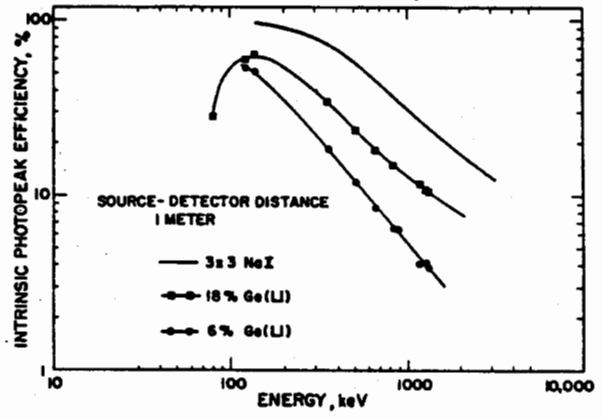

Fig. A-1.
Measured photopeak efficiency for gamma spectrometers.

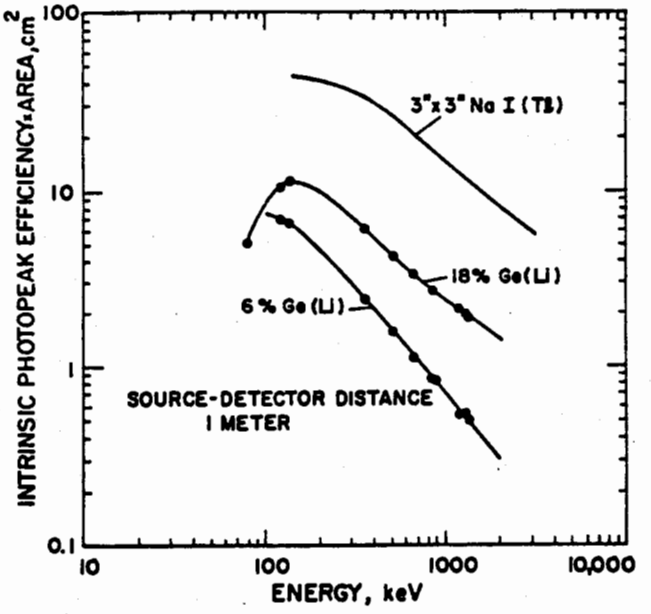

Fig. A-2.
Comparison of gamma spectrometers.

are calculated and measured values taken from Phillips Petroleum Co., Idaho Falls, report IDO-16880 (August 1964). In these figures intrinsic efficiency is defined as photopeak counts per gamma incident on the detector face. From the curves of Fig. A-2, which have the detector area folded in, count rates can be computed directly when the flux is given. Indeed, the data in Fig. A-2 were used to compute the flux from measured photopeak count rates, and also to predict count rates for a large detector when the flux is given.

APPENDIX B

THE RADIOGRAPHIC SYSTEM

I. Description

The basic radiographic system is a photofluorographic system using a scintillating screen coupled by an objective lens to an image intensifier. The image output of the intensifier is then recorded directly on Polaroid film through a fiber-optics coupling plate. A 3- by 3-ft scintillating screen was selected as being conveniently large for the radiographic targets of interest and sufficiently portable for transporting to a variety of radiation facilities. The screen composite is made up of 200 mg/cm^2 ZnCdS (US Radium PFG) covered by a sheet of lead 0.060 in. thick and a sheet of aluminum 0.060 in. thick. A lighttight bellows construction was selected to permit the use of a variety of lenses with different view angles. Most of the experimental work was done with only two lenses, although five lenses were evaluated and will be described later.

The image intensifier is a second generation proximity-focused intensifier which is very simple in design (although complex from the manufacturing point of view), very small and lightweight, and which requires relatively low supply voltages (about 6000 V) and very little power (about 6 mW). Two intensifiers were purchased from ITT for this program, one of 18-mm format and one of 23-mm format. The specifications for the tubes are given in Table B-I.

The 18-mm tube is of special interest because it can be coupled to a standard size vidicon target (also 18 mm). For imaging directly on film, the larger, 23-mm tube was more desirable. Second generation tubes as large as 75 mm have been produced, but such tubes are currently produced in small numbers with long delivery times.

These image intensifiers have a noise-induced output, with no light input, much like photomultipliers. Unlike photomultipliers however, there is no convenient way to discriminate against the noise. Therefore, when the image is being recorded directly on film, the noise-induced light is being integrated by the film in just the same way as the radiographic image. This noise then imposes a time limitation on the exposure time when isotopic sources are being used. It can be partially or totally eliminated by "gating" the tube on and off when using a pulsed source, providing the noise is produced in the photocathode.

A gating system was designed to switch the image intensifier rapidly, since the tube takes approximately 1 sec to turn on after full voltage is applied. The tube could effectively be switched much faster if the voltages across the microchannel plate (MCP) and between the MCP and phosphor were left on, and only the voltage between the photocathode and the MCP was switched. This was accomplished with a 200-V negative pulse which was varied in width from 0.5 to 82 μsec. In other experiments at LASL, a similar tube has been successfully gated for as short a time as 5 nsec. This gating capability allows the radiographic sensor to operate in high background orbits, since a direct-current background (which appears as light on the screen) can easily be overcome if the image intensifier is operated for only several microseconds in synchronization with a beam burst from a flash x-ray machine or linac.

TABLE B-I

IMAGE INTENSIFIER SPECIFICATIONS

	18-mm Tube	23-mm Tube
Maximum usable aperture	18 mm	23 mm
Maximum diameter	45 mm	50 mm
Thickness	22 mm	17 mm
Conductivity (amperes at minimum gain)	6.7×10^{-7}	1.6×10^{-6}
Phosphor	P-20	P-20
Photocathode	S-25	S-20
Resolution	24 line pairs/mm	20 line pairs/mm
Cathode sensitivity	232 μA/lm at 4.3×10^{-4} lm	293 μA/lm at 7.5×10^{-4} lm
Luminous gain	22,500	42,000
Equivalent background input	1.8×10^{-12} lm/cm^2	1.04×10^{-11} lm/cm^2

The present radiographic system does not use a mirror to reflect the image by 90°, and the image intensifier is therefore not shielded from the beam. The system was used in this manner throughout the entire experimental program without any apparent ill effects. In a flyable system the in-line camera has the distinct advantage of saving this extra shielding weight.

All permanent radiographic data records were in the form of Polaroid pictures taken by direct film contact with the output fiber optics of the image intensifier tube. Much of the work was done with Polaroid 3000 film, but slower, high-contrast films were also used. Pictures for reproduction were taken on Polaroid Type 55 positive/negative film. Switching from one film to another required, of course, compensations in radiation dose, tube gain, etc.

Comparisons of film sensitivity and vidicon sensitivity were made to provide some basis for relating the performance of the system with that of a flight system with video recording. Several references cite a nominal vidicon sensitivity of 0.1 fc illumination on the vidicon target. A 30-Hz video scan corresponds to an exposure-per-frame of 3.3×10^{-3} fc-sec or 3.55×10^{-2} metercandle-sec. Using data sheets from the Polaroid Corporation, it is found that the Type 57 film (3000 ASA) requires 3.98×10^{-4} metercandle-sec to produce a 25% contrast picture; and that the Type 55 positive/negative film (50 ASA) requires a 3.6×10^{-2} metercandle-sec for a 25% contrast picture. A 25% contrast picture is subjectively a good picture and was therefore chosen for the comparison. The above figures show that the 3000-speed film is about 100 times more sensitive than the nominal vidicon, and that the positive/negative film has about the same sensitivity as the nominal vidicon. An improvement in the vidicon gain by 100 is probably easily achievable in a flight system by slow scan or other techniques, so the sensitivity of the radiographic system with 3000-speed film is comparable to that of a flight system.

II. Lens Evaluation

Each of the different lenses to be evaluated presented a different image format and a different focal length. This latter dimension is critical in that the photocathode of the image intensifier is at high voltage and arcing can occur. The lens evaluation also provided observations of the behavior of a very wide-angle lens placed close to the screen. The five lenses in Table B-II were evaluated using ^{60}Co as the radiographic source.

The f/0.78 lens was used with only partial success because the back focal length was small enough to cause intermittent arcing from the image intensifier. From the data that were taken, however, it was approximately twice as fast as the f/0.95 lens. The 25-mm, f/0.95 lens was used normally with the 18-mm image intensifier, because the image size from this lens closely matched the size of the intensifier. Similarly, the 50-mm, f/0.95 lens was used normally with the 23-mm image intensifier. However, during the lens comparisons, all the lenses were used with the same tube. The two f/0.95 lenses appeared to perform comparably except for the difference in image size.

TABLE B-II

CHARACTERISTICS OF EVALUATED LENSES

Aperture	Focal Length (mm)	View Angle (deg)	Lens-to-Screen Distance	Make
f/0.78	25	30	6 ft	Canon
f/0.95	25	30	6 ft	Angenieux
f/0.95	50	30	6 ft	Canon
f/1.3	15	47	45 in.	Angenieux
f/1.8	5.9	94	18 in.	Angenieux

One concern with the wide-angle lenses is illustrated by the f/1.8, 94° case in which the lens was 18 in. from the center of the screen and 31 in. from the extreme edges. This means that the center of the screen should be contributing three times more light than the edges, and it was expected that the radiographs would have a bright area near the center. The effect, if present at all, was not apparent in any of the test radiographs made. In addition, any distortion due to the extreme close-up was not in evidence. These tests also indicated that the nominal f numbers of the lenses were apparently not affected by the severe geometries.

III. Screen Evaluation

Three screens were evaluated using a 600-mCi ^{60}Co source and exposure times of 30 sec. The screens were 0.010 in. and 0.020 in. ZnCdS (Radelin, PFG) and 0.020 in. $CaWO_4$ (Radelin STF-2), and several pictures were taken with each screen for equivalent exposure times. The 0.020-in. ZnCdS and 0.020-in. $CaWO_4$ screens had twice the light output of the 0.010-in. ZnCdS screen, and it was found that the 0.020-in. ZnCdS screen had an extraordinarily long persistence when exposed to daylight or to radiation. The other two screens did not appear to suffer from this persistence problem. The thicker screen (0.020 in.) was made of two thinner layers bonded together, a manufacturing technique which may have contributed to the high persistence.

$CaWO_4$ screens have some advantages over the ZnCdS screens. They are more sensitive to harder radiation, and the blue light output (4400 Å) is better mated to the S-20 and S-25 photocathodes of the image intensifiers, compared with the yellow-green (5500 Å) of ZnCdS. Also the light output as a function of temperature is quite different for the two screens. These phenomena favor the $CaWO_4$ screen for this application and will be discussed further.

The optimum thickness of converter material (either lead, tungsten, or tantalum) in front of the scintillating screen is a strong function of the characteristics of the source used. For example, 0.040-in. lead sheets are used routinely at the Pantex linac, whereas 0.010-in. lead sheets are used routinely at LASL's GMX-1 betatron. Thicker lead converters give fuzzier images, however thicker converters also give better shielding to the scintillating screen (or film) in the presence of extraneous backgrounds (room scatter, target scatter, and source-associated background).

Several thicknesses of lead, ranging from zero to 0.060 in., were used with $CaWO_4$ screens at the SCAPP at 4 and 7 MeV. The quality of the radiographs improved rapidly up to 0.040 in. and slowly thereafter. However, the image obtained using 0.010 in. of lead was quite acceptable, whereas the radiograph taken with no lead lacked contrast. Because the SCAPP was found to have a great deal of source-associated background, the thicker sheets of lead provided more shielding rather than acting as converters.

IV. Screen-Lens-Photocathode Matching

Optimization of an intensifier-type radioactive system requires careful matching of the screen output spectrum with the spectral transmission characteristics of the objective lens and with the spectral response characteristics of the intensifier photocathode. Because most of the radiographic experiments were done with a non-optimum combination, the relative response of other combinations of these components was calculated to give some indication of the performance increase to be expected. This information would certainly temper a judgment on such matters as optimum exposure levels or absolute system sensitivity for this type of radiographic system.

The basic calculation of the response of a given intensifier photocathode and a given objective lens when exposed to light of some given spectrum is

$$I = \int_{\lambda_1}^{\lambda_2} S(\lambda)T(\lambda)R(\lambda)d\lambda \quad ,$$

where I is the photocurrent emitted by the photocathode, $S(\lambda)$ is the power spectrum of the incident light before its incidence on the lens, $T(\lambda)$ is the spectral transmission of the lens, and $R(\lambda)$ is the spectral response or absolute sensitivity of the photocathode. The limits of integration are over the incident light spectrum. The absolute spectral radiant power being emitted from the scintillating screen is not well known, but this does not prevent calculation of relative system outputs because the spectral shapes of $CaWO_4$ and ZnCdS light emissions are well known.

Figure B-1 shows the spectral shapes of $CaWO_4$ and ZnCdS light emissions, as well as the variety of photocathode response functions selected for trial calculations. For all calculations a "typical" lens transmission function was used and is also shown in Fig. B-1. This lens transmission function is that published[28] for a Canon 50-mm, f/0.95 lens, and is representative of fast, medium focal length lenses. The photocathode response functions selected included the S-20, the 116 which favored PFG, the 111 which favored $CaWO_4$, and the 135 which was flat across the spectral band encompassing both $CaWO_4$ and ZnCdS. The number designations are RCA nomenclature.

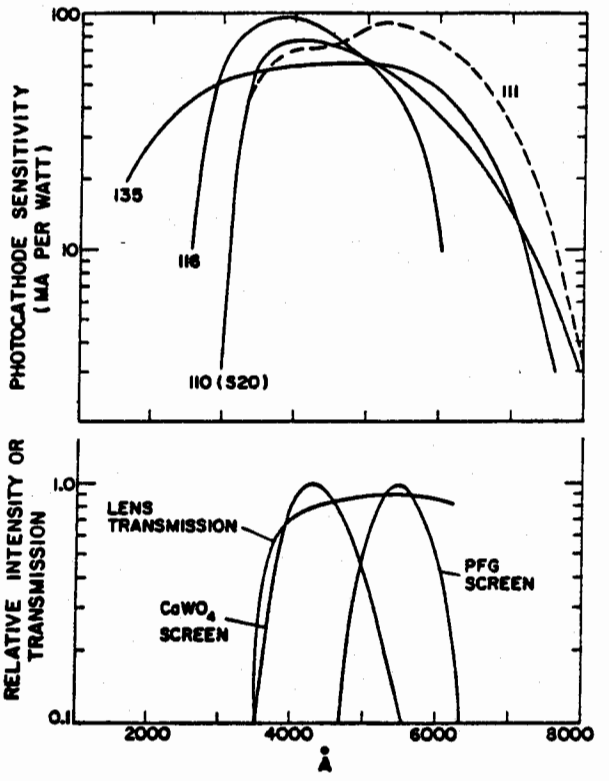

Fig. B-1.
Spectral functions of screens, lens, and photocathodes.

A simple computer program was written to integrate the product of a spectral function, the transmission function, and a photocathode response function. This calculation was done for all combinations of the functions shown in Fig. B-1, and the results of these calculations are shown in Table B-III. Note that with the same lens there is a range of about a factor of two in the photocathode output depending on the screen-photocathode matching. This particular lens favors the ZnCdS by removing about 20% of the $CaWO_4$ emission at the spectral peak.

For the present experiments note that for the same radiant power emission at the screen, $CaWO_4$ outperforms ZnCdS by a factor of 0.887/0.642 or 1.38 in terms of measured response, i.e., photomultiplier response, for instance. The relative light production efficiency in the two screens has not been considered here. However, the $CaWO_4$, because of its high average atomic number is a more efficient light producer than ZnCdS for the energetic photons of interest in this program; so considerations of relative light-producing efficiencies will tend to enhance further the performance capability of the $CaWO_4$ screen. The importance of this ratio is that a $CaWO_4$ screen with the same light output (watts per square centimeter, for instance) as a PFG screen would provide 38% more response in our image intensifier which happens to have the S-20 photocathode.

V. Cold Screen Experiments

Experiments were performed to investigate the behavior of $CaWO_4$ and ZnCdS scintillating screens over a range of temperatures. Information from several sources indicates that the light output from these screens may vary drastically with temperature, a phenomenon of special interest for space applications of the materials. In these experiments small samples of each screen material were cooled with liquid nitrogen while the screen was being irradiated with a ^{60}Co source and while the light output from the screen was being measured with a photomultiplier and electrometer. The dose rate delivered to the screen for all trials was about 85 R/h.

The design of the experimental geometry permitted (1) low thermal impedance between the screen material and the cryogen, (2) lighttightness to insure low optical backgrounds, and (3) insulation of the photomultiplier from the cold parts of the assembly. As the cryogen was introduced into a dewar containing the cold finger, both the output of the photomultiplier and the temperature of the cold plate were recorded. The initial temperature was either room temperature or as high as 50°C which was achieved by heating the screen-backing with a heat gun. When the temperature of the plate reached about −100°C, heat was again applied to the plate with the heat gun. Light output vs screen temperature was again recorded during the warm-up of the assembly. Careful control measurements using artificial light sources were made to insure that the photomultiplier response was not being affected by temperature excursions during the experimental trials. During such measurements the output of the photomultiplier was constant over the extremes of temperature.

The results of these experiments are shown in Fig. B-2. The light output from $CaWO_4$ increases with decreasing temperature, whereas the reverse is true for ZnCdS. The $CaWO_4$ was well-behaved in that the light output tended to follow the same curve as the temperature was lowered and raised. On the other hand, ZnCdS exhibited a peculiar hysteresis effect and the warming curve tended to jump to a new locus which was higher than the cooling curve. The behavior of the ZnCdS seemed to depend on recent thermal history; for instance, the initial light output at room temperature was maximum whenever the material had soaked at room temperature for many hours, but during subsequent temperature cycling this initial high output at room temperature was not achieved. It was also observed that the behavior of the material during each temperature cycle varied from the preceding cycle. Although the experiments were not continued long enough to establish it unequivocally, it appeared that after several temperature cycles the material was approaching a well-defined characteristic curve which was single-valued for each temperature. As a consequence of this anomalous behavior, the characteristics of ZnCdS are displayed in Fig. B-2 as a broad band instead of a curve.

To relate these two curves it should be noted that the experimental geometry, radiation source-screen spacing, was altered between trials to maintain the same signal output from the photomultiplier at room temperature,

TABLE B-III

CALCULATED SCREEN-PHOTOCATHODE RESPONSE

Photocathode	Relative Response	
	$CaWO_4$	ZnCdS
110 (S20)	0.887[a]	0.642[a]
111	0.946	1.000
116	0.992	0.482
135	0.752	0.663

(a) $\frac{(\text{Response})_{CaWO_4/S\text{-}20}}{(\text{Response})_{ZnCdS/S\text{-}20}} = 1.38$

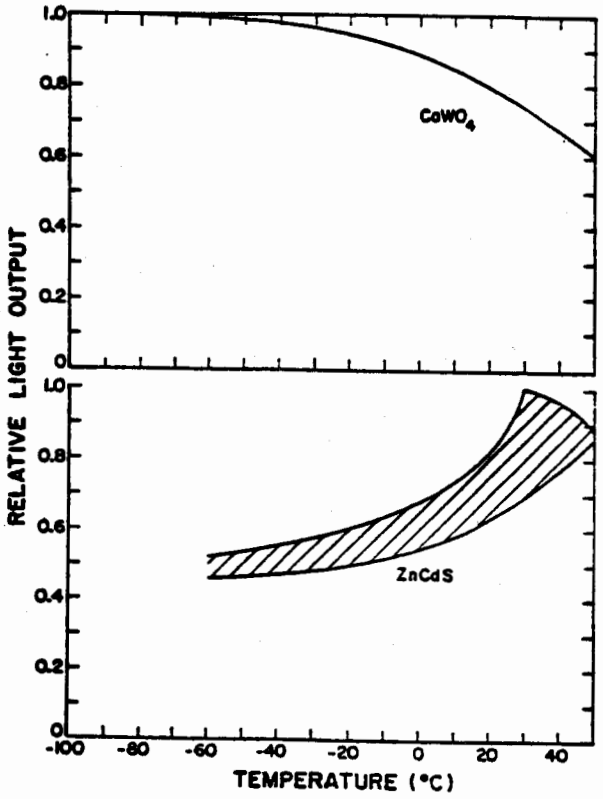

Fig. B-2.
Screen output vs temperature for $CaWO_4$ and ZnCdS.

about 25°C. This temperature is the approximate crossing point for the two curves, and provides the absolute comparisons between the two materials. Recall, however, that in a real satellite inspection system the effects of the objective lens and the response of the specific photocathode used with the image intensifier must be taken into account; in these experiments the recording photomultiplier had the S-20 photocathode. Further, it must be realized that different radiation absorption efficiencies at different photon energies will change the relative response of the two materials at any temperature.

Light output variations with temperature are significant, about a factor of two over the temperature extremes. The observed changes are probably not so gross as to eliminate either screen as a candidate material. However, in the design of a flight system, these data point to thermal control of the radiographic screen as one way of enhancing system performance.

VI. Summary

The components of the radiographic camera, which included scintillating screen, converter, objective lens, image intensifier, and power supply, have been thoroughly demonstrated. Either the 0.020-in. $CaWO_4$ or the 0.020-in. ZnCdS (if the persistence problem can be solved) screen is suitable, but the $CaWO_4$ screen is somewhat superior. The converter material should be strong enough to support the scintillating screen and still be flexible. Lead, being a soft material, has very little strength in thin sheets. Materials such as tungsten or tantalum have been used as converters and are much better suited to this application. Because tantalum and tungsten have higher density but lower atomic number than lead, an equal thickness can be used for all practical purposes. The optimum thickness of lead converter was found to be 0.040 in. (using the SCAPP) but radiographs of fair quality were made with 0.010-in. lead. Because the weight of the converter becomes appreciable for large screens, a 0.010-in. thickness of either tungsten or tantalum is recommended.

Because the f/0.95 lens was used typically in the program, all of the recommended intensities, etc., are based on a lens with this speed. A faster (or slower) lens would require proportionately less (or more) radiation to give the same picture. The fastest lenses used (f/0.95 and f/0.78) had also the narrowest view angle (30°), and the slowest lens (f/1.8) had the widest angle (94°). Assuming that these are the best lenses available, then the choice of lens becomes a trade-off between the intensity of the source and the distance from screen to lens. For example, if the screen size chosen is 6 by 6 ft, then the wide-angle lens is 3 ft from the screen and the narrow-angle lens is 12 ft from the screen. Because it should be relatively easy to design a lightweight, but rigid, light baffle for a 12-ft screen-to-lens separation, the f/0.95 lens (or faster) is recommended. The f/0.78 lens (also 30° view angle) is twice as fast as the f/0.95 lens, but is not recommended because of the arcing problem.

The proximity-focused (generation 2) image intensifier can easily be coupled directly to a vidicon with a fiber optics bundle rather than viewing the output with another lens, which costs another factor of at least 100 in intensity. It is also apparently unaffected by modest amounts of radiation, even at extremely high dose rates. As a result of this the lens and image intensifier can view the screen directly and are therefore unshielded (except by the target).

APPENDIX C

SPACE RADIATION BACKGROUND

I. Introduction

Nuclear detectors are sensitive to the primary and secondary effects of a number of space radiation backgrounds. The most intense effects arise from energetic charged particles trapped in the earth's magnetic field. Occasionally intense solar-proton flares produce energetic protons of intensities approaching those of the trapped particles. Galactic cosmic rays, consisting mostly of high-energy protons, affect the detectors by deposition of charge in sensitive regions and by secondary-particle production in both the earth's atmosphere and the spacecraft.

Neutrons which leak back into space from the atmosphere are the only important source of neutrons in free space, while neutrons produced in the spacecraft materials add to this free space background. The last background to be considered, that of cosmic gamma rays, is low enough to be almost insignificant. In the following sections the backgrounds will be treated in increasing order of importance.

II. Cosmic Gamma Rays

Cosmic gamma rays above 0.25 MeV have been measured by Vette et al,[29] who measured a flux of 0.7 photons $cm^{-2}sec^{-1}$ above 0.25 MeV and 0.2 photons $cm^{-2}sec^{-1}$ above 0.6 MeV. Above 0.6 MeV the intensity falls as $E^{-2.3}$. Because the flux is constant, except for variation of earth shadowing with satellite altitude, subtraction of this background should be simple if it becomes necessary.

III. Solar Proton Flares

Solar particles of energies from a few million electron volts up to a few gigaelectron volts are associated with certain solar flares. These particles are predominantly protons with varying fractions of alpha particles and heavier nuclei and are also called solar cosmic rays. The large events, occurring a few times a year, can produce fluxes exceeding the galactic cosmic rays by many thousands of times and can last one or two days. During such large events, neutron- and gamma-ray detectors would be unusable except in the low magnetic latitude portion of the lower orbits. There the earth's magnetic field would shield out all except the most energetic particles, with the penetrating flux depending strongly on the energy spectrum of the particles. Thus, solar protons would negate neutron- and gamma-ray detection only rarely and probably not at all for the midlatitudes of the 300-nm and lower orbits.

IV. Galactic Cosmic Rays

At the top of the atmosphere, protons contribute almost 90% of the cosmic-ray flux. Helium nuclei contribute 9%, with heavier nuclei and electrons each contributing 1%. The mean energy of the spectrum is about 1 GeV. The interstellar flux is constant and isotropic, but at the earth the flux is affected by solar activity. Short period decreases (Forbush decreases) of up to 15% in neutron production by the primary particles can occur after geomagnetic storms which are caused by solar activity. The flux gradually returns to the initial value in a day or two. Longer period variations are associated with the 11-yr solar cycle. The flux decreases about 40% from the solar activity minimum to the maximum. Probably the increase in particles leaving the sun at solar maximum increases the trapped magnetic field carried along by particles. Thus, the magnetic field in interplanetary space increases and excludes more of the cosmic rays, thereby causing the decrease in flux.

Consider first the atmospheric interaction. The primary particles produce protons and neutrons and other particles by nuclear reactions with the air molecules. The protons lose energy more rapidly to the air because they are charged. The neutrons are scattered, with a resultant energy loss, and some neutrons leak back out the top of the atmosphere. The resultant neutrons above the atmosphere are called albedo neutrons. The number of primary cosmic-ray particles reaching the top of the atmosphere at any point is affected by the earth's magnetic field. A relatively low-energy particle can reach the earth at the magnetic poles, but particles must have much higher energy to penetrate to the earth at the magnetic equator. Consequently, the cosmic-ray flux at the top of the atmosphere is at a minimum at the magnetic equator and rises gradually to a maximum in the magnetic polar regions. The albedo neutron flux produced by these particles varies by a factor of 7.4 between the equator and the poles.[30] The neutron flux at the top of the atmosphere (50 km) was determined to be 0.52 $cm^{-2}sec^{-1}$ at the poles

and 0.070 $cm^{-2}sec^{-1}$ at the equator at solar maximum. The flux variation with altitude was consistent with an R^{-3} dependence, where R is the distance from the center of the earth. This dependence is what one would calculate for an isotropic leakage flux.

The effects of cosmic rays on the detector-spacecraft system are difficult to calculate, because the geometry is complex and the high-energy particle-production cross sections are not well known. The effects are much more significant for the neutron detector than for the other detectors, so some experimental results for the Vela satellite neutron detectors will be used. These detectors are moderated ^{3}He proportional counters with no guard counters. The moderators are 6.5-in.-diam polyethylene cylinders, 6.5 in. long. The efficiency for fission-spectrum neutrons is 10 cm^2 (about 4%). The Vela orbits are circular at approximately 18 earth radii, and albedo neutrons are significant at this altitude. The cosmic-ray flux is approximately that of the lower altitude polar regions since the earth's magnetic field shielding is insignificant. The detector count rate from all cosmic-ray-produced effects varies from 8 sec^{-1} at solar maximum to 14 sec^{-1} at solar minimum; equivalent to a neutron flux of 0.8 to 1.4 $cm^{-2}sec^{-1}$. The spacecraft weight is approximately 350 kg, and the detector is well inside the spacecraft. At the top of the atmosphere, this detector-spacecraft combination would produce a count rate equivalent to a neutron flux of 1.3 $cm^{-2}sec^{-1}$ (0.8 + 0.52) at the poles and 0.17 $cm^{-2}sec^{-1}$,

$$\left(\frac{0.8 + 0.52}{7.4}\right),$$

at the equator at solar maximum and 5/3 of these rates at solar minimum. The local effects produced in the detector-spacecraft system are assumed to vary directly with the albedo neutron flux. This follows from the assumption that cosmic-ray neutron production in spacecraft materials is proportional to neutron production in the atmosphere.

V. Trapped Particles

The Van Allen or radiation belts of the earth are regions containing intense fluxes of energetic protons or electrons, or both. These particles are trapped by the earth's magnetic field, which is approximately a dipole field. Particles execute spirals along magnetic field lines which converge in the magnetic polar regions. The angle between the velocity vector and the field line (the pitch angle) increases as the particle continues in the direction of increasing field until it reaches 90°. At this point (the mirror point), the spiral motion along the field line changes direction by 180° and continues until the particle mirrors in the other hemisphere. If a mixture of particles is inserted on a field line at the magnetic equator (the point of lowest magnetic field intensity for any field line), the particles will spiral along this line and mirror at various points. Those with smaller pitch angles will mirror closer to the poles than those with larger pitch angles. The mirror points are independent of energy. Thus, the particle flux on this line would be greatest at the equator and would decrease as the field increases toward the poles. For any field line the particle flux should be a function of the magnetic field only.

Consideration of all identical field lines (identical except for their longitude) gives a shell which intersects the earth in a circle about each magnetic pole and is farthest from the earth at the magnetic equator. The distance in earth radii from the center of the earth to the shell equator is called the L value of the shell. Particles trapped on any field line of a particular L shell drift longitudinally around the earth in periods of the order of 1000 sec while mirroring between the hemispheres in about 1 sec. The trapped particles for a particular L shell mix thoroughly with all others in that shell. Thus, the trapped particle flux can be characterized by two variables: the magnetic field, B, and shell value, L.

Vette and others[31] have correlated data from many satellites which penetrate the radiation belts and have devised models of particle environment in terms of B and L. For each L one additional piece of information is needed, namely, the particle energy spectra. These are obtained experimentally for each shell. The NASA National Space Data Center has incorporated model environments on punched cards and has written a program to calculate satellite orbits, to determine B and L from position, and then to determine electron and proton fluxes and spectra from the model environments. The program is called TRECO.

The TRECO code was modified to record spectral information about the model radiation environment at selected time intervals along an orbit. In the case of trapped protons, the spectral information was obtained by plotting on film the particle flux in selected energy intervals. For the electron belts, further analysis was required so the complete spectrum at selected places was also punched on cards for later use.

The model trapped radiation environments which were used were also obtained from NASA and are referred to as the Vette models AP-1, AP-6, AP-7, and AE-2. The models are static and therefore, in the particular case of the electron model AE-2 of 1964, the model does not at the present time reflect the average composition of the belts. Variations in the average composition of the electron belts, which are expected to have taken place since the model year 1964, are a decrease in inner belt fluxes

caused by decay of the Starfish electrons and an increase in outer belt fluxes accompanying the increase of solar activity in the solar cycle. The inner belt discrepancy is the only one about which much information is available, so the AE-2 model environment was modified to approximate the present situation by truncating each spectrum for $L \leq 2.5$ above the energy 0.75 MeV. This corresponds to the NASA model electron environment which is expected to be published in 1972.

VI. Gamma Detector Background

Further analysis of the electron data was necessary because detector background is directly produced through bremsstrahlung photons. To calculate the bremsstrahlung radiation, an empirical method[32] was used in which the measured bremsstrahlung intensity produced in a thick target in the forward hemisphere is related to the ratio of the energy of the photon produced to the energy of the incident electron. Using a single empirical curve, a transmitted bremsstrahlung spectrum can be calculated from the incident electron spectrum. The method was checked using the Grumman electron spectrum[2] and did give the same photon spectrum that the Grumman report contains. To calculate a bremsstrahlung spectrum in the back hemisphere, a backscatter curve was obtained by taking the difference between published 4π and forward hemisphere curves.

To calculate the amount of bremsstrahlung radiation transmitted through shielding materials in a simple manner, some provision must be made for radiation which is initially scattered but is eventually counted because of the spatial extent of the active detector volume or of multiple scattering. Such scattering was accounted for by using as an absorption cross section the total energy absorption cross section plus one quarter of the total scattering cross section. This procedure has been shown to be valid for radiation in the range 10 to 100 keV and, for lack of other means, has been applied between 100 keV and 7 MeV.

The specific geometry calculated corresponds to a shielded Ge(Li) detector. The outer layer of 2-in. LiH serves to stop the incident electrons while producing a minimum amount of bremsstrahlung because of the low average Z. Next, a 1/4-in. layer of lead attenuates the large number of low-energy photons. The guard counter follows and is 2-in.-thick CsI. The remainder consists of a 3-in.-diam, thin Mylar jacket enclosing the 45-mm-diam by 50-mm-long active volume. The length of the shield was 20 in. and the field of view of the collimator 10°. The collimator aperture was closed to direct entry of charged particles by 2 in. of LiH which was followed by a soft photon filter composed of 1/2 g/cm^2 of molybdenum and 1/6 g/cm^2 of tin.

The assumption was made that the entire detector aperture would view the target, making the background calculation independent of distance. It was also assumed that charged particles would not enter the collimator during inspection. This could be accomplished in the lower orbits by not looking in directions approximately perpendicular to the magnetic field since the charged particle pitch angles are close to 90°. Thus, the background entering through the collimator was assumed to be back hemisphere bremsstrahlung produced in the near side of a thick aluminum target. The cylindrical sides of the shield were assumed to be directly exposed to the charged-particle environment, and the ends of the shield were assumed to be far enough away to produce negligible background.

During the calculation, all of the energy absorbed in the guard counter is tallied to produce the guard counting rate, and the Ge(Li) background rate is found from the photon spectrum reaching the active volume using a sample 6% Ge(Li) intrinsic photopeak efficiency curve. One must realize that the calculations of photon number and energy incident on the Ge(Li) have been simplified to permit calculations of a large number of cases. An accurate calculation would require an elaborate photon transport code (Monte Carlo) configured to a particular detector. Therefore one should use the heavily-shielded detector count rates as order-of-magnitude estimates.

TABLE C-I

(b)

APPENDIX D

NEUTRON SPECTRUM UNFOLDING

The use of gamma-ray interrogation either actively or passively allows the identification of elements with low (γ,n) reaction thresholds by the detection of the resultant neutrons. The elements of interest in the present application are ^{2}D and ^{9}Be which have (γ,n) thresholds at 2.226 and 1.666 MeV, respectively. The elements can be distinguished by the maximum energy (endpoint) neutrons produced. These energies are given below.

$$E_{max}(^{2}D) = 1/2(E_{\gamma} - 2.226)$$

$$E_{max}(^{9}Be) = 8/9(E_{\gamma} - 1.666)$$

For a simple system a well calibrated (in energy/channel) pulse-height analyzer would be adequate to distinguish these endpoints.

More information could possibly be obtained by unfolding the pulse-height spectra from the detector to obtain the neutron spectra incident on the detector. It may simplify identification in the case of significant shielding or moderation and in the presence of high-energy fission neutrons. In addition, it might be possible to obtain more quantitative information from the number of neutrons that can be assigned to each component [$^{9}Be(\gamma,n)$, $^{2}D(\gamma,n)$ and fission]. To this end the experimental and numerical techniques involved in unfolding pulse-height spectra obtained from ^{4}He proportional counters were investigated and are described here.

The equation for the response of a detector, $D(\xi)$, to a signal, $\phi(E)$, can be written as

$$D(\xi) = \int_{0}^{\infty} A(E,\xi)\phi(E)dE \quad , \tag{D-1}$$

where $A(E,\xi)$ is the response at ξ to a unit signal at E. In the present application (neutron-spectrum measurement) $\phi(E)$ is the neutron spectrum as a function of energy E, and $D(\xi)$ is the pulse-height spectrum as a function of pulse height ξ. This equation is commonly solved by dividing both the range of E and the range of ξ into a finite number of neutron-energy and pulse-height increments to obtain a set of simultaneous linear equations:

$$D_i = \sum_{j=1}^{J} A_{ij}\,\phi_j \quad i = 1 \ldots I \tag{D-2}$$

or

$$\underline{A\phi} = \underline{D} \quad .$$

Attempts at solving Eq. (D-2) by inverting the matrix $\underline{A}$ ($\underline{\phi}_s = \underline{A}^{-1}\,\underline{D}$) may lead to unbounded errors in the solution $\underline{\phi}_s$. These are a result of the nature of the equation and the fact that D is not known exactly but only as $D_i \pm \sigma_i$.

The least-structure method solves Eq. (D-2) subject to the constraints (1) that the (2nd derivative)^2 of the

solution be minimized and (2) that the residual ϵ [defined by Eq. (D-3)] be consistent with the

$$\underline{\epsilon} = A\phi_s - D \qquad \text{(D-3)}$$

error with which D is measured. Consistency here will mean

$$\sum_{i=1}^{I} \left(\frac{\epsilon_i}{\sigma_i}\right)^2 = I \quad .$$

The second derivative will be expressed by the following numerical approximation to the second derivative:

$$\frac{d^2\phi_j}{dE^2} = \frac{1}{h^2}\left(\phi_{j-1} - 2\phi_j + \phi_{j+1}\right) \quad .$$

The constrained minimization is accomplished by introducing the Lagrange multiplier λ and minimizing the function:

$$\psi = \frac{1}{h^2} \sum_{j=1}^{J} \left(\phi_{j-1} - 2\phi_j + \phi_{j+1}\right)^2 + \lambda \sum_{i=1}^{I} \left(\frac{\epsilon_i}{\sigma_i}\right)^2 \quad ,$$

or solving the set of equations

$$\frac{\partial\psi}{\partial\phi_j} = 0 \qquad \text{for } j = 1 \ldots J \quad .$$

It is assumed that

$$\frac{\partial^2\psi}{\partial\phi^2_j} = \frac{\partial^3\psi}{\partial\phi^3_j} = 0 \qquad \text{at } j = 1 \text{ and } j = J.$$

Forcing the solution to have a minimum second derivative as well as to satisfy Eq. (D-2) tends to prevent the unbounded oscillations mentioned above. The amount of smoothing used in the solution (how small the second derivative is forced) is strongly dependent on the estimate of the errors, σ, in the measured data, D. Clearly, too much smoothing will eliminate actual structure in the solution.

As a test of these techniques for obtaining neutron spectral information from pulse-height distribution measurements using ^{4}He proportional detectors, the neutron spectra from a ^{239}Pu sphere, a ^{252}Cf source, and from the (γ,n) reaction on ^{9}Be and ^{2}D at two electron energies were obtained. These measurements, shown in Figs. D-1 through D-3 and Fig. 43 were intended only as a proof of the experimental and numerical techniques and not as a demonstration of the full capability of the technique. It is felt that more can be done with the use of rise-time discrimination, with better measurements of the detector response function, A(E,ξ), and by using response functions more closely spaced in energy to take advantage of the resolution of the detectors.

In addition, by obtaining normalized response functions (counts/channel/incident neutron), absolute spectrum measurements can be made. The spectra presented here have arbitrary normalizations.

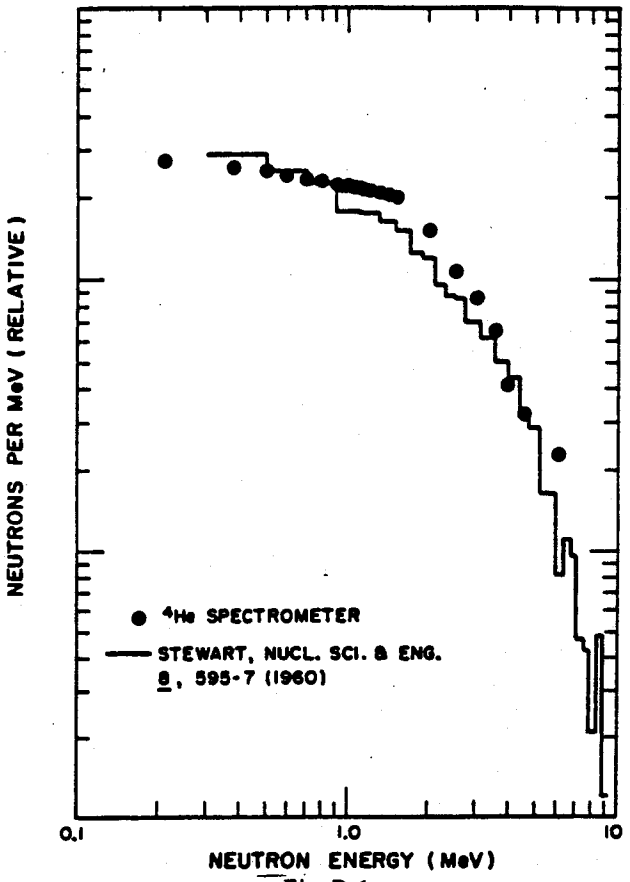

Fig. D-1.
Fission neutron spectrum from ^{239}Pu multiplying sphere.

UNCLASSIFIED

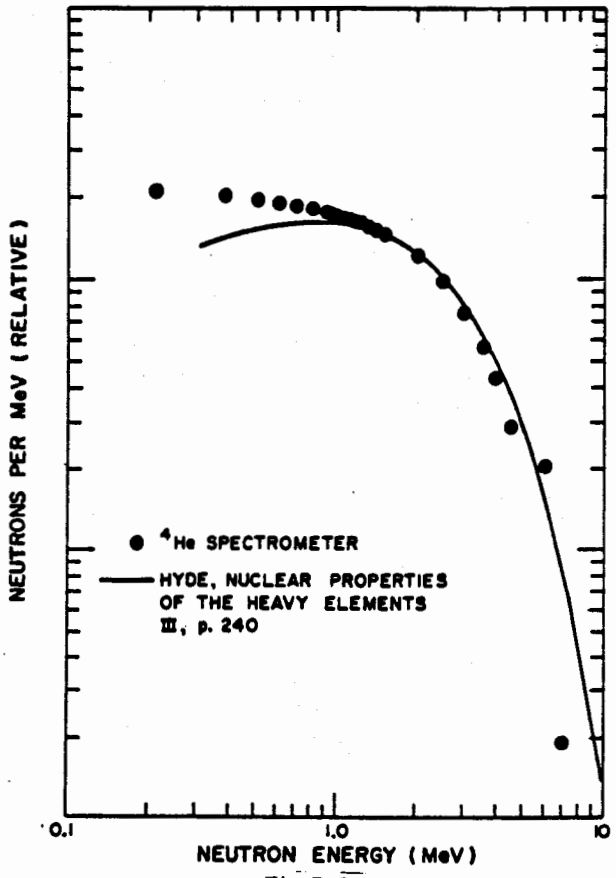

Fig. D-2.
Spontaneous fission neutron spectrum, ^{252}Cf.

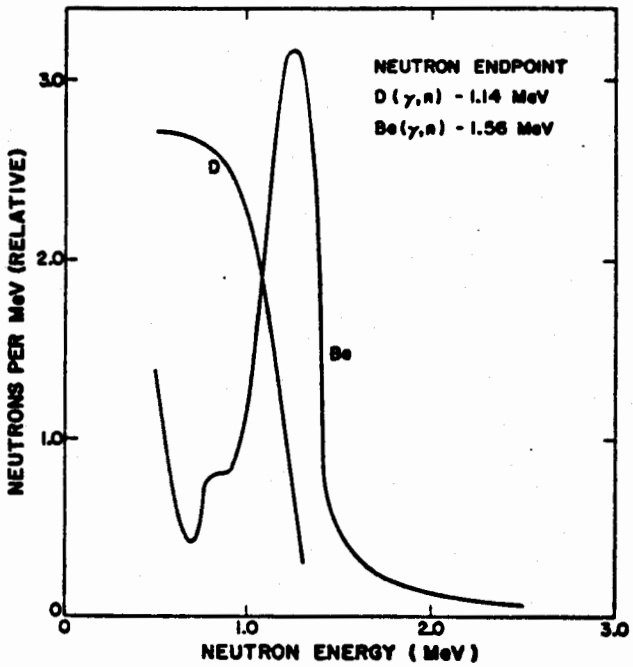

Fig. D-3.
Deuterium and beryllium photoneutron spectra, 4.5-MeV bremsstrahlung.

APPENDIX E

MONTE CARLO ANALYSIS OF ^{4}He NEUTRON DETECTORS

I. Introduction

General response characteristics of ^{4}He neutron detectors were studied with Monte Carlo techniques. These studies complement the experimental evaluation and application of ^{4}He detectors for neutron counting and spectroscopy. Effects of detector geometry, fill-gas composition, and gas pressure on detector response were examined by parametric Monte Carlo calculations. The calculated detector responses provide a guide to optimizing detector design for the particular applications considered in this study. A discussion of calculational techniques and typical results follows.

II. Generation of Range-Energy Table

A range-energy table is a basic requirement for the Monte Carlo calculation of recoil spectra. For a ^{4}He detector, this table of (E,R) values gives the range R(E) of the recoil alpha particle in ^{4}He, where E is the initial energy of the alpha particle. The range is calculated from

$$R(E_\alpha) = \int_0^{E_\alpha} (-dE/dx)^{-1}\, dE \quad , \qquad \text{(E-1)}$$

where dE/dx is the alpha-particle stopping power of ^{4}He at the appropriate gas pressure. Values of stopping power were obtained from the recent and very useful compilation of Northcliffe and Schilling.[33] With the format of Ref. 33 as a guide, R(E) was evaluated analytically in the range $0 \leq E \leq 0.05$ MeV using $-dE/dx = kE^{1/2}$, with k determined from the stopping power at 0.05 MeV. For the energy range $0.05 < E \leq 48$ MeV, R(E) was numerically evaluated from Eq. (E-1) using a seven-point Newton-Cotes formula to integrate tabulated $(dE/dx)^{-1}$ data. To provide a finer logarithmic energy scale, R(E) was evaluated at the intermediate values

$$E = \exp\,[0.5\,(\ln E_i + \ln E_{i+1})] \quad , \qquad \text{(E-2)}$$

where E_i and E_{i+1} are consecutive values on the referenced energy scale.

III. Monte Carlo Procedure

Monte Carlo calculations were made for an isotropic point source of neutrons located on the axis of a cylindrical proportional counter. The calculational geometry is shown in Fig. E-1. The Monte Carlo calculational steps are outlined:

(1) Neutrons are emitted isotropically at S. Only those neutrons emitted within a source cone defined by the half-angle θ are sampled. These neutrons enter the detector where they can escape from the detector with no collision, be captured in the detector wall, or be elastically scattered by ^{4}He. A neutron having an elastic scattering collision at C will have an energy and direction (E_n, u_n, v_n, w_n) after collision, as determined from the differential scattering cross section $d^2\sigma/dE d\Omega$ (u_n, v_n, and w_n are the direction cosines).

(2) The energy and direction of the recoil nucleus $(E_\alpha, u_\alpha, v_\alpha, w_\alpha)$ are calculated from conservation of energy and momentum after collision.

(3) Using a binary search interpolation routine, the recoil nucleus range $R(E_\alpha)$ is computed from the range-energy table.

(4) Step 4 treats wall and end effects. The distance, r, in the direction $(u_\alpha, v_\alpha, w_\alpha)$, from the point of collision C to the nearest detector wall is computed. If $r > R(E_\alpha)$, one event is tallied for the energy group ΔE containing E_α. If $r < R(E_\alpha)$, the distance r is expressed as

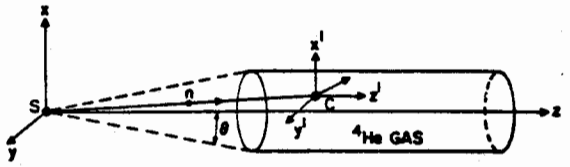

Fig. E-1.
Monte Carlo calculational geometry for isotropic point source of neutrons located on the axis of a cylindrical proportional counter.

$$r = R(E_\alpha) - R(E_w) \quad , \qquad \text{(E-3)}$$

where E_w = energy of the recoil nucleus on reaching the detector wall and $R(E_w)$ = residual range, i.e., range of the recoil nucleus having energy E_w. Since r and $R(E_\alpha)$ are known, the residual range is given by $R(E_w) = R(E_\alpha) - r$. Using inverse interpolation, E_w is computed from the range-energy table and one event is tallied for the energy group E containing $E_\alpha - E_w$.

(5) Steps 1 through 4 are repeated until enough neutron histories have been computed to give the desired statistical accuracy. The resulting tally per energy group gives a histogram of the ideal (perfect resolution) recoil pulse-height spectrum.

Actual recoil pulses produced in the proportional counter by monoenergetic neutrons will have an energy distribution due to the statistical nature of the ion production and energy loss processes. Effects of statistical processes, local field inhomogeneities, pulse rise-time, and external electronics on detector resolution are difficult to calculate accurately from first principles. Rather than attempting to include these effects analytically, we treated detector resolution by distributing the pulse height in each energy group with a Gaussian function. Detector resolution expressed as a Gaussian distribution has been shown to be a valid technique in the interpretation of measured ^{4}He recoil pulse-height spectra.[34,35]

After completion of Step 5 above, the recoil pulse-height distribution is given by C_j counts accumulated in energy group ΔE_j, j=1, —, J. Each pulse height is to be spread in energy by the Gaussian distribution

$$P_j(E) = (1/\sqrt{2\pi}\,\sigma) \exp\,[-(E-\bar{E}_j)^2/2\sigma^2] \quad , \qquad \text{(E-4)}$$

where $\bar{E}_j$ is the mean energy of group ΔE_j and σ is the standard deviation. The common measure of resolution, full width at half maximum, is $E_{½} = 2.35\sigma$. Using this relation, Eq. (E-4) becomes

$$P_j(E) = (0.938/E_{½}) \exp[-2.76\,(E - \bar{E}_j)^2/E_{½}^2]\,. \quad \text{(E-5)}$$

The distributed pulse height in group ΔE_i, resulting from the computed ideal pulse height in group ΔE_j, is calculated numerically using Eq. (E-5) as

$$C_{ij} = \int_{E_{i-1}}^{E_i} C_j\, P_j(E)\, dE, \quad \Delta E_i = E_i - E_{i-1}\,. \quad \text{(E-6)}$$

The total pulse height in group ΔE_i is then given by

$$C_i = \sum_{j=1}^{J} C_{ij}\,. \quad \text{(E-7)}$$

Values of C_i from Eq. (E-7) give the recoil spectrum with detector resolution effects simulated by a Gaussian distribution. The resolution used in Eq. (E-5) is given by

$$E_{½} = 0.1\ \bar{E}_j,\ \bar{E}_j \leq 1.0\ \text{MeV}$$

$$= 0.10\ \text{MeV},\ \bar{E}_j > 1.0\ \text{MeV}\,. \quad \text{(E-8)}$$

This empirical relation is based on examination of typical resolution values reported in the literature.

Figure E-2 shows alpha-particle recoil spectra resulting from an isotropic point source of neutrons located 1.0 m from the nearest detector end face. The detector length is 24 in., the o.d. is 2 in., and the ^{4}He gas pressure is 8 atm.

These calculations are based on the same neutron source strength, so that all recoil spectra in Fig. E-2 can be compared on the same relative amplitude scale. The amplitudes are plotted in Monte Carlo units of weight per million electron volt which, as noted, are proportional to counts/channel. In ^{4}He, the maximum neutron energy transfer corresponds to 180° scattering, resulting in a recoil ^{4}He nucleus having 64% of the incident neutron energy.

As an example of the type of survey calculations that were made with these Monte Carlo techniques, effects of detector length on recoil pulse shape and amplitude were calculated. The response to 1.0-MeV neutrons for detector lengths from 5 to 25 in. is shown in Fig. E-3. In each case the source is located on the detector axis at 1 m from the nearest detector end face. Figure E-3 shows that an increase in the detector length increases the peak amplitude at slightly less than a linear rate. The increased amplitude is due primarily to increased path length for maximum energy transfer (180° scattering). Other effects of detector length are summarized in Table E-I.

The Table E-I data show that a reduction in detector length should not degrade the peak shape. Because

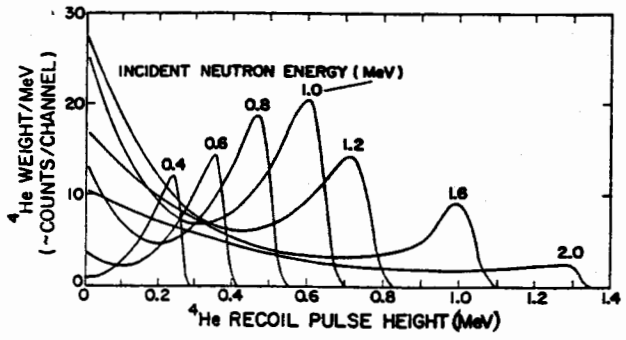

Fig. E-2.
Calculated recoil pulse-height spectrum in 8-atm ^{4}He detector for 0.4- to 2.0-MeV neutrons.

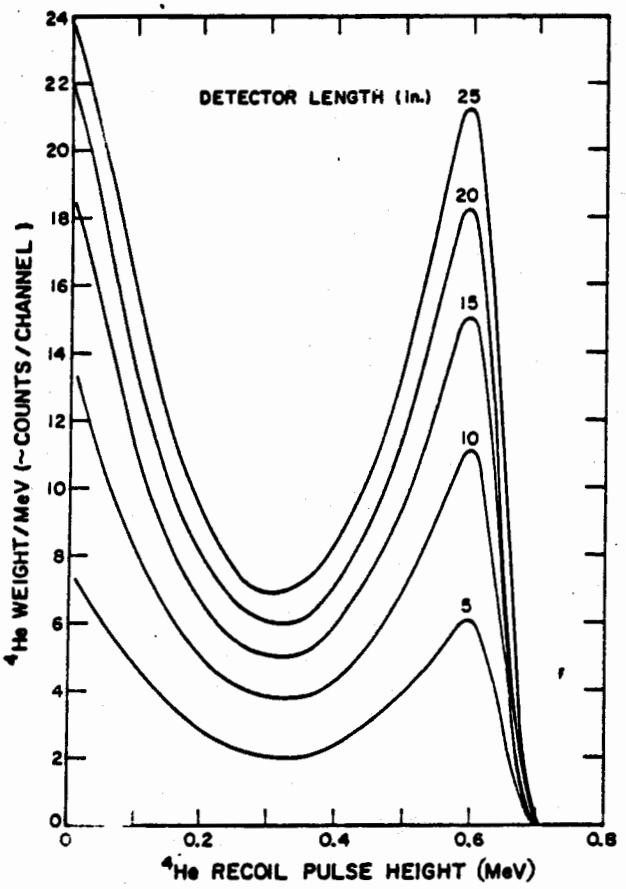

Fig. E-3.
Effect of detector length on recoil pulse spectrum for 1.0-MeV neutrons. ^{4}He detector, 2-in. o.d., 8-atm pressure.

TABLE E-I

EFFECTS OF DETECTOR LENGTH

Detector Length (in.)	Peak/Valley	FWHM (MeV)	Peak Location (MeV)
5	3.0	0.20	0.59
10	3.0	0.20	0.60
15	3.0	0.19	0.60
20	3.0	0.19	0.60
25	3.1	0.20	0.60

only the number of counts in the peak is significantly changed by reducing the tube length, a short ^{4}He detector could be used whenever the counting time is sufficient to achieve the required statistical confidence.

The ^{4}He detectors recommended for bremsstrahlung-induced (γ,n) and (γ,f) interrogation are to have 16-atm gas pressure. Monte Carlo calculated response functions for 16-atm detectors are shown in Figs. E-4 and E-5, for 1- and 3-MeV neutron sources, with tube of 2-in. o.d., length of 24 in., and source-to-detector distance of 1 m. Increase in the gas pressure from 8 to 16 atm increases the amplitude of the full energy peak by a factor

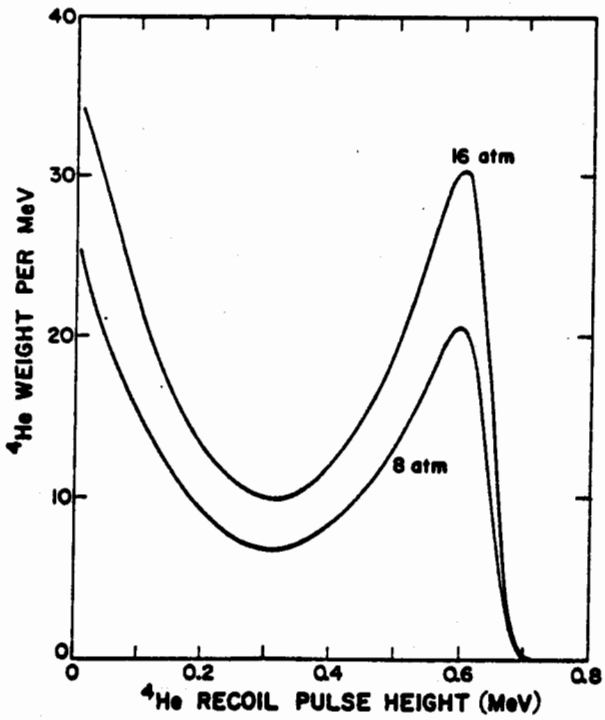

Fig. E-4.

Calculated recoil pulse-height spectra in 8- and 16-atm ^{4}He detectors for 1.0-MeV neutrons.

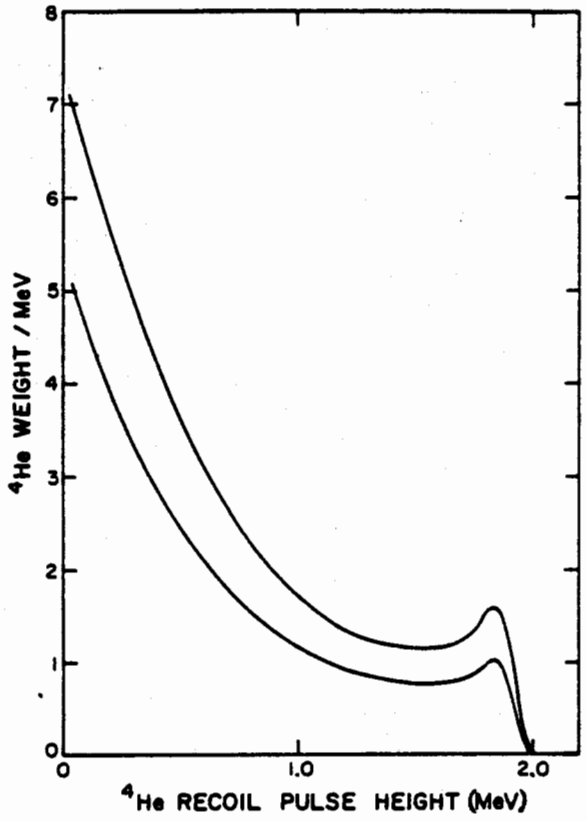

Fig. E-5.

Calculated recoil pulse-height spectra in 8- and 16-atm ^{4}He detectors for 3.0-MeV neutrons.

of 1.5. The FWHM and peak/valley ratio are unchanged by a doubling of the ^{4}He pressure.

Calculated response functions discussed thus far are based on a source-to-detector distance of 1 m. To determine what changes will occur when the detectors are moved to the baseline distance of 20 ft from the source, response functions were calculated for this source-to-detector distance. At the larger distance, the solid angle subtended by the detector end face is reduced by 0.027. The ratio of calculated peak amplitudes is 0.033. Thus, the intrinsic efficiency of the ^{4}He detector is increased by 0.033/0.027 = 1.22 in moving from 1 m to 20 ft away from a point source. This is because neutrons from the larger distance are entering the detector more nearly parallel to the axis. The Monte Carlo calculations indicate that there should be no inherent problems in using 16-atm ^{4}He detectors at interrogation distances in the neighborhood of 20 ft.

Detector responses were calculated for several neutron spectra and compared with measured pulse-height spectra from the same sources. Figures E-6 and E-7 show calculated ^{4}He detector response to 4.5-MeV bremsstrahlung-induced (γ,n) spectra from D(D_2O) and beryllium. The 8-atm, 2-in.-o.d., 24-in.-long detectors were used with

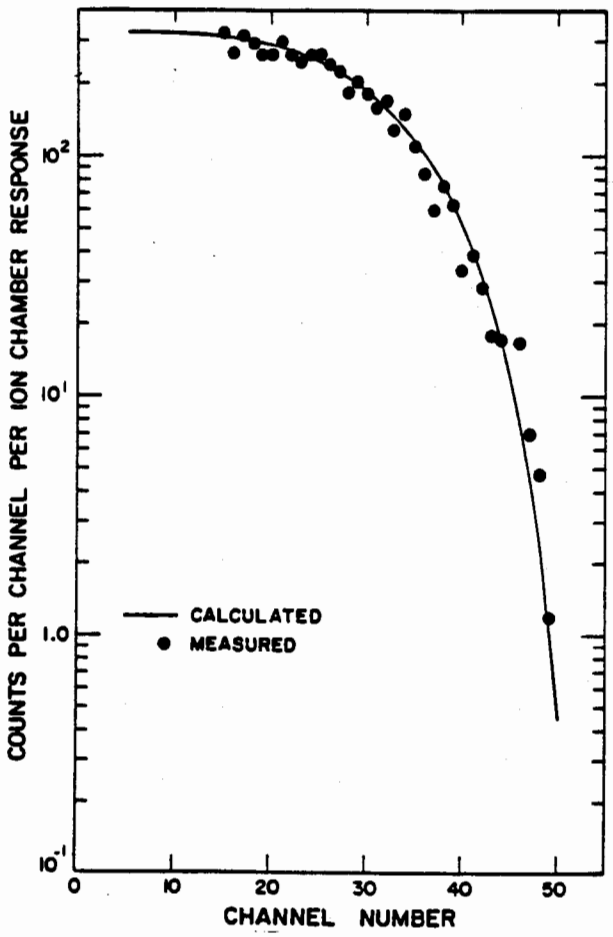

Fig. E-6.

^4He detector response to 4.5-MeV electron bremsstrahlung-induced (γ,n) spectrum from D to D_2O.

a 1-m source-to-detector distance in the calculations and measurements. The computed detector response for deuterium gives a good fit to the measured data. Some disagreement between the measured and calculated response is evident for the beryllium data. This difference is partially attributable to uncertainties in the contribution by excited state beryllium transitions to the photonuclear spectrum used in the Monte Carlo calculation. The general agreement between measured and calculated spectral response supports the application of photonuclear interrogation to distinguish between beryllium and deuterium.

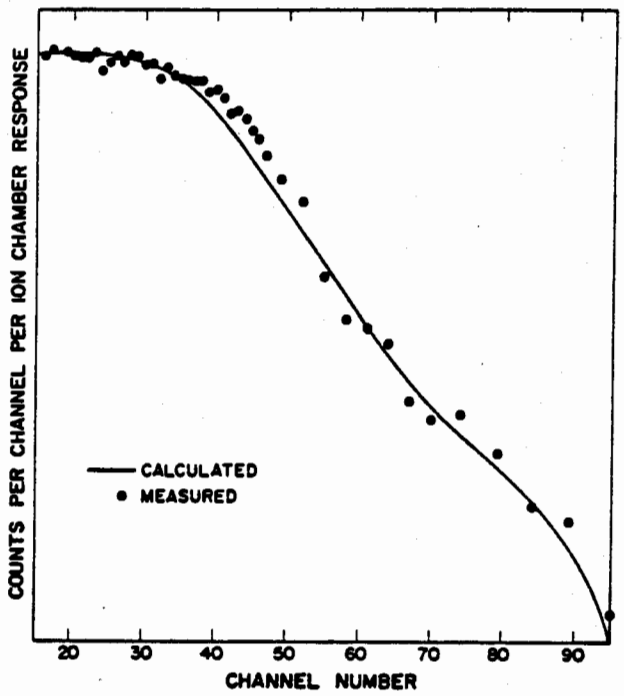

Fig. E-7.

^4He detector response to 4.5-MeV electron bremsstrahlung-induced (γ,n) spectrum from beryllium.

APPENDIX F

RADIOGRAPHIC IMAGE ENHANCEMENT

Existing LASL facilities were used in an attempt to demonstrate the potential of image processing in restoring and extracting information from poor quality radiographs such as those telemetered to earth after a satellite inspection. Image processing of television pictures taken by the Ranger and Mariner spacecrafts has already demonstrated the utility of the approach in a space application. Briefly, image processing techniques can be used to:

(1) Correct for photometric distortion of the vidicon,

(2) Remove scan noise associated with slight variations in the scanning beam position from scan to scan,

(3) Remove scan noise associated with the Gaussian shape of the intensity across the scanning beam diameter,

(4) Filter out recognizable, periodic system noise from other electronic subsystems on board the spacecraft,

(5) Stretch contrast,

(6) Sharpen edges for fine detail enhancement by a variety of schemes,

(7) Smooth out white or random noise, and

(8) Provide optimal (Wiener) filtering if adequate models of the noise and of the image proper can be made available.

The above list is by no means exhaustive. Threre are many other processing techniques which might be applicable and useful.

In this program photographic film instead of a video system was the basic image-recording medium; and since a TV camera is probably the primary noise source in a real system, image processing of film may not be especially applicable to the real system case. Nevertheless, it was felt that the potential of image-processing techniques to the enhancement of radiographs of real weapons might be demonstrable and that the opportunity to operate on such images should not be passed.

Detailed discussions of image processing are to be found in Refs. 36 through 39, and the following discussion is meant merely to acquaint the reader with rudimentary notions of the image-processing techniques applied in this effort.

The mechanics of image processing are straightforward. An image, usually on a negative, is scanned by a rapid-scan microdensitometer which digitizes the image and stores it on magnetic tape. Computer storage limitations restricted the processing to 500 scans, each scan containing 500 discrete values. The stored image on tape then corresponded to a 500 x 500 array of density values, or 2.5×10^5 density points. The 50μ aperture used for the scanning took full advantage of the inherent resolution contained in the initial images. This inherent resolution is determined by the image intensifier resolution and not the film, which has a much higher intrinsic resolution. The digitized image, now on tape, can then be computer-manipulated and the processed image "played back" on Polaroid film. At LASL the scan and playback are performed on the same machine, a Photometric Data Systems Microdensitometer system 1050A, which contains a PDP-8 computer.

Computer processing is typically done in either of two ways: (1) the digitized image (point locations and corresponding density values) is manipulated directly by the program, or (2) the density points are treated as a function which is represented by the points, and the function is transformed into the Fourier or spatial frequency domain before manipulation.

With the first approach, for example, noise smoothing is possible by averaging each density point with several of its neighboring points. Contrast stretching is also done by working directly with the density values; the mean density value for the entire image is computed and then all density values on the tape are increased or decreased with respect to the mean value. There are many other processing schemes which involve the manipulation of only density data.

The density data are transformed into a spatial frequency representation when some kind of filtering is preferred. Since the "function" to be transformed is represented by discrete density values, the discrete Fourier transform (DFT) is used. One form of the DFT is

$$A_r = \sum_{k=0}^{N-1} X_k \exp(-2\pi jrk/N) \quad r = 0, \ldots, N-1 \quad ,$$

where A_r is the rth coefficient of the DFT, X_k denotes the kth density sample in a one-dimensional series, and $j = \sqrt{-1}$. The A_r's are almost always complex, and the index r is sometimes called the frequency of the DFT.

Operating on a series (a scan) of density values using the above expression produces a set of complex coefficients representing the amplitudes of all the spatial frequency components which make up the "image" formed by the density values. From these calculated amplitudes, the power spectrum of an image can be generated. The power spectrum is nothing more than the square of the absolute value of the Fourier transform, i.e., $|D_s(f)|^2$, where $D_s(f)$ is the transform of $d_s(x)$, the density function. The arguments f and x refer to frequency and position respectively, and the units are conventionally in cycles/millimeter and millimeters. The power spectrum indicates the frequency content of an image and is useful in choosing the filter to be applied to the image in the spatial frequency domain. To relate the density values in real space and the power spectrum in the spatial frequency domain, it might be pointed out that the spacing of the density values turns out to be the wavelength of the highest frequency component in the resulting power spectrum; while the span of the density data is the wavelength of the zero frequency or fundamental mode in the power spectrum.

The final detail of an image is contained in the high-frequency components of its power spectrum (once the image has been transformed). Similarly the broader

features and information about the overall exposure and contrast of an image are contained in the lower-frequency components of its power spectrum. This observation leads naturally to an enhancement scheme in which the image in spatial frequency domain is filtered in such a way that the high frequencies of the power spectrum are boosted and the low frequencies attenuated. The result, when the image is transformed into its original form, should be an enhancement of edges and of fine detail.

Similarly certain kinds of periodic, predictable noise patterns may be evident in a given image, and may be easily filtered out by applying an attenuating filter in frequency space to that band of frequencies which represents the noise. If the filter has been properly chosen and properly applied, then transforming the image to its original form produces an enhanced image in which the bothersome noise has been removed. Such an approach is generally valid only when the power spectrum of the noise is in well-defined bands and does not coincide with the frequency bands in which essential information is contained. Otherwise the desired information will be filtered out along with the unwanted patterns.

In this program, it was decided to use high pass-filtering and contrast stretching as the basic processing schemes. While it was not felt that these two schemes necessarily represent the optimum processing schemes, computer programs were readily available for them. Also, these techniques are well established and known to be

UNCLASSIFIED

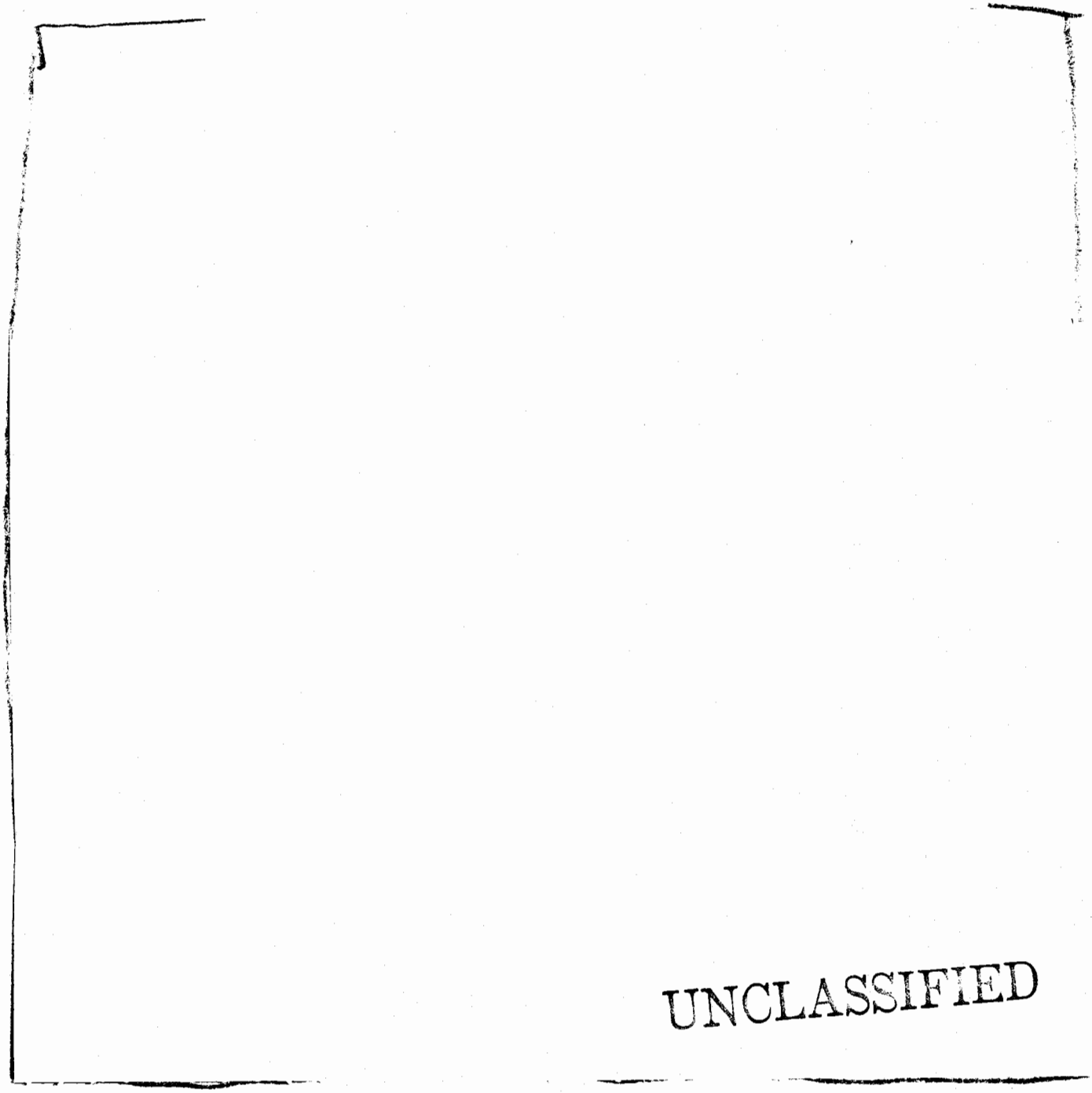

UNCLASSIFIED

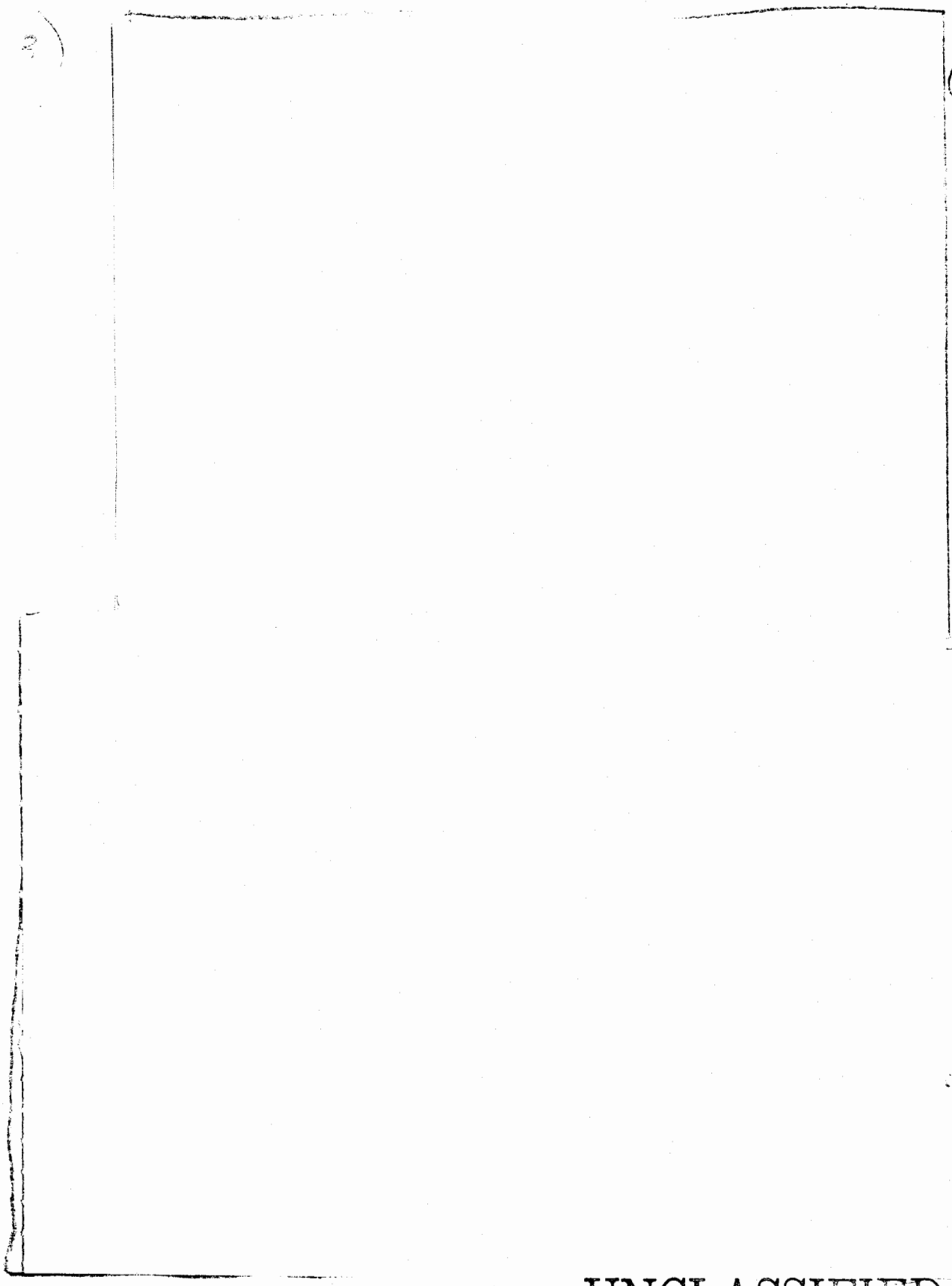

(1)(3)

(1)(3)

a)

b)

b(1)

(1)(3)

UNCLASSIFIED

It is anticipated that effort on image enhancement will continue at LASL. Many different enhancement schemes will be attempted on the basic set of data already collected for this program. In addition, it is anticipated that a video system will be assembled and video tape output, which more closely matches the data from a spaceborne inspector, will be available for the simulation of noise suppression and information recovery.

~~SECRET~~

UNCLASSIFIED

This page intentionally left blank!

UNCLASSIFIED

~~SECRET~~